TESLA - COLLABORATION

Contributions to the PAC'95

DESY Print June 1995, TESLA 95-11

Contributions to the PAC'95 - Contents

Studies on a Free Electron Laser for the TESLA Test Facility

J. Rossbach
for the TESLA FEL Study Group[1]
Deutsches Elektronen Synchrotron, D-22603 Hamburg, Germany

Abstract

We present the layout of a Single Pass FEL to be driven by the TESLA Test Facility (TTF) currently under construction at DESY. The TTF is a test-bed for high-gradient, high efficiency superconducting accelerating sections for a future linear collider. Due to its unrivaled ability to sustain high beam quality during acceleration, a superconducting rf linac is considered the optimum choice to drive a Free Electron Laser (FEL). We aim at a photon wavelength of $\lambda = 6$ nm utilizing the TTF after it has been extended to 1 GeV beam energy. A first test is foreseen at a larger photon wavelength.

1. GENERAL DESCRIPTION

A Free Electron Laser (FEL) in the soft X-ray regime is under study, using the superconducting linac of the TESLA Test Facility (TTF) being under construction at DESY [1]. The FEL at the TESLA Test Facility (TTF FEL) is based on the principle of 'Self Amplified Spontaneous Emission' (SASE) [2]. The key advantage of the SASE scheme compared to other FEL schemes is that neither an input seed laser is required nor mirrors forming an optical cavity. Thus, no known fundamental limitation would prevent operation even down to the Ångstrom region. In the first section of the undulator the electrons radiate independently and the phases of the photons are randomly distributed. Since microbunch formation starts from this „random" noise, a long undulator is needed to achieve laser action with exponential growth in light output. For the TTF FEL an overall undulator length of 30 m is planned.

The photon wavelength λ_{ph} of the first harmonic is related to the period length of a planar undulator λ_u by

$$\lambda_{ph} = \frac{\lambda_u}{2\gamma^2}\left(1+\frac{K^2}{2}\right), \qquad (1)$$

where, $\gamma = E/mc^2$ is the relativistic factor of the electrons and $K = e B_u \lambda_u / 2\pi mc$ the 'undulator parameter', e being the elementary charge, m the electron rest mass, c the speed of light, and B_u the peak field in the undulator.

The physics program for the TTF FEL requires a photon wavelength of 6 nm. Therefore, for state-of-the-art undulator parameters are assumed, e.g. $\lambda_u = 27$ mm, $K = 1.3$, a beam energy of 1GeV is necessary.

Two beam parameters are essential to reach power saturation within a not too long undulator: A small transverse beam emittance ε_t to provide both small beam diameter and small beam divergence in the undulator, and a small longitudinal beam emittance ε_z to achieve kilo-Ampere instantaneous beam currents at an energy width in the 0.1% range.

The TTF is an ideal accelerator to drive a SASE FEL. There are two main reasons:

- The perturbation of small emittance beams during the acceleration process is smallest with a superconducting linac at lower frequency. Because the resonator volume and the stored energy are big, the accelerating field is hardly affected by the presence of the electron beam. The variation of the effective accelerating voltage over the bunch length („longitudinal wakefield") is minimum and the tendency of beam induced rf deflections („transverse wakefields") is small.
- A superconducting linac provides a large AC power efficiency and a high duty cycle. The TESLA Test Facility will operate at 1 % duty cycle, orders of magnitude larger than a normal conducting linac would do at the TTF nominal gradient of 15 MV/m. In addition to power efficiency, this is another crucial advantage for potential experiments, because it leaves sufficient time between pulses in the bunch train for data handling.

The most expensive single component of a short wavelength FEL is the accelerator. Taking into account,

---

[1] The TESLA FEL Study Group:

ASC Samara: E.L. Saldin, E.A. Schneidmiller, **CE Saclay:** A. Mosnier, **DESY:** R. Bacher, W. Brefeld, M. Dohlus, H. Edwards, B. Faatz, J. Feldhaus, K. Flöttmann, A. Gamp, P. Gürtler, K. Hanke, L. M. Kieman, J. Krzywinski, M. Leenen, T. Limberg, G. Materlik, T. Möller, J. Pflüger, D. Proch, J. Rossbach, J. Schneider, S. Schreiber, J. Sekutowicz, M. Seidel, K. Tesch, D. Trines, R. Wanzenberg, H. Weise, S.G. Wipf, B.-H. Wiik, **Fermilab Chicago:** E. Colby, T. Nicol, **Helsinki Univ. of Technology:** T. Åberg, **INFN Milano:** R. Bonifacio, C. Pagani, P. Pierini, L. Serafini, **JINR Dubna:** M.V. Yurkov, **KFA Jülich:** W. Eberhard, G.Ganteför, **Lab. de Photophys. Moléculaire Paris:** G. Comtet, G. Dujardin, L.Hellner, **Lawrence Livermore Natl. Lab.:** T. Scharlemann, **LNLS Campinas:** ,R. DeCastro, **Los Alamos Natl. Lab.:** J. Goldstein, R.L. Sheffield, **Max-Born-Institut Berlin:** H. Rottke, W. Sandner, I. Will, **Max-Planck-Inst. f. Biophys. Chemie Göttingen:** T. M. Jovin, **Max-Planck-Inst. f. Mikrostrukturphys. Halle:** C. M. Schneider, **Polish Acad. of Sciences Warschau:** K. Rzazewski, **TU München:** P. Feulner, D. Menzel, W. Wurth, **UCLA Los Angeles:** J. Rosenzweig, **Univ. Bielefeld:** D. Feldmann, **Univ. Birmingham:** R. E. Palmer, **Univ. Bochum:** K. Al-Shamery, M. Baems, H. J. Freund, W.Greinert, **Univ. Düsseldorf:** E. Kisker, **Univ. Essen:** C. Westphal, H. Zacharias, **Univ. Frankfurt:** H. Schmidt-Böcking, L. Spielberger, **Univ. Göttingen:** G. Schmahl, **Univ. Hamburg:** C. Kunz, B. Sonntag, H.J. Voß, **Univ. Kiel:** L. Kipp, M.Skibowski, **Univ. Rostock:** K. H. Meiwes-Broer, **Univ. Tomsk, Russia:** Y. Nikitina, **Univ. Würzburg:** H.-P.Steinrück, **Uppsala Univ.:** M. Martensson

that a SASE FEL needs beam parameters similar to those to be realized for a Linear Collider, it is obvious that the TTF linac can be ideally utilized for driving a SASE FEL. For the discussion of the TESLA Test Facility linac and its relation to the TESLA 500 Linear Collider scheme we refer to the TTF Design Report [1].

The TTF design energy is 500 MeV. It has to be upgraded to 1 GeV electron beam energy required for the desired photon wavelength. Figure 1 shows the overall TTF FEL scheme. Table 1 compiles main parameters of the TTF FEL.

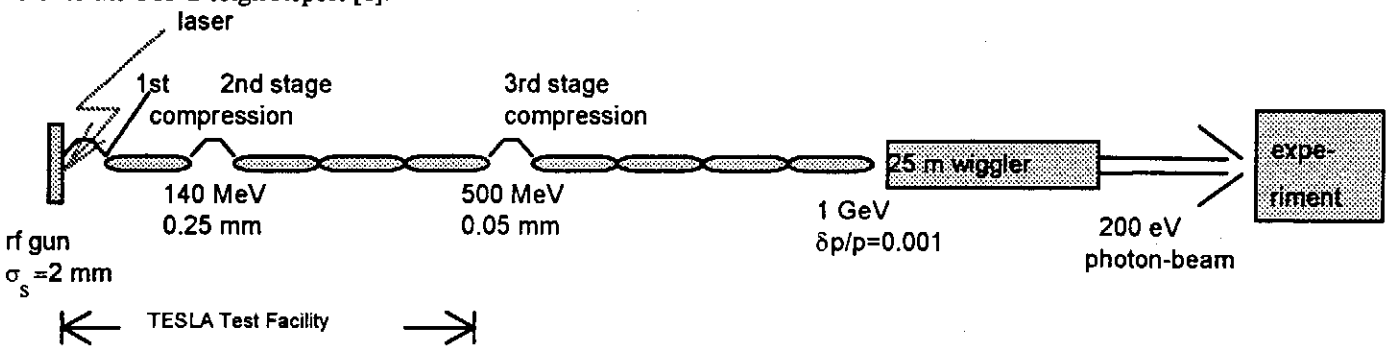

Figure 1: Schematic layout of the TTF FEL based on the TESLA Test Facility (TTF). Four additional TESLA accelerator modules bring the energy up to 1 GeV. The bunch length is reduced from 2 mm to 50 μm within three steps of bunch compression. The SASE FEL process requires an undulator of 25 m effective length. The over-all length of the facility is some 200 meters.

2. ELECTRON SOURCE

The transverse coherence condition imposes a tight requirement on the transverse emittance ε_t of the electron beam [3]:

$$\varepsilon_t^n \leq \frac{\gamma \cdot \lambda_{ph}}{4\pi}$$

ε_t^n is the *normalized* emittance. For λ_{ph} = 6 nm, γ = 2000, this requires $\varepsilon_t^n < 1\ \pi$ mrad mm. Actually, as is seen from Figure 2, this condition is not very strict, but the saturation length significantly increases if ε_t^n is larger. Thus, we aim at $\varepsilon_t^n = 1\ \pi$ mrad mm for the rms electron emittance of a 1 nC bunch charge from the electron gun, and we allow for a factor of two emittance dilution during longitudinal beam compression and acceleration up to 1 GeV. According to beam dynamics simulations in both the bunch compressors and the accelerator, this seems to be a conservative assumption. These very high phase space densities came into reach due to two major achievements: The development of the rf gun [4] and the concept of space charge compensation [5].

3. UNDULATOR

The undulator is the most prominent FEL specific component. The proposed design avoids technical risks. A planar hybrid undulator is foreseen with period length λ_u = 27 mm and peak magnetic field B_u = 0.5 T, parameters very much like those of existing undulator magnets. The main challenges are the total length of 30 m, the additional quadrupole focusing to be supplied and tight tolerances. To simplify production, measurement and installation, 5m long modules are forseen. This also permits installation of electron and photon beam monitors and correction elements.

VARIABLE	UNITS	VALUE
beam energy	GeV	1.000
λ(radiation wavelength)	nm	6.4 (193 eV)
λ_u (undulator period)	mm	27.3
undulator gap	mm	12
B (undulator peak field)	T	0.497
undulator length	m	25
beam optics β function	m	3
rms beam size	mm	0.05
ε^n (normalized emittance) in the undulator	π mrad mm	2.0
peak electron current	A	2490
number of electrons per Gaussian bunch		6.24E+9
number of photons per Gaussian bunch		4E+13
peak electron beam power	GW	2490
energy spread σ_γ/γ	10^{-3}	1.00
bunch length	μm	50.
L_g (power gain length)	m	1.00
L_S (saturation length)	m	< 25
P_{sat} (saturated power)	GW	3
average brilliance [photons/s/mm²/mr/0.1%]		up to 6E+21
bunch train length	μsec	800
number of bunches per train		up to 7200
repetition rate	Hz	10

Table 1: Main parameters of the TESLA Test Facility FEL (TTF FEL). The in·'tion device is assumed to be a planar hybrid undulator. These values should be used as a guideline only since the optimization has not yet been finished and experimental experience has to be gained in this wavelength regime.

4. FEL PROCESS

Various computer codes have been used to investigate the start-up from noise, and the lethargy, exponential and saturation regimes, respectively, e.g. NUTMEG [6], GINGER[7], FS2R[8], TDA[9,10]. There is no essential disagreement between results of all these codes written by different groups and based on different approaches. It should be noted though, that for a complete study of the shot noise startup the time dependence of the input noise and the slippage effects should be taken into account in the theory and in the simulations. The one-dimensional analysis shows that a critical parameter for shot noise analysis is the beam length in units of the "cooperation length" [11]:

$$\lambda_c = \frac{\lambda}{4\pi\rho}.$$

For the TTF FEL the cooperation length is 0.26 μm, and the beam length is 50 μm. In this case bunch-to-bunch fluctuations should be a fraction of a gain length and the use of an equivalent input signal analysis should be adequate. A more careful study with existing time dependent FEL codes (GINGER and FELEX) is in its starting phase and will be reported soon. Figure 2 shows the emitted intensity as a function of ε^n.

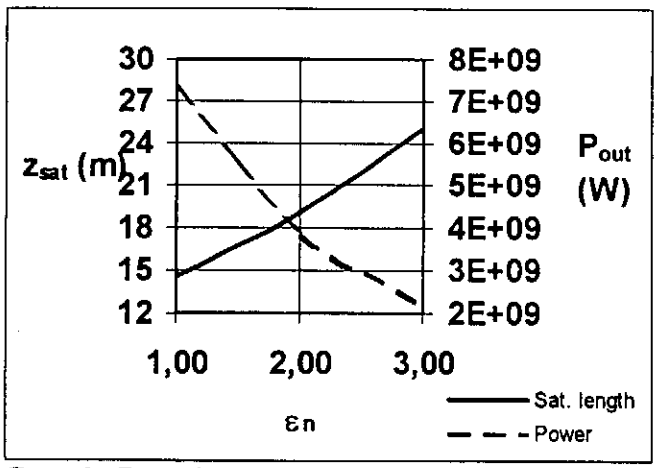

Figure2: Emitted intensity and saturation length at the peak gain as a function of the normalized electron beam emittance, for the nominal energy spread of 0.1%.

In order to determine the performance of the FEL including the undulator field errors, first simulations have been performed with the simulation code TDA3D [10]. The goal is to systematically study the correlation between phase shake and FEL parameters like saturation length and peak power. These simulations will include the undulator plus the superimposed quadrupole focusing. Figure 3 shows the photon flux emitted by the TTF FEL.

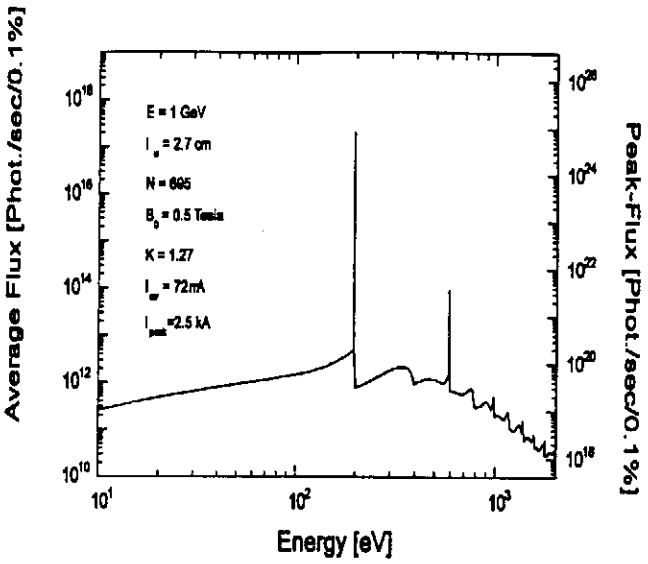

Figure 3: Expected photon flux emitted by the TTF SASE FEL. The two peaks correspond to the FEL emission at the fundamental and 3rd harmonic. The lower curve is the spontaneous emission in the undulator.

REFERENCES

[1] D. A. Edwards (ed.): TESLA Test Facility Linac - Design Report, DESY Print TESLA 95-01 (1995)

[2] R. Bonifacio, C. Pellegrini, I.M. Narducci: Opt. Commun. 50 (1984) 373.

[3] see e.g. W.B. Colson, C. Pellegrini, A. Renieri (eds.): Laser Handbook Vol. 6, North Holland (1990)

[4] J. Fraser, R. Sheffield: Nucl. Instr. Meth. A 250 (1986) 71

[5] B. Carlsten: Nucl. Instr. Meth A 285 (1989) 313

[6] E.T. Scharlemann, W.M. Fawley, SPIE, Vol. 642, 1 (1986)

[7] R.A. Jong, et al.: SPIE, Vol. 1045, 18 (1989)

[8] E.L. Saldin, et al.: DESY Report 94-219 (1994)

[6] C. Travier: Proc. EPAC 94 London (1994) 317

[8] P. Kung, H.-C. Lihn, H. Wiedemann: SLAC-Pub-6507 (1994)

[9] C.-M. Tran, J.S. Wurtele: Comput. Phys. Commun. 54 (1989) 263

[10] P. Jha, J.S. Wurtele: Nucl. Instr. Meth. A331 (1993) 447

[11] R.Bonifacio, et al.: Phys. Rev. Lett., 73 (1994), 70

Beam Position Monitors in the TESLA Test Facility Linac

R. Lorenz, TU Berlin, Einsteinufer 17, 10587 Berlin

Abstract

The transverse position of the beam in the TTF Linac will be measured using two different types of monitors. For the alignment of the quadrupoles a circular cavity was designed because of the desired resolution of 10 μm and the limited longitudinal space. The amplitude of the TM_{110}-mode will be measured in a homodyne receiver, using a signal from the timing system as a reference. Stainless steel prototypes were tested. Furthermore, the single bunch behaviour was measured at the CLIC Test Facility.
Coaxial Striplines will be installed in the experimental area, having a resolution of better than 100 μm. The averaged position of the whole bunch train or the position of an individual bunch will be measured using the amplitude-to-phase conversion.

I. Introduction

In order to establish a technical basis for a superconducting linear collider the TESLA Test Facility is an essential part of the development of injectors, accelerating cavities, cryostat and new diagnostic techniques.
The transverse position of the beam after the injector will be measured using two different types of monitors. For the alignment of the quadrupoles a single circular cavity was designed because of the limited longitudinal space and the desired resolution of about 10 μm in a cold environment (see also [3]). The amplitude of the TM_{110}-mode will be measured in a homodyne receiver, using the seventh harmonic of a 217 MHz timing signal as a reference.
Stripline BPMs will be installed in the experimental area, having a resolution of about 100 μm. For Injector I (bunch spacing of 4.6 ns) the averaged position of the bunch train will be measured using the amplitude-to-phase conversion.

II. TM_{110}-Cavity

The amplitude of the TM_{110}-mode excited in the cavity by an off-center beam yields a signal proportional to the beam displacement and the bunch charge. Its phase relative to an external reference yields the sign of the displacement. Both polarizations of this mode have to be measured to get the displacement in x and y, respectively. For Injector I this system can measure only an average over the bunch train.

A. Prototype Design

The cavity parameters given in Table I were calculated with URMEL, and the measurements were performed on a stainless steel prototype at room temperature (Fig.1). CrNi was chosen as the cavity material to measure individual bunches spaced at 1 μs (Injector II).

After cooling down the structure, the seventh harmonic of 216.7 MHz has to be within the cavity bandwidth to avoid an active tuning system inside the cryostat. The antennae consisting of Kyocera-feedthroughs welded into a special flange, are replaceable to allow a pre-tuning (by adjusting the coupling after welding).

parameter dimension	**at 290 K**	**target**	**sensitivity** $\pm.1$ mm Δ
radius R_0	115.2 mm	114.77 mm	$\mp$1247 KHz
length l	52.0 mm	51.80 mm	$\pm$79 KHz
beam pipe	39.0 mm	37.85 mm	$\mp$610 KHz
theoret. loss factor $[\frac{V}{pC}]$		$k_{110} = 0.242$, $k_{010} = 0.179$	
theoretical unloaded Q		$Q_{110} = 2965$	
measured frequ. [GHz]		$f_{110} = 1.5133$, $f_{010} = 1.04$	
measured coupling		$\beta_{110} = 1.31$, $\beta_{010} = 0.1$	

Table I
Cavity design and measured parameters

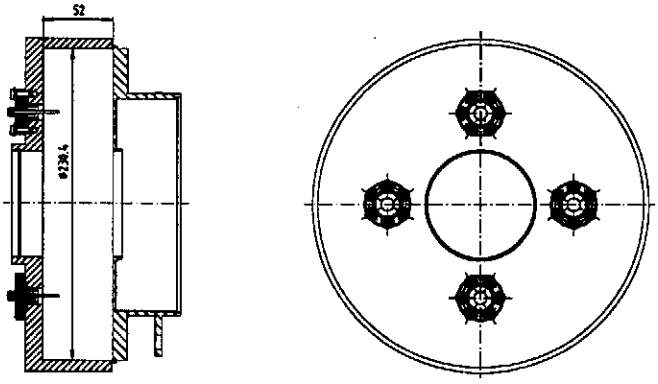

Figure. 1. Cavity BPM

B. Estimated Signals

The resolution near the electrical center of the cavity is limited by the thermal noise of the electronics and the excitation of common modes. For a cavity without beam pipes, the voltage of the TM_{110} excited by a beam at a position δ_x vs. the noise voltage can be estimated as

$$\frac{V_{110}(\delta_x)}{V_{\text{noise}}} = \frac{\delta_x \cdot a_{11}}{2J_1^{\max} R_0} \frac{V_{110}^{\max}}{V_{\text{noise}}} = \frac{\delta_x}{J_1^{\max} R_0} \frac{k_{110} \cdot a_{11} \cdot q \cdot \mathrm{T_{tr}}}{\mathrm{NF}\sqrt{Z_0 k_0 \mathrm{TB}}}$$

where a_{11} is the first root of J_1, $\mathrm{T_{tr}}$ the transit time factor, $q = 32$ pC the bunch charge, k_{110} the long. lossfactor and R_0 the cavity radius (Table I). For a noise figure of NF = 2, the S/N-ratio in a bandwidth $B = 10$ MHz at 293 K is about $139\frac{\delta_x}{\mu\mathrm{m}}$.
Since the field maximum of the common modes is on the cavity axis, they will be excited much stronger than the

TM_{110} by a beam near the axis. The voltage of the TM_{010} with respect to the TM_{110} and the ratio of the spectral densities at ω_{110} can be estimated as ([1])

$$S_1 = \frac{V_{010}(\omega_{010})}{V_{110}(\omega_{110})} = \frac{1}{\delta_x}\frac{\lambda_{110}}{5.4}\frac{k_{010}}{k_{110}} \approx 27 \cdot \left(\frac{\delta_x}{\mathrm{mm}}\right)^{-1}$$

$$S_2 = \frac{v_{110}(\omega_{110})}{v_{010}(\omega_{110})} \approx \frac{1}{S_1}\frac{Q_{110}}{1+2\beta_{110}}\left(1-\frac{\omega_{010}^2}{\omega_{110}^2}\right) \approx 16 \cdot \frac{\delta_x}{\mathrm{mm}}$$

S_1 gives the required frequency sensitive common-mode rejection - about 69 dB for a displacement of $\delta_x = 10\mu$m. But the minimum detectable signal near the electrical center of the cavity is still limited by residual signals at ω_{110} ($S_2 \leq 1$). With a combination of two antennae in a hybrid one gets a field selective filter and a rejection of unwanted common field components at ω_{110}, limited only by the finite isolation of the hybrid between the Σ- and the Δ-port. Finally, we get a theoretical resolution of less than 6 μm for 20 dB of isolation.

C. Signal Processing

We adopted a homodyne receiver scheme (Fig.2), where the amplitude of the TM_{110} and a reference are mixed down to DC. The reference-signal is generated by mixing a 217 MHz-signal from the timing system and amplifying the seventh harmonic. When the beam is on the right, the system can be set up to give positive video polarity. The signal changes the phase by 180° when the beam moves to the left, and for a centered beam it becomes zero.

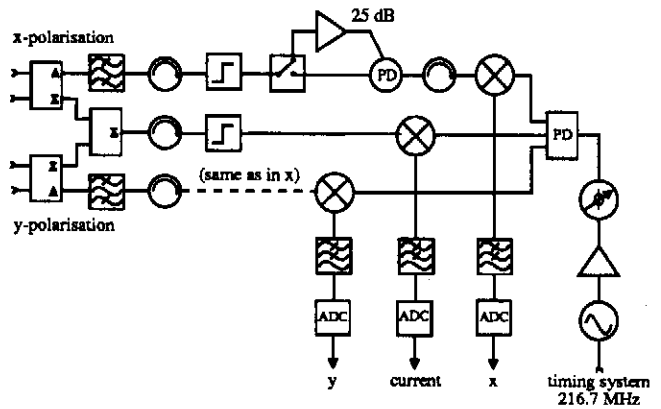

Figure. 2. Signal processing scheme for the cavity BPMs

Due to the limited space, the combination of two opposite antennae was realized outside the cryostat. The tubular bandpass filter has a bandwidth of 100 MHz and a stopband attenuation of more than 70 dB, up to 8 GHz. Together with the hybrid and the coupling factors this gives a frequency sensitive common mode rejection of about 100 dB. Because of the finite isolation of the hybrid and between both polarizations of the TM_{110} (asymmetries in the cavity), the full aperture was divided into two measurement ranges.
The LO-RF-isolation of the mixer determines the dynamic range of the electronics. By using a Quadrature IF Mixer, no additional phase stabilization for the reference would be required. An isolator was inserted between the filter and the mixer to reduce reflections and error signals due to second-time mixing.
After passing a low-pass filter and a bipolar video amplifier, the signal may be either viewed directly on an oscilloscope for adjustment, or digitized and used for the quadrupole alignment. All data of the 12-bit ADC-board can be read out between two bunch trains and the normalization will be done in a computer.

D. Test Results

Bench tests were carried out on a stainless steel prototype to determine the resolution near the center and to test the electronics. Therefore the cavity was excited by an antenna, fed by a network analyzer. A resolution of about 5 μm was measured in the frequency domain (narrowband) and in the time domain (impulse response) by moving the cavity (Fig.3 and Fig.4, see also [3]).

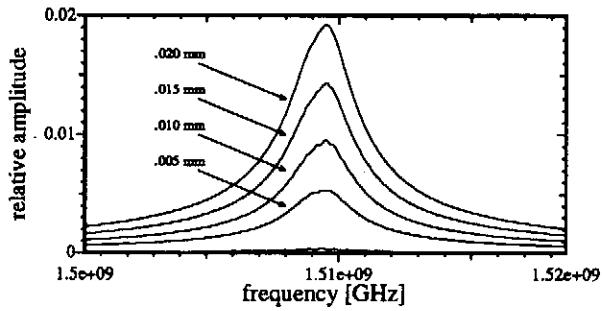

Figure. 3. Bench-test - Narrowband output vs. position

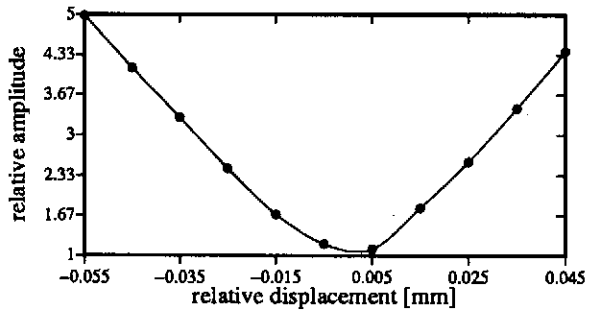

Figure. 4. Bench-test - Impulse response vs. position

To get similar responses in a real time domain measurement and for testing the electronics, a pulser ($t_w \approx 370$ps, amp $\approx$ 16V) was built to excite the cavity. The filtered Δ-port signal was mixed down to DC and displayed on an oscilloscope triggered by the sum-signal of the hybrid. Since the pulser was not very stable with respect to its amplitude, it was impossible to measure the min. resolution.
In addition, a prototype was tested at the CLIC Test Facility at CERN to demonstrate the principle single bunch response of the monitor and to measure the amplitude of the TM_{110}-mode as a function of the relative beam displacement. Therefore, the BPM was installed in the spectro-

meter arm and the beam was moved vertically by changing the current of the steering coil.
Since no LO-signal at 1.51 GHz (phase-related to the beam) was available, four different LO-schemes were tested. In one scheme a 250 MHz- signal from the timing system was fed to a step recovery diode and the 6th harmonic was mixed with the Δ-signal. Figure 5 shows the output of the electronics vs. the relative beam position.

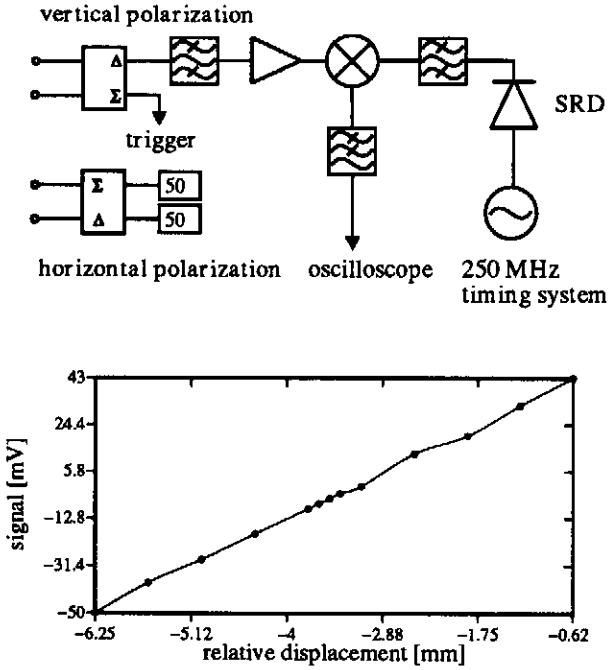

Figure. 5. CTF-test - Output versus rel. position

Unfortunately, due to the measurement position, the mechanical setup and some machine parameters it was impossible to measure the minimum detectable signal near the monitor center.

III. Stripline Monitors

Stripline monitors were selected for the experimental area and a temporary beamline because of the relaxed requirements - 100 μm resolution around the center - and the warm location. All monitors will consist of four 50 Ω coaxial striplines, positioned 90 degrees apart in azimuth (Fig.6). The housing for the one in the dipole arm will be slightly modified due to the elliptical beam pipe.
The BPM body is machined from a single block of stainless steel, and four holes and the beam aperture are drilled (similar to the structure described in [4]). Each electrode is 175 mm long, has a geometrical coupling factor of about 2 % and is shortened at the end. To reduce standing waves on the electrode, the transition from the electrode through the feedthrough into the cable was optimized up to 6 GHz. The main distortion is caused by the feedthrough. A prototype was built by DESY-IfH Zeuthen and is under test.
The signal processing electronics have to measure the Δ-signal and the Σ-signal of two opposite electrodes to calculate the position in one direction. Because of the small charge per bunch and the multibunching, an amplitude-to-phase conversion scheme was adopted. Its basic component is a device which transforms the amplitude ratio of two input signals into a phase difference, usually a $\frac{\pi}{2}$-hybrid. The generation of a normalized output (position versus current) over a wide dynamic range is the main advantage of this system.

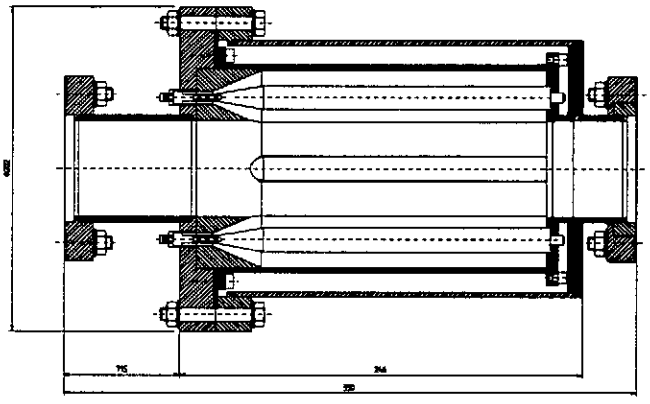

Figure. 6. Stripline BPM

Analog electronics will be built by INFN Frascati and a prototype will be tested this summer. The signal coming out of the phase detector may be either viewed directly on an oscilloscope or digitized using a 12-bit ADC-board.
This system will be appropriate to measure individual bunches spaced 1 μs for Injector II, too. Another alternative is to adopt the SLAC-system, where the signals of each electrode are individually stretched, amplified, held at their peak value and than digitized.

IV. Acknowledgements

The author would like to thank DESY-IfH Zeuthen for building several prototypes and the realization of the stripline monitor. Special thanks are extended to Hans Braun from the CLIC/CTF group for his help in the preparation and realization of the tests.

References

[1] W. Schnell, "Common-mode rejection in resonant microwave position monitors for linear colliders", CLIC note 70, CERN-LEP-RF/88-41
[2] R. Shafer, "Beam Position Monitoring", AIP Conference Proceedings 212, 1989, pp. 26-58
[3] R. Lorenz, K. Yezza, "Test results on a Beam Position Monitor Prototype for the TTF", in Conference Proceedings of the EPAC 94, London, July 1994, pp. 1536-1538
[4] J. Hinkson, K. Rex, "A Wideband Slot-Coupled Beam Sensing Electrode for the Advanced Light Source (ALS)", IEEE Conference Proceedings of the PAC 91, San Francisco, May 1991, pp. 1234-1236

Response of Superconducting Cavities to High Peak Power*

T. Hays, H. Padamsee, Laboratory of Nuclear Studies, Cornell University, Ithaca, NY 14853 USA

Abstract

A technique to find the transient cavity Q from transmitted power is presented. This technique can facilitate finding the Q as a function of accelerating electric field for low power pulsed measurements, but it has a special application to analyze the thermal breakdown behavior during high peak power pulsing. With high power, in short time scales, the fields in a superconducting cavity can be driven well past the CW breakdown limit. With knowledge of the Q during breakdown, one can show that a large fraction of the surface was still superconducting as the cavity reached high fields. A lower bound to the critical RF magnetic field can then be determined.

Results of pulsing a 1.3 GHz Nb cavity with 340 kW for 150μs are presented. The Q extraction technique is used to measure a lower limit of H_c^{RF} over the range of 2 K to 8.3 K despite the presence of a thermal defect.

I. INTRODUCTION

As we continue to push the achievable accelerating gradients in Nb cavities, the critical RF magnetic field, H_c^{RF}, will eventually show up as a hard limit. Improvements in Nb purity and processing of field emission have already advanced practical accelerating gradients above the 25 MV/m level.[1] How much farther can Nb be pushed? When is it time to abandon Nb in favor of other superconductors such as Nb_3Sn that have higher DC critical fields? Is the H_c^{RF} of Nb_3Sn films significantly higher than bulk Nb?

The difficulty in answering these questions is largely due to the presence thermal defects that quench the superconductivity and prematurely limit the sustainable surface magnetic field. In CW operation, in addition to the defect's particular characteristics, the quench field is dependent upon the specifics of the steady state heat transfer. Thus improving the thermal conductivity of Nb serves to raise the quench field. A small normal conducting "hot spot" can be sufficiently cooled and contained to avoid thermal runaway. If the cavity fields are raised above this CW quench field, the normal region grows to eventually encompass the cavity, but this growth takes a finite amount of time.

With high peak power pulsing, the cavity fields can be quickly raised well above the CW quench field while the normal region is growing. To determine H_c^{RF} from this, one must be sure that the cavity is still superconducting at the relevant high field region. A new technique is presented that allows calculation of the instantaneous cavity Q any time during the filling or decay. By knowing Q, one can estimate the size of the normal region and ensure that H_c^{RF} is measured at a superconducting surface. In the present work, we use this technique to measure H_c^{RF} of a 1.3 GHz Nb cavity for temperatures from 2.1 K up to 8.3K.

In addition, since the accelerating field is known at every instant, this Q extraction technique can be used to quickly determine Q vs E_{acc}. Application in this manner is the subject for further work.

II. FINDING INSTANTANEOUS CAVITY Q

In what follows, the differential equation of the cavity state is derived and solved for Q_0. Consider a cavity driven on resonance with one coupler. By conservation of energy we can write

$$P_f = P_{diss} + P_r + \frac{dU}{dt}. \tag{1}$$

where

P_f	=	forward power (toward the input coupler)
P_{diss}	=	cavity dissipated power
P_r	=	reverse power
U	=	stored energy (inside the cavity)
t	=	time.

The only tricky part about this expression is the reverse power which satisfies

$$P_r = \left(\sqrt{P_f} - \sqrt{P_e}\right)^2 \tag{2}$$

where

$$P_e = \omega U / Q_{ext}. \tag{3}$$

Q_{ext} is the "external" Q of the coupler.

Equation (2) indicates that the net reverse wave results from a superposition of a wave reflected off the input coupler and a wave being emitted from the cavity. Substituting (2) into (1) and using

$$P_{diss} = \frac{\omega U}{Q_0} \tag{4}$$

for the cavity losses and

$$\frac{1}{Q_L} = \frac{1}{Q_0} + \frac{1}{Q_{ext}} \tag{5}$$

for the "loaded Q" as well as (3) we arrive at a differential equation for stored energy:

$$\frac{dU}{dt} = 2\sqrt{\frac{P_f \omega U}{Q_{ext}}} - \frac{\omega U}{Q_L}. \tag{6}$$

A clearer form results when written in terms of the fields ($\propto \sqrt{U}$).

$$\frac{d\sqrt{U}}{dt} = \frac{1}{2\tau_L}\left(\sqrt{U_0} - \sqrt{U}\right) \tag{7}$$

where

$$U_0 \equiv \frac{4\tau_L{}^2 \omega P_f}{Q_{ext}} \tag{8}$$

is the steady state stored energy.

Equation (7) shows that the cavity has a natural time constant τ_L for response and that the field changes at a rate proportional to the displacement from its equilibrium value.

If the cavity-coupler system had more than one coupler, (1) would have an additional term with the form of (3) for the

*Work supported by the NSF with supplementary support from the U.S.-Japan Cooperative Agreement

emitted power of each coupler. The only effect this has on the subsequent equations is to require that the definition of "loaded Q" in (5) have an additional $1/Q_{ext,k}$ term for each of the k new couplers.

From (7) and (2) the time dependent cavity behavior can be determined analytically or numerically.

The above treatment gives $U(t)$ from Q_0 (and other variables) but to go the other way, one has only to solve for Q_0 in (7) to get

$$\frac{1}{Q_0} = \frac{2\left(\sqrt{\frac{P_f\omega}{Q_{ext}}} - \frac{d\sqrt{U}}{dt}\right)}{\omega\sqrt{U}} - \frac{1}{Q_{ext}}. \qquad (9)$$

Again, if there are k additional couplers, they would show up as further $1/Q_{ext,k}$ terms subtracted from the right side of (9).

Equation (9) is useful for extracting the $Q(t)$ or the $Q(E)$ behavior of a cavity during pulsed operation. And unlike previous methods of getting $Q_0(E)$ from a pulse that examined only the cavity decay[2], this technique can be used any time the cavity has energy. This method also improves over past methods in that it requires only the instantaneous values of U, $d\sqrt{U}/dt$, and P_f. The cavity's history (or future) need not be considered, and no functional fits are needed.

If the cavity is grossly overcoupled ($Q_{ext} \ll Q_0$) then Q_0 plays little role in determining the shape of $U(t)$. For the overcoupled case, in order to extract Q_0, $U(t)$ must be known to first order within a fractional error of Q_{ext}/Q_0. When Q_0 does have a negligible contribution, one can take advantage of this to extract Q_{ext}. When ($Q_{ext} \ll Q_0$), Q_{ext} can be found by

$$\frac{1}{\sqrt{Q_{ext}}} = \frac{\sqrt{P_i} \mp \sqrt{P_i - \frac{dU}{dt}}}{\sqrt{\omega U}} \qquad (10)$$

where the negative sign is used when d^2U/dt^2 is positive and vice versa.

III. EXPERIMENTAL APPARATUS

Cavities of the DESY shape (1.3 GHz) are tested using a high power klystron and modulator system[3] capable of providing 1.5 MW for 270 μsec. Currently input coupler limitations allow the full 1.5 MW to be used only when the pulse length is reduced to ~150 μsec.

Results presented here are for a single cell cavity made from Russian Nb sheets with a starting RRR of 460±150. Subsequent solid state gettering with Ti resulted in a RRR of 1825 ± 700[1]. Because the cavity's resonance was not at the center frequency of the klystron, the experimental results presented here were limited to a peak power of 1 MW.

Germanium thermometers were mounted on each beam tube to monitor the cavity temperature and any thermal gradient. Three Allen-Bradley resistor thermometers were mounted on the cavity equator to observe fast temperature changes as a result of pulsing. Measurements of incident and transmitted power during pulsing are made by crystal detectors monitored by an 8-bit digital storage oscilloscope (Tektronix 2212). The oscilloscope traces are acquired and processed by a Macintosh computer running LabVIEW software.

[1]The RRR measurements were done on small witness samples.

IV. PULSING TO REACH H_c^{RF}

It is thought that H_c^{RF} is equal to the superheating critical field, H_{sh}, a metastable state above the thermodynamic critical field, H_c.[4] H_{sh} can be achieved in RF because the nucleation time for flux penetration is much longer than an RF period.[5] The race to beat the growth of the normal conducting region requires that the cavity fields be ramped up to H_c^{RF} in less than 100 μs, the faster the better. To do this a very strong input coupling ($Q_{ext} \simeq 10^6$) is used. Higher couplings could ramp the fields faster but that would result in too much of a sacrifice in the measurable range Q_0.

Oscilloscope traces of up to 1 MW peak power pulses to the liquid helium cooled Nb cavity were acquired at 2.1 K and 4.2 K. By warming the cavity we hoped to be able to lower H_c^{RF} enough to come close to it even with the thermal breakdown. To prepare for warmer measurements, the cavity was cooled with flowing gaseous helium at 4.2 K and the fast pulsed breakdown behavior was found to be similar to that of liquid cooling. There was the worry that the cavity would have a different thermal breakdown behavior due to the inferior cooling power of the gas, but the time scales are so short that the cold reservoir outside the cavity doesn't have time to play a large role in the heat transfer.

Bathed by flowing helium gas, the cavity was slowly warmed up to its transition temperature 9.25 K while high peak power pulsed measurements were made (with $Q_{ext} = 9 \times 10^6$ and $P_f = 340$ kW). Two such pulses and the extracted Q_0 are presented in Figure 1. At the beginning of the pulse, Q_0 is too high to measure, but as the normal region grows, Q_0 plummets until it reaches the value of a completely normal cavity. As the temperature is raised from Figure 1 a) to 1 b), the breakdown field is lower, and Q_0 drops earlier. Note that because of the strong coupling and high incident power, the cavity fields continue to rise despite the plumetting Q_0. Since the cavity is almost completely normal conducting at its peak field, it is vital to extract Q_0 while the fields are rising to be able to measure a lower bound to H_c^{RF} with confidence.

At the beginning of the pulses in Figure 1, Q_{ext} was sucessfully extracted using Equation (10). The value thus obtained agreed well with independent measurements of Q_{ext}.

The 8-bit amplitude resolution on the oscilloscope was the most serious limitation to the data. Averaging was required get rid of a little noise and to remove the "steps" caused by this resolution limit.

To be positive that there is a superconducting surface reaching the peak field, we claim the cavity must be at least 90% superconducting. Since the 10% normal region occupies the area around the local defect, it is assured some part of the high field equatorial region of the cavity is superconducting.

A conservative calculation then dictates that Q_0 must be at least 2×10^6. Applying this criterion to the pulses measured yields the data in Figure 2. The two lowest temperature data points were acquired using liquid helium cooling at 2.1 K and 4.2 K with higher peak power and greater input coupling. Because the breakdown occurred so early in the pulse, testing the cavity much above 8.3 K gave inconclusive results.

For comparison, criticial magnetic field curves for Nb are also shown in Figure 2. The curve for H_{sh} is obtained from

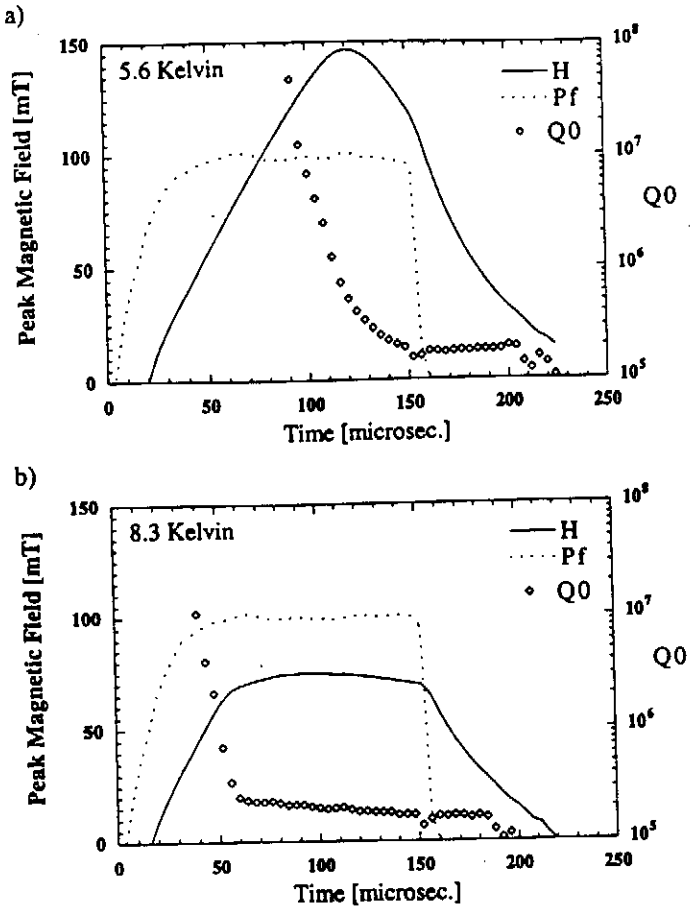

Figure 1. Pulses to the cavity causing thermal breakdown at a) 5.6 K and b) 8.3 K. Peak forward power was 340 kW for both pulses. Forward power is shown with arbitrary units.

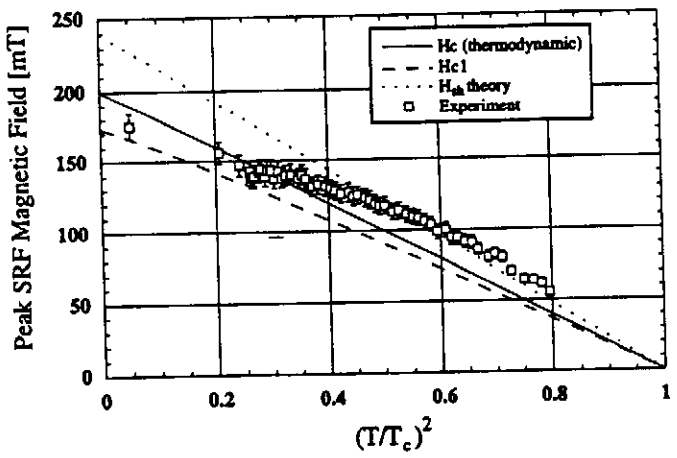

Figure 2. Measured surface magnetic fields on the superconducting Nb surface compared with DC critical fields[6] and a reasonable guess at H_{sh}.

the simplistic assumption that $H_{sh}(0) = c_{sh}H_c$ with $c_{sh} = 1.2$ throughout the temperature range. The exact values are not easily predicted, but because of the temperature dependence of the Ginsburg-Landau parameter it is expected that c_{sh} is lower for lower temperatures and higher closer to T_c. One might think that it is suggestive that the experimental data in Figure 2 also follows this trend, but the stronger influence of the thermal defect on the lower temperature points is probably dominating the shape.

Note that these first experimental measurements are tentative. Improvements in the reliability of power measurements and better data resolution are in progress.

V. CONCLUSIONS

The new Q_0 extraction technique was successful in exploring high magnetic fields in a superconducting cavity despite the presence of a thermal defect. Measurements on Nb up to 8.3 K are consistent with the idea that H_c^{RF} is the superheating critical field. These measurements suggest that high magnetic field studies of Nb_3Sn are feasible using this Q_0 extraction tool.

VI. ACKNOWLEDGMENTS

We wish to thank our colleagues W. Hartung for helpful criticism on the theory, J. Sears for assistance in cavity purification, and E. Chojnacki for help with the klystron. Thanks go to K. Hosoyama from KEK for assistance with the helium gas cooling. We are also grateful to the many members of the international TESLA Collaboration that aided in setting up the 1.3 GHz cavity test facility at Cornell.

VII. REFERENCES

[1] C. Crawford et al. *Particle Accelerators*. Vol. 49, pp. 1-13 (1995).

[2] D. W. Reschke and R. W. Roth *Fundamentally Fastest Method Measuring $Q_a(E_{acc})$ - Performance of S.C. Cavities* Fachbereich Physik, Bergische Universitat Wuppertal, Germany. Presented at the 6th Workshop on RF Superconductivity at CEBAF in Newport News, VA, USA.

[3] ibid. Ref. [1].

[4] J. Matricon and d. Saint-James *Phys. Lett.* **24A**, 241 (1967).

[5] R. B. Flippen *Phys. Lett.* **17**, 193 (1965).

[6] D. K. Finnemore, et. al. *Phys. Rev.* **149**, 231 (1966).

Microscopic examination of defects located by thermometry in 1.5 GHz superconducting niobium cavities*

J. Knobloch, R. Durand, H. Muller and H. Padamsee
F.R. Newman Laboratory of Nuclear Studies, Cornell University, Ithaca NY 14853

Abstract

A new high resolution, high speed thermometry system has been built at Cornell to permit the study of anomalous loss regions in 1.5 GHz superconducting Nb cavities in superfluid He. Following a cavity test, the cavity is dissected for examination of these regions in an electron microscope. Presented is a survey of the topographical and elemental characteristics of various defects found so far. Included are field emitters which were known to be active at the end of a cavity test, as well as those which processed.

I. INTRODUCTION

In present day Nb cavities the surface magnetic fields achieved still fall far short of those theoretically attainable. The maximum field possible is believed to be the superheating rf field (2300 Oe @ 1.6 K) [1]. In practice, though, one finds that the cavity Quality (Q) already begins to drop between 300 and 1000 Oe.

Several mechanisms responsible for anomalous power dissipation at these fields have been identified. Presently, the most common ones are dielectric/magnetic losses (thermal defects) [2] and field emission (FE) [3]. Both mechanisms can be attributed to microscopic defects present on the inner cavity wall.

To better understand the nature of the defects we have begun to search for these, using thermometry [2] as a guide. We catalogue their heating characteristics and after cavity tests dissect the cavities to undertake a microscopic and elemental examination of the defects.

II. EXPERIMENTAL SETUP

To facilitate the search a new thermometry system was developed, whose details have been discussed elsewhere [4]. It is designed for L-Band cavities operating in superfluid He at 1.6 K. Its essence is an array of 756 specially prepared carbon thermometers pressed against the outer cavity wall. A map at a resolution of 0.25 mK takes about 1/10 s to acquire. Increasing the acquisition time to 2.5 s permits us to resolve 30 μK signals. This is a marked improvement over previous systems which either were very slow, requiring several tens of minutes for an acquisition, or were unable to detect signals below 5 mK.

After the tests, cavities that have interesting sites are cut apart. During the cutting process the interior of the cavity is pressurized with filtered N_2 gas, thereby minimizing dust contamination. Cuts are made along the beam tubes (~ 2.5 cm from the iris) and along the equator using two sizes of conventional pipe cutters. The entire cutting process is carried out in a class 100 clean room.

The chamber of an electron microscope (SEM) has been enlarged to permit the examination of the half cells. We have been able to show that thermometry data is a useful guide to locating defects in the SEM. The defects' elemental composition is also studied by energy dispersive x-ray analysis.

The heating due to thermal defects occurs directly at the defect site. On the other hand, field emitters are more difficult to pinpoint. Generally one detects the power deposited by accelerated FE electrons impacting with other parts of the cavity wall. In that case we revert to trajectory calculations using the program "MULTIP" to determine the emitter location [5].

III. MEASUREMENTS

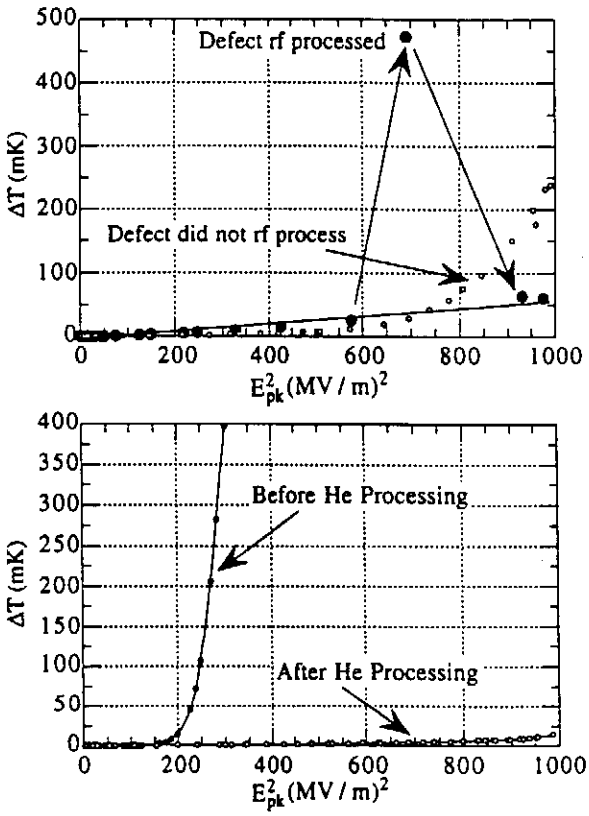

Figures 1a & 1b: FE heating measured for sites which a) didn't process (shown in fig. 2b), b) processed in the rf field (shown in fig. 2c) and c) He processed (shown in fig. 2d). The heating is plotted vs. the electric field squared so that background heating in the absence of FE is linear.

All of the cavities discussed here had been tested in the past. For the most recent test all but one (LE1-Hereaus) were

Work supported by the NSF with supplementary support from the US - Japan foundation

Presented at the 1995 Particle Accelerator Conference, Dallas TX

chemically etched with BCP 1:1:2 for 3 minutes. This was followed by rinsing the cavity with continuous flow deionized water for at least 2 hours prior to drying with warm filtered N_2 gas. LE1-Hereaus was only cleaned with DI water in conjunction with ultrasonic agitation.

During the tests the cavity fields were increased while measuring the cavity Q and temperature distributions at regular intervals. In one case an emitter *rf processed* [6], that is, upon raising the field beyond a threshold, the emitter's heating was permanently extinguished. (see fig. 1a).

In another case, the maximum power dissipated in the cavity was 8 W, most of which was absorbed by a single emitter. Subsequently *He processing* [7] was successfully performed on the cavity resulting in the elimination of the emitter (fig. 1b).

IV. RESULTS & DISCUSSION

On average we found the temperature signals of two or three FE sites in each cavity. LE1-Hereaus, which had far more, was the exception. This was not surprising, considering this cavity had not been etched prior to the test.

Of the nine FE sites studied in greater detail, six were located in the bottom halves of the cavities. This observation supports the notion that emitters are primarily caused by foreign particles, accumulating at the bottom due to gravity.

In two cases a microscopic search of an area ±1 cm and ±10° centered on the predicted emitter location failed to turn up any defects that were indicative of FE (discussed later).

In the remaining seven cases we found defects displaying definite signs of FE within at most a 2-3 mm radius of the predicted emitter location. Table 1 summarizes these. Frequently we also searched the surrounding area. Although occasionally we did find micron sized particles, these did not show any signs that FE had occurred and could easily be removed by high pressure N_2 gas, whereas the FE sites remained anchored to the cavity surface.

Table 1: Summary of the emission sites for which microscopic defects could be correlated with the thermometry signals.

#	Melting/Craters Present ?	Star-burst?	Pro-cessed?	Contami-nants	Fig.
1	Minimal Melt.	No	No	Fe, Cr	2a
2	Melting	No	No	In, Al	None
3	Minimal Cratering	No	No	C,O,Fe,Ni, Cr,Ti,Ca,Br	None
4	Min. Cratering	Yes	No	None	None
5	Severe Melting	Yes	No	C,O,Cl, Ti	2b
6	Significant	Yes	Yes	C	2c
7	Very Severe	Yes	w/ He	None	2d

Cataloging field emitters

The defects listed above can be categorized as follows:

A) Three unprocessed FE sites (entries 1-3) consisted of foreign particles a few 10's of μm in size which had been partially melted. Fig. 2a shows an example of such a defect. Note the molten region which is magnified in the inset.

B) In two unprocessed cases (entries 4 & 5) we found regions of limited cratering surrounded by a large area (diameter = 500 μm) of reduced secondary electron emission coefficient. This feature has been observed in the past [3],[8] and is known as a starburst because of its dark star shaped appearance in the SEM. In the case of entry 5, we also found a large (70 μm) foreign particle which had melted to a large extent (see fig. 2b)

C) At the location of the rf processed emitter (entry 6) we found an irregularly shaped starburst surrounding a region of significant cratering and melting (see fig. 2c) Some remnants of a foreign particle (carbon) existed as well.

D) The helium processed emitter (entry 7) had a very regularly shaped starburst (see fig. 2d). No foreign elements were detected at the center which consisted entirely of severely molten Nb surrounded by some cratering.

Progression of field emission:

These results suggest the following scenario for the progression of FE:

1. At sufficiently low current densities the FE process is insufficient to alter the appearance of the emitter. This explains why we were unable to find some field emitters in the microscope.

2. As the electric field is increased, the FE current density rises locally to values sufficient to melt parts of the site (fig. 2a). FE may perhaps occur at several points on the defect simultaneously, so that the melting process doesn't noticeably affect the defect's collective FE characteristics.

3. Further field increases result in extreme heating (ultimately leading to a local explosive event). A plasma builds up, which is fueled by desorption/evaporation of one or more of the local emitters. Through a cleaning action of the plasma, a starburst is produced [8] (fig. 2b). Neighboring emitters may still be in the first two stages, so that again the overall FE characteristics of the defect are only little changed.

4. Finally, the plasma itself results in significant heating over a region encompassing a large portion of the defect. Once a critical temperature is exceeded the entire defect processes (fig. 2c). The emitter in fig. 2b was perhaps just before this stage. Of particular note is the fact that almost the entire defect seems to have melted.

The new evidence presented here supports that the plasma production is not simply the result of a defect's processing event. Rather it is the heating by the plasma that is essential to its extinction. The heating by the FE current alone may not be sufficient.

The He processed emitter evidence tends to support this notion. The He provides the 'fuel' to enhance the plasma, thereby permitting the defect to process at lower field levels than would ordinarily be possible.

This scenario, of course, is speculative and we are currently running simulations to test our hypothesis. Further cavity tests will be carried out to yield more statistics.

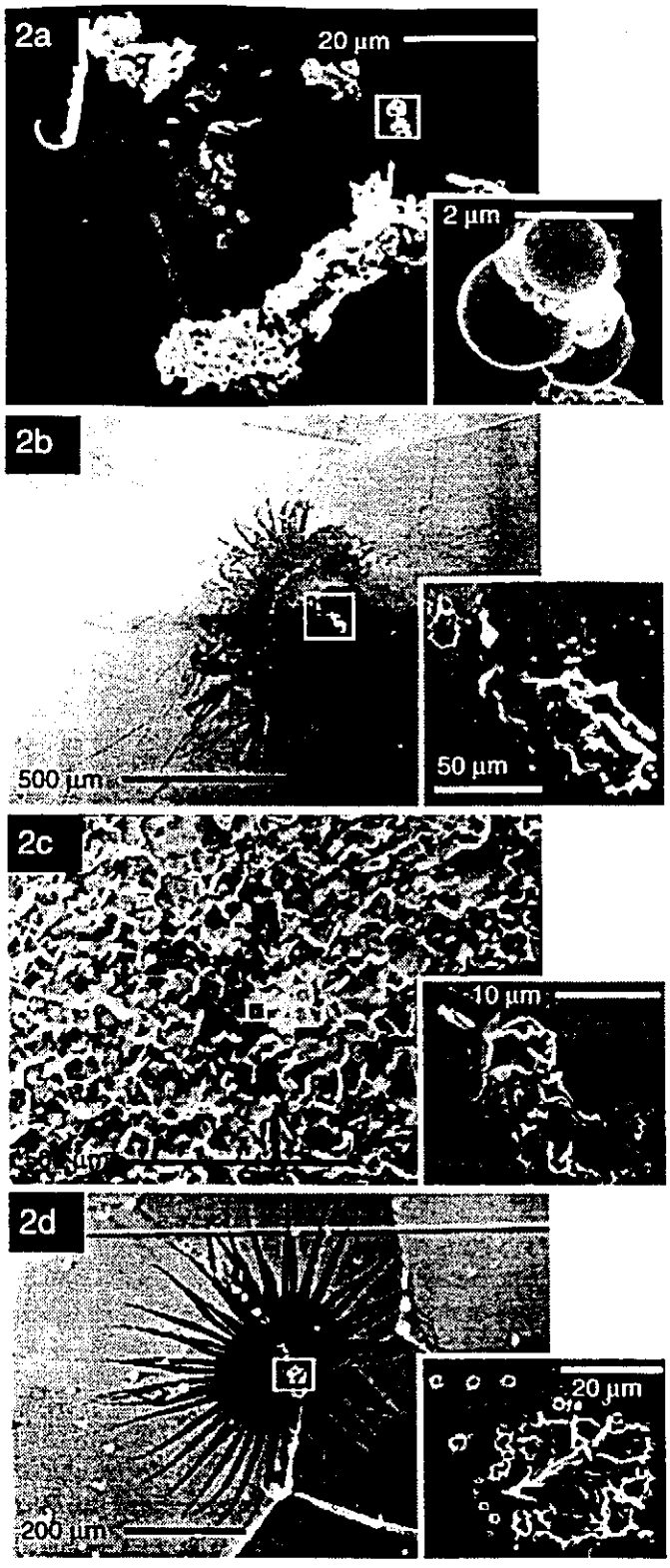

Figures 2a - 2d: Examples of FE defects found for the four cases A - D discussed in the text. It is speculated that these figures represent a natural progression in FE, ultimately leading to the processing of a defect. The insets are magnifications of the areas in the rectangles.

Other Observations:

1. We found a thermal defect (fig. 3), which at higher field levels could have lead to thermal breakdown. The copper particle at that location could not be removed by high pressure solid CO_2 cleaning. Parts of it seem to have melted, which may explain why the particle was so firmly attached. Calculations [9] indicate that melting was possible at the fields attained, provided the particle was thermally isolated.

Figures 3a & 3b: A thermal defect (copper)

2. Comparison with other experiments show that the average starburst size scales inversely with frequency between 1.5 and 5.8 GHz. If starbursts are produced during half an rf cycle, while FE is active, we find that an expansion velocity of $\sim 10^6$ m/s is required. This is consistent with the expansion of electrons thermally emitted from plasmas observed during explosive DC FE [10]. Perhaps such electrons are responsible for the starburst production.

3. Generally, cavities were FE free until a threshold field was exceeded, resulting in the irreversible activation of at least one field emitter. Room temperature cycling of the cavity did not deactivate these. This observation seems to be at odds with the use of the "*tip-on-tip*" model [11] to explain FE.

4. The main contaminants in emitters were C, Fe, Cr and Ti, which probably came from assembly tools and the ion pump. Steps are being taken to modify the pump system.

V. REFERENCES

[1] H. Piel, CERN Acc. School (1988) page 149
[2] H. Piel, Proc. of the Workshop on RF Superconductivity, Karlsruhe (1980), page 85
[3] D. Moffat et al., Particle Accelerators 40, (1992), page 85
[4] J. Knobloch et al., Rev. Sci. Instrum., 65 (11), (1994) page 3521
[5] J. Graber et al., Nucl. Instr. and Meth. in Phys. A 350, (1994) page 582
[6] J. Graber, Ph.D. Thesis, Cornell University
[7] H. Schwettmann et al., J. Appl. Phys. 45, (1974) page 914
[8] T. Hays et al., Proc. of the 6th Workshop on RF Superconductivity, CEBAF (1993) page 750
[9] J. Graber, Cornell University, private communication
[10] E. Litvinov, IEEE Transactions on Electrical Insulation, EI-20 (4), (1985) page 659
[11] M. Jimenez at al., J. Phys. D. **27**, (1994) page 1038

AN ADVANCED ROTATING T-R MAPPING & ITS DIAGNOSES OF TESLA 9-CELL SUPERCONDUCTING CAVITY

Q. S. Shu, G. Deppe, W-D. Moeller, M. Pekeler, D. Proch, D. Renken
P. Stein, C. Stolzenburg, DESY, Hamburg 22603, Germany
T. Junquera, A. Caruette, M. Fouaidy, IPN (CNRS - IN2P3) Orsay, France

Abstract

An advanced rotating temperature and radiation mapping has been developed for investigation of field emission & thermal breakdown of TESLA 9-cell superconducting cavities in superfluid He. More than 10,000 spots on cavity surfaces can be investigated in one turn with 5^{o} angular stepping. We locate a heated area with maximum ΔT=3.3K around the 5th cell's equator. A heat flux density of 5 W/cm^2 in the region ΔT=3K and total heat power Q~100W going to LHe from the area were calculated. An emitter responsible for the heating was identified at the iris area (So=8cm) of the same cell according to T-maps associated with a simulation of impacting electron trajectories. The cavity reached Eacc=20 MV/m. We briefly introduce the technical layout, experimental data and analysis results. The surface scanning thermometers, mechanical structure, moving adapting device and a fast data acquisition are discussed in detail in [1], [2].

I. INTRODUCTION

A. Field Emission and Thermal Breakdown

Great progresses have been achieved in pursuing high accelerating gradients of superconducting cavities due to the world-wide efforts [3]. However, the field emission (FE) and thermal breakdown (TB) are still the main obstacles preventing SRF cavities from confidently reaching Eacc = 25 MV/m, the TESLA's goal (TESLA is an international effort for the TeV Energy Superconducting Linear Accelerator).

B. T-R Mapping

Most of the FE sources and TB defects on the inner RF surfaces of cavities are submicro-sizes [4] and activated only at high RF fields while cavities in a superconducting state. The main approaches to understand the FE and TB are to study the hot spots and radiation (X-rays induced by impacting FE electrons) on the cavity surfaces during RF operation. Various advanced T and/or R mapping have been developed and comprehensively used at CERN[5], Cornell [6], DESY, Saclay [7] and Wuppertal [8]. T-R mappings can be classified into two categories:

(1) Fixed Mapping: Thermometers (and/or photodiodes) are fixed on the surfaces of cavity. They have higher thermometer efficiency (using grease as bounding agent) in HeII and simpler mechanical structures than rotating one. However, some 700 of thermometers are needed for an one-cell 1.5 GHz cavity [6].

(2) Rotating Mapping: For a 9-cell 1.3 GHz cavity, a rotating T-R mapping uses about 100-150 of thermometers instead of ~ 6,000 (9x700). The thermometer efficiency. accuracy and reproducibility are highly depending on the heat transfer condition at the sensor location on the cavity wall

The rotating mapping recently developed at DESY combines measurements of T & R for TESLA 9-cell cavities (a complicated geometric structure). Therefore, rather sophisticated mechanical design and surface scanning thermometers is needed to meet all the performance requirements in superfluid He.

II. TECHNICAL LAYOUT

Total 116 specially developed surface scanning thermometers [2] and 32 photodiodes (PIN Silicon/S 1223-01) are assembled into 9-rotating arms as shown in Figure 1 A, B. The thermometer enhance the thermal contact with cavity by a silver tip while isolated from HII with an epoxy housing. Due to a reinforced structure of TESLA cavity, the thermometers can not directly touch the surfaces of cavity iris. Considering the electrical fields reach maximum at iris, 4 photodiodes are mounted in the end of each arm to monitor FE induced X-rays while 14 thermometers are used to monitor the temperatures in the entire region between irises of ach cell. Only 9 thermometers are at the first and last arms.

A driving and suspending structure in superfluid He is

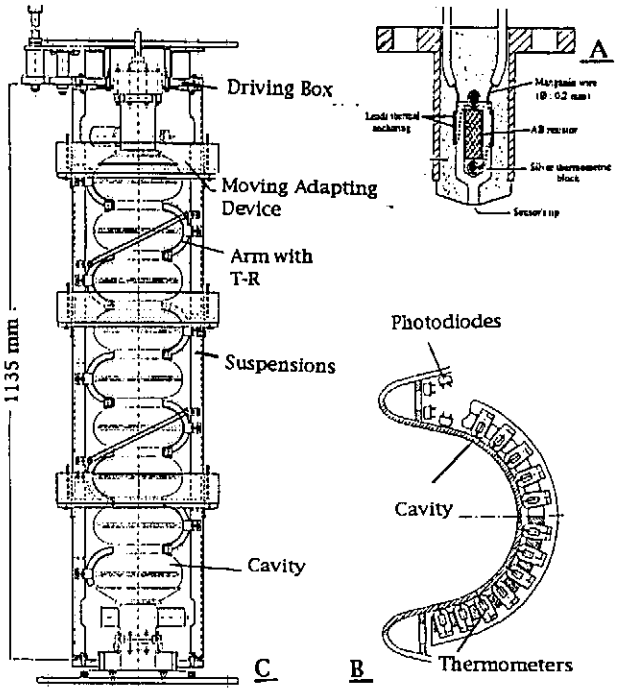

Figure 1: (A) A superfluid He scanning thermometer. (B) A rotating arm. (C) The DESY rotating T-R mapping without rotating measuring cables.

designed to gently turn the arms around and uniformly press the thermometers (through a spring-holder structure, P=100 g

per thermometer) onto the cavity surfaces. A large number of electronic measuring cables have to move with the rotating arms when the T-R mapping rotates. These cable become very rigid in LHe. A moving adapting device is successfully designed to overcome the problem. The space in the TTF vertical cryostat is very constrained that makes the mapping design even more difficult.

Driven by a computer-controlled stepping motor, the T-R arms can be automatically turned to any expected position on the cavity with a accuracy of 1 degree. More than 10,000 spots on cavity surfaces can be investigated in one turn with 5^{o} angular stepping. Two Ge-thermometer and three additional scanning thermometers are used to monitor the change of bath temperature during measurement. Maps can be taken with auto-scanning of entire cavity surface or scanning with time in a fixed position. The effective resolution of temperature measurement is less than 5 mK. One longitudinal measurement in a fixed angular position can be completed in less than 10 ms. All data taken, control and display are performed by a Sun-station computer with a LabView^{TM} language program. Figure 1 C shows the assembly of TESLA T-R mapping without cabling system. The technical aspects will be presented in detail at [1].

III. TEST AND DIAGNOSES

A TESLA prototype cavity -1 has reached 20 MV/m as shown in figure 2. Previously, cavity -1 had been limited by thermal breakdown at about Eacc = 10 MV/m. Afterwards, the cavity -1 was heat treated at 1400^{o} C in a vacuum oven [9] for one hour with Titanium purification. The cavity was removed 80 μm of material from the inner RF surface and 30 μm from outer side by chemistry, followed by high pressure rinsing with ultra-pure water [9]. Then, the cavity was equipped with the rotating T-R mapping and tested in a vertical cryostat of T < 2.1 K.

A. Locating of Heated Areas and Intensity

We successfully locate the heated areas and their intensities associated with processing of cavity RF test. In the test the cavity -1 was initially stopped by heavy field emission at point A of 11.2 MV/m with a Q, 8.5 x 10^{8}. The T-map

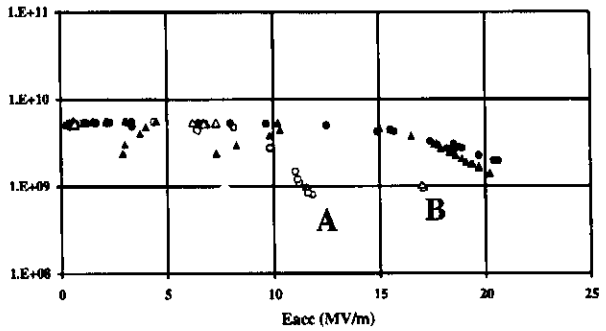

Figure 2: Overall RF performance of the TESLA cavity -1. Dots present first test, triangles present second test. (notice: the low power Q was corrected to about 1x10^{10} by later data)

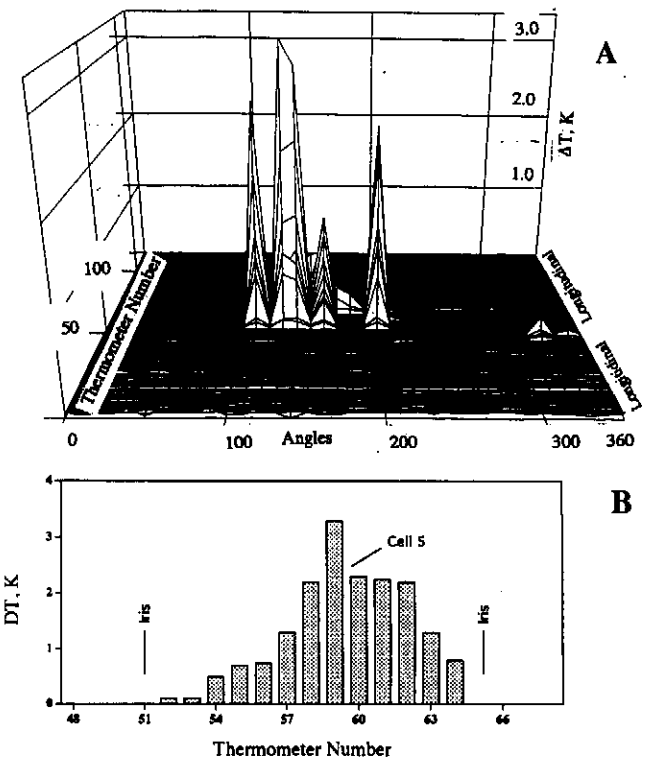

Figure 3: A, A temperature map taken at 11.2 MV/m for TESLA cavity -1. B,. Longitudinal ΔT plots, fixed at 140^{o}.

(Figure 3A-3B) indicate an important heated region delimited by 12 thermometers (#53 to #64) centred close to the equator of the 5th cell, between the 110^{o} to 200^{o} angles. out of this region the heating is very low. The ΔT value in this region is 100mK - 3.3K. The x-axial of figure 3 is the thermometer number from 0, close to the top iris of cell-1, to 116, close to the bottom iris of cell-9. The y-axial represents the angular location on the cavity surface. The high pulse RF power processing (HPP, up to Eacc=30 MV/m) [10] was introduced to the cavity and successfully eliminated the field emitters. Another T-map also witnessed the FE elimination. The shape of Q vs. E plots, map after HPP and FE electron tranjectories indicate that a serious defect heating in the area is excluded. After HPP, the cavity finally reached 20 MV/m in cw mode.

The cavity was stayed in the cryostat and naturally warmed up to about 200 K during the New-Year-Eve/95, and then cooled down and tested again. Strong field emission in the cavity was activated about 17 MV/m (point B). The hot spots are located in different angular position from the previous one in figure 3. The cavity reached 20 MV/m again (Q recovered also) only with a low RF power process. Similar phenomena was observed and explained in [11].

B. Analysis of Thermal Performance

The experimental data obtained with the T-R mapping is consistent with the thermal analysis if we consider the following assumptions: high efficiency of thermometer at high heat flux, heat transfer governed by Kapitza regime, and electron trajectories impacts over a large area.

The magnetic field heating at equators of the 5th cell, for Eacc=11.2 MV/m and Rs=30 nΩ, gives only ΔT=5 mK. From the RF measurement, we can estimate the total dissipated power in the cavity and distinguish the two main contributions: (1) dissipated power in the cavity wall due to magnetic losses: Prf=13 W, covering entire 9 cells, and (2) the power related to the electron FE: Pelec=173 W, focusing on local region.

The very high value ΔT measured in this region (100mK-3.3K) can only be explained by assuming that the efficiency of a scanning thermometer increases strongly with the heat flux density at the interface of cavity wall and HeII. This tendency has been observed in several thermometer calibration. We can estimated a heat flux density of 5 W/cm^2 in the region ΔT=3K based on experimental values of Kapitza conductance for Nb. Such a high heat flux density is slightly less than the critical heat flux densities reported in experiments with metallic flat heaters in HeII [12], So it is believed that the heat transfer is in the regime governed by Kapitza conductance. The integration of the product of Kapitza conductance and ΔT over the heated region leads to a total heat power going to He bath: Q~100 W. This value is consistent with the RF measurements of the experiment.

C. Identifying of FE Origins

Locating origins of FE and TB is very important to understand the influence of various cavity processing and also to a guided reparation of defected cavities. The measured hot spots directly indicate the location of a defect in case of TB. However, the measured hot spots only indicate the landing of impacting FE electrons, but not the emitter.

The simulation of FE electron trajectories demonstrate the following interesting results: FE electrons from an emitter can mpact over a very large area, the shape of trajectories are sensitive to emitter location (So), and an emitter responsible

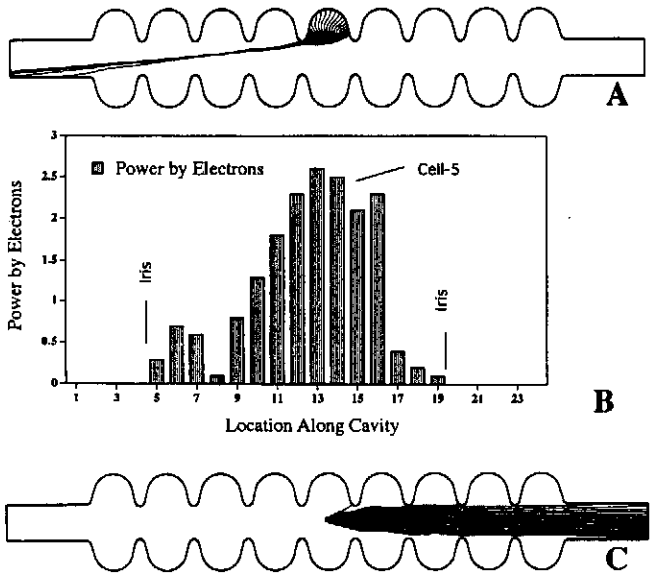

Figure 4: (A) FE electron trajectories of a emitter located at So=8 cm. (B) Power distribution contributed by impacting FE electrons from So=8 cm. (C) Electron trajectories, So=9 cm.

for the heating shown in figure 3 is successfully identified.

Since electron trajectories, impacting electron energy and power deposition distribution (dP/ds vs. s) are controlled by the Eacc and So, a series of simulations are performed by changing So at Eacc=11.2 MV/m, assume β=200, Se (emitter area) = 1x10^{-13}m^2. It is found that an emitter located at So=8 cm (at the iris area in a curvilinear co-ordination) has electron trajectories shown in figure 4A. Its power distribution (dP/ds vs. S) in figure 4B seems to be closed to the shape of the measured temperature distribution. It is indicated that heated area at equator (usually by defects) can also be caused by FE. The β and Se (emitter area) of the candidate emitter were adjusted to fit with the thermal analysis and RF experimental data. For instance, at Eacc=11.2 MV/m, if Se=1x10^{-13} m^2, β = 400, the total mean power landed over RF period is 10W.

The FE electron trajectories are very sensitive to the emitter location in the cavity. For example, if an emitter locates at So=9 cm, FE electrons are driven out of the initial cell and rush to the cut-off tube of the cavity (Figure 4C).

IV. FUTURE DEVELOPMENT

The improvement of the mechanical system and cabling of the mapping is scheduled in the May of 95. The computer data acquisition for photodiodes will also be commissioned at next test.

V. ACKNOWLEDGEMENT

We sincerely thank P. Kneisel (CEBAF), W. Weingarten (CERN), H. Padamsee, J. Graber, W. Hartung (Cornell), M. Champion (Fermilab), C. Pagani (INFN), B. Bonin (Saclay) and G. Wueller, R. Roeth (Wuppertal) for many fresh discussions and hints. Sincere thanks are also presented to our DESY colleagues in the cryogenic group, vacuum group, mechanical group, MHF group for their support.

VI. REFERENCES

1. Q. S. Shu et.al., TU-A3-6, CEC/ICMC Conf., Ohio, 1995.
2. T. Junquera et. al. TTP 14, this Conf., PAC/95.
3. D. Proch: Proc. - 5th workshop on RFS, DESY, 1991.
   R. Sundelin: Proc. - 6th workshop on RFS, CEBAF, 1993
4. H. Padamsee, Applied Supercond. Conf., Boston, 1994.
5. Ph. Bernard et. al, Nucl Inst & Met in Phys Res vol 190
   Ph. Bernard et. al. & S. Buhler et. al, the 5th (and 6th) workshop on RFS, DESY 1991 (and CEBAF, 1993).
6. Q.S. Shu et..al., IEEE transaction, Vol. 27, No. 2, 1991.
   Q.S. Shu et.al., Nucl Inst & Met in Phys Res A278. 1989.
   J. Knobloch, et. al., SRF 94-0419-03, Cornell Univ., 1994
7. B. Bonin et. al., Proc. of 6th workshop on RFS, 1993.
   M. Fouaidy et al Proc 5th workshop on RFS, DESY,1991.
8. R. Roth and G. Muller et. al., Proc. of the 5th (and 6th) workshop on RFS, DESY 1991 (and CEBAF, 1993).
9. A. Matheisen, D. Trines, TESLA Meeting, 1994.
10. J. Graber et. al., Nucl Inst & Met in Phy Res A278. 1989.
11. Q. S. Shu et. al., IEEE transaction, Vol. 25, No. 2, 1989.
12. A. Kashani, S. W. Van Sciver, Cryogenics 25, 1985.

SURFACE SCANNING THERMOMETERS FOR DIAGNOSING THE TESLA SRF CAVITIES

T. Junquera, A. Caruette, M. Fouaidy, IPN (CNRS - IN2P3) 91406 ORSAY cedex, France
Q.S. Shu, DESY, 2000 HAMBURG 52, Germany

ABSTRACT

In order to investigate the field emission and the thermal breakdown of 9-cell TESLA SRF cavities, 150 specially developed surface scanning thermometers have been built. The description of the thermometers and their calibration in superfluid helium are presented. A special test chamber equipped with a heated niobium plate is used to study the thermometer thermal response versus the heater power at different bath temperature. The comparison of thermometer response with numerical simulations results and experimental data obtained with reference thermometers mounted on the Nb plate using a thermal bonding agent, allows to get an estimation of the measurement efficiency of scanning thermometers. Experimental data obtained with cavities are analysed with the help of the calibration results and numerical simulations.

INTRODUCTION

The development of He II surface thermometers for diagnosing and studying the thermal effects in supercoducting RF cavities has been a major activity of the Orsay Group during the recent past years. Several papers describe the different types of thermometers and the main experimental features : fixed thermometers for studies of the anomalous heating of samples mounted on special cavities [1], scanning thermometers for monocell cavities [2] and special vacuum thermometers for Kapitza conductance measurements [3].

In this paper we present the first results of a new development in collaboration with the DESY laboratory, for constructing a diagnostic system for the 9-cell TESLA cavities. As compared to the older devices, a large number of thermometers (> 100) are mounted around the cavity which raises different mechanical and cabling problems. The complete description and the first results are given in an another paper at this conference [5]. In this paper we focuse on the calibration of the thermometers and the thermal analysis of the first temperature mapping results obtained.

DESCRIPTION

The surface thermometer design [Fig. 1] is very close to the model developed earlier for the CERN group [2]. The sensitive part is an Allen-Bradley carbon resistor (100 Ohm, 1/8 W) housed in a silver block with a sensor tip of 1 mm diameter for the thermal contact to the external surface of the cavity. This housing is thermally insulated against the surrounding He II by an epoxy envelope (Stycast) moulded around the silver block and into a bronze piece which allows the sensor mounting on the rotating thermometric arm. The thermometers tip must present a good contact with the cavity wall when scanning : two springs located inside two holes in the body of the rotating arm are used for this purpose, the contact pressure control and adjustement is allowed by means of two screws. Each thermometer has two independent manganin wires thermally anchored to the silver block with ~ 15 cm free length for connecting to each cell board (14 thermometers). At the level of the boards the connectors ensure the cabling dispatching inside the cryostat allowing the motion of the rotating arm.

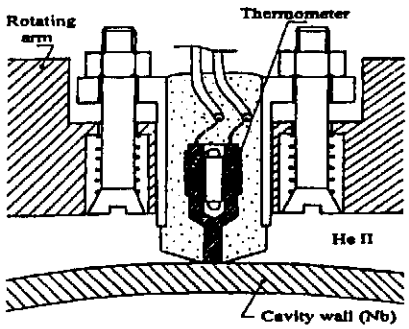

Fig. 1 : Cross section of a HeII surface thermometer

CALIBRATION

Superfluid helium

A representative batch (32) of the 150 thermometers fabricated for this device were tested using a special calibration chamber [1] allowing the mounting of 16 thermometers at every test. In principle all thermomters are located in a region subjected to the same heat flux density. In this experiment the thermometers tip were glued to the Nb heated plate by means of a good thermal bonding agent (Apiezon N Grease) in order to verify the fabrication process. The two thermometers batches (2 x 16) give a mean thermal response $<\Delta T>_1 = 8.0$ mK and $<\Delta T>_2 = 8.8$ mK respectively for a total heater power of 195 mW at $T_{bath} = 1.8$ K. Numerical simulation of the plate heater assembly for the same experimental conditions gives $\Delta T = 56$ mK. This calculation was performed in order to evaluate the thermometer efficiency η defined as the ratio of the experimental thermal response ΔT_{exp} to the simulated temperature jump ΔT_{sim} at the Nb - He II interface. In this case we obtained $\eta = 0.14$.

A complementary test was performed by mounting the thermometers in the real operating conditions of the scanning device, (e.g. without any bonding agent between the

thermometer tip and the Nb wall). The results for a batch of 13 thermometers is presented in Fig. 2 at two different heater powers of 1.86 W and 2.8 W. A first group of thermometers was mounted with a contact pressure of ~ 10 bars (spring load of 80 gr) giving $\langle\Delta T\rangle_{1.86}$ = 2.1 mK, a second group was monted with a pressure of ~ 62 bars (spring load of 500 gr) giving $\langle\Delta T\rangle_{1.86}$ = 6.4 mK. A third group of fixed thermometers (e.g. glued with grease, not displayed) gives $\langle\Delta T\rangle_{1.86}$ = 92 mK. At a higher power (2.8 W) the measurements were $\langle\Delta T\rangle_{2.8}$ = 6.3 mK (at a pressure of 10 bars) and $\langle\Delta T\rangle_{2.8}$ = 16 mK (at a pressure of 62 bars). All these results clearly show an important decrease of the measurement efficiency when no bonding agent is used : η is now close to 0.01. Notice that in this case, the efficiency is heater power dependant.

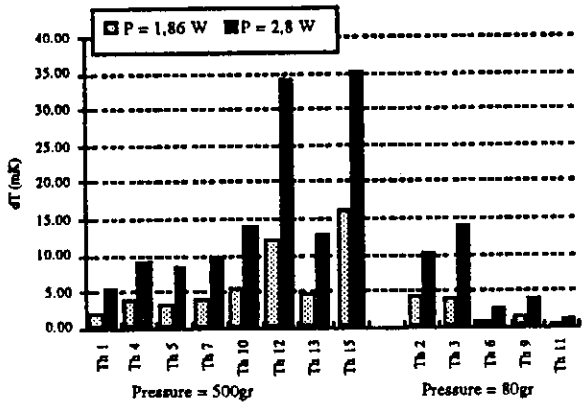

Fig. 2 : Thermal response at T_{bath} = 1.8 K (without contact grease)

Subcooled helium I

The subcooled helium bath obtained for temperature over the λ point (T>2.2K) and a pressure of 1 bar gives the possibility to study heat losses in the cavity wall in a far less constrained mode than in HeII. In this case the heat transfer mechanism is dominated by free convection cooling (laminar or turbulent) which induces the formation of a thick superheated helium boundary layer, the temperature is now quite easy to measure without taking many precautions in the mounting conditions of the thermometers. The calibration was made with the same thermometer batch and the same chamber. The results are displayed in Fig. 3. The same three groups of thermometers were tested giving respectively $\langle\Delta T\rangle_{80g}$ = 572 mK, $\langle\Delta T\rangle_{500g}$ = 651 mK and $\langle\Delta T\rangle_{fixed}$ = 537 mK for a total power of 146 mW at 2.5 K. These values show clearly a rather insensitivity to the mounting conditions and a much reduced dispersion in each group as compared to superfluid helium results. The agreement with a previous published equivalent thermal resistance [4] in subcooled helium at 2.5 K is quite good : the mean measured value is R_{th} ~ 30 K/W/cm^2 which is consistent with the calculated value of 65 K/W/cm^2 for the same heater [4] power. This agreement seems to be quite good considering all the hypothesis and simplifications adopted to calculate this thermal resistance in a free convection bath with turbulent flow using dimensional analysis. Anyway and as expected, the comparison with superfluid helium results in terms of thermal boundary resistance (e.g. R_{th} ~ 2K/W/cm^2, Kapitza resistance at 1.8K) shows up the benefit of operating in subcooled normal helium. However, the price to be paid is a reduced spatial resolution and a reduced operating accelereting field due to the global cavity heating.

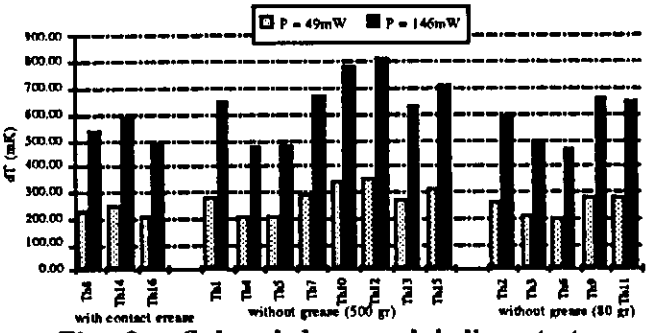

Fig. 3 : Subcooled normal helium test 2.5 K < T_{bath} < 3 K

EXPERIMENTAL RESULTS

The first experimental results using a completely equipped rotating arm (116 thermometers) have been obtained with a prototype TESLA cavity (1.3 GHz, 9 cells) [5]. This cavity, after a heat treatment at 1400 °C in a vacuum furnace, was tested in a vertical cryostat at the DESY TTF facility. During the experiment, high power processing (HPP) was performed which leads to an important improvement of the cavity performances : E_{acc} = 20 MV/m at Q_o = 2 x 10^9 (Q_o at low field $\geq$ 10^{10}). Several T-maps were recorded during the test in superfluid helium bath (before and after HPP) and in a subcooled helium bath (after HPP).

a) Superfluid He II bath

During the first run, the cavity reach a maximum accelerating field (E_{acc}) of 11.2 MV/m limited by a very heavy field emission. The Q_o decreased from $\geq$ 10^{10} at low field to 8 x 10^8 at the maximum field. A first T-map was recorded at this value exhibiting very high ΔT in the 5th cell. The heated region was very extended : it concerns 12 thermometers of the 5th cell (Fig. 4) and presents several maximums at different angles between 100 ° and 200 ° (Fig. 5). Very high ΔT were measured (1K - 3.3 K) in this cell.

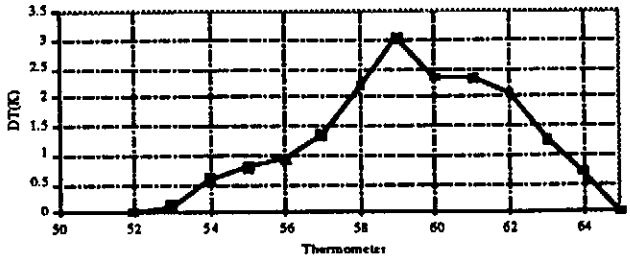

Fig. 4 : ΔT (5th cell thermometers) at 130° azimuthal angle

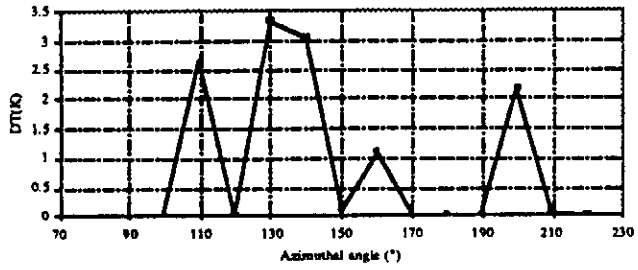

Fig.5 : ΔT (thermometer #59) vs. azimuthal angle

The first question raised by these results is if we may trust the measurements. In order to explain that a very high measurement efficiency of the thermometers must be considered. During the thermometer calibration the measurement efficiency has exhibited a strong dependance on the heat power level : the efficiency is multiplied by 2 when the power is increased from 1 to 3 W. This is completely different from the behaviour of fixed thermometer using a thermal bonding agent (Apiezon grease) which exhibits a ΔT linearly proportional to the heater power. Evidence of high ΔT measured in monocell cavities with scanning thermometers has been observed many times. Values of ΔT in the range of 100 mK to 200 mK have been measured in Nb/copper cavities at CERN [2] with largely lower RF power levels (~ 2 to 10 W).

If we admit a very good efficiency at the high heat flux density encountered in this cavity, another questionable point remains : are such high heat flux density levels compatible with the critical heat flux in He II ? Some references on this subject confirms that metallic heated plates in He II exhibit very high ΔT (5 to 6 K) in the Kapitza regime before reaching the critical flux inducing the transition to film boiling [6].

Extensive calculations of electrons trajectories at 11.2 MV/m shows that emission sites located in the proximity of the iris of the 5th cell could explain such impacts in the equator region of this cell. The azimuthal spreading of the heated area is more difficult to understand. Model calculations simulating a unique emitter site provocating a rather thin electron impact along the azimuthal can explain a smaller angular spreading in the cold face of the cavity. To explain the ΔT shapes observed, a first hypothesis of separated sites located in the same cell at different angles along the iris must be admited. From the point of view of the total power involved in this experiment we have performed the integration of the heat power density over the heated region :

$$Q = \int_s qds \approx S_{th} \sum_n h_k \Delta T_n$$

where S_{th} is an estimation of the equivalent heated surface measured by one thermometer which has been arbitrarily taken equal to the product of the distance between two thermometers and length corresponding to a scanning angle of 10°. h_K is the Kapitza conductance at the measured point

$$h_k = H_K.f(\Delta T) = h_o\, T_{bath}^{n}.\, f\,(\Delta T/T_{bath})$$

$$H_k = 0.017\ T^{3.62}\ W/cm^2K \quad [7].$$

This integration gives Q ~ 100 W which seems to agree quite well with the RF power measurements. The power attributed to the electrons is easily deducted from the ΔQ_0 at E_{acc} = 11.2 MV/m ($\Delta Q_0 = 10^{10} - 8 \times 10^8$). A simple calculation gives $P_{electron}$ ~ 170 W. So, we obtain values which are of the same order of magnitude : the discrepency could be attributed to HK variations from Nb sample to another and to η which is not exactly 1. This good agreement could add some confidence to the recorded ΔT.This strong field emission was efficiently treated by HPP technique in the same experiment and a very good Eacc value was reached (20 V/m). A T-map taken at 17.7 MV/m shows that the heating observed in the 5th cell has disappeared and that some lower heating is now measured in the cells #5 and #7 reaching some peaks of ΔT ~50mK at angles of 100° and 280°.

b) Subcooled helium bath

Several T-maps were performed in a subcooled HeI bath at bath temperature in the range 2.3 - 2.5K with E_{acc} ~18 MV/m. All the maps shows a global heating (ΔT) ~ 400 mK of all the cells and some scattered hot points in cells # 5 and # 7. It is interesting to compare this measured values with the results obtained during the calibration : the surface resistance ($R_{BCS} + R_{residual}$) at a wall temperature of 3 K is estimated to be R_S = 150 nΩ. In the equator region of the cells the surface magnetic field corresponding to Eacc = 18 MV/m can be computed : Hs ≅ 6.10^4 A/m. Then the heat flux density in this area is calculated : $q_S = \frac{1}{2} R_S H_S^2 \approx 27 mW/cm^2$.

Considering the equivalent thermal resistance measured during the calibration tests in subcooled helium (R_{th} ~ 30 K/W/cm²) we can estimate the resulting heating : ΔT ~ 800 mK. This is a good agreement with the measured values when we take into account all the simplifications adopted to perform this estimation the thermal resistance depends on the heated surface orientation with respect to the vertical (buoyancy force).

REFERENCES

[1] M. Fouaidy, T. Junquera, A. Caruette, Proc. 5th Workshop on RF Superconductivity Hamburg (1991) p. 547,

[2] Ph. Bernard, D. Bloess, E. Chiaveri, C. Hauviller, T. Schiller, M. Tauffer, W. Weingarten, P. Bosland, A. Caruette, M. Fouaidy; T. Junquera, Proc. 6th Workshop on RF Superconductivity (Newport News, Oct. 1993) CEBAF report, p. 739,

[3] S. Bühler, A. Caruette, M. Fouaidy, T. Junquera, Proc. 6th Workshop on RF Superconductivity (Newport News, Oct. 1993) CEBAF report, p. 1002,

[4] R. Romijn, W. Weingarten, IEEE Trans. on Magnetics, Mag 19 (1983), p. 1318,

[5] Q.S. Shu, G. Deppe, W. Moller, M. Pekeler, D. Proch, D. Renken, P. Stein, C. Stolzenburg, T. Junquera, M. Fouaidy, A. Caruette, (this conference),

[6] A.Kashani, SW. Van Sciver, Cryogenics 25 (1985) p.238

[7] K. Mittag, Cryogenics 13 (1973), p. 94.

Options and Trade-Offs in Linear Collider Design

J. Rossbach
Deutsches Elektronen-Synchrotron, D-22603 Hamburg, Germany

Abstract
Four markedly different concepts of linear colliders are presently under investigation. They may be characterised by the keywords 'X-band, S-band, two-beam, and superconducting'. Both the essential differences and the common problems are pointed out in this paper. As a basis of discussion, parameter sets of six collider study groups working on JLC/KEK, NLC/SLAC, VLEPP/BINP, CLIC/CERN, SBLC/DESY, and TESLA will be used.

1. INTRODUCTION

This paper deals with the concepts of linear colliders (LC) in the 300 GeV to 1 TeV center-of-mass energy range as they are presently under discussion. They are based on four distinct approaches: the conventional S-band (3 GHz) approach, the X-band (11 to 14 GHz) approach, the two-beam accelerator approach, and the superconducting L-band approach. Except for the X-band approach, each of them is represented by a single linear collider study group. This does not mean of course, that important R&D work is not done elsewhere. These groups are TESLA as an international effort for the superconducting cavity concept, CLIC(CERN) for the two-beam approach, and SBLC(DESY) putting forward the S-band based design. Use of X-band cavities is proposed by three studies named NLC(SLAC), VLEPP(BINP), and JLC(KEK). Note that JLC also considers an S-band and a C-band version of their collider. The main parameters of these six linear collider studies are compiled in table 1.

The information on the status of the respective activities lies beyond the scope of this paper. It may be useful, nevertheless, to point out some problems which are common to all of the designs, and to compare the different ways proposed to solve them. This comparison is all the more possible since an international committee has been founded to work out a detailed comparison of the various linear collider schemes [1]. The emphasis in the following discussion will be on the optimisation of beam power and vertical beam size. The reason is that, in order to get the desired luminosity, one unavoidably needs very high average beam power, so that power efficiency becomes an essential parameter. Depending on what one feels to be the optimum assumption on these parameters, the choice of rf frequency will have to be different. In addition, since the achievable gradient is connected with the rf frequency, the energy upgrade scenario maybe considered an issue, especially if the total length of the collider will be strictly limited.

2. HOW TO GET THE LUMINOSITY

Due to the small cross-sections of the processes of interest, high energy electron-positron linear colliders need a luminosity L of the order of 10^{33} to 10^{34} cm^{-2} s^{-1}. It is instructive to realize that L can be represented by

$$L = \frac{f_{rep} n N^2}{4\pi \sigma_x^* \sigma_y^*} = \frac{P_b \cdot N}{4\pi E \sigma_x^* \sigma_y^*} \qquad (1)$$

For the meaning of symbols, see Table 1.
Apparently, there are only three free parameters at a given collision energy: P_b, N, and the beam size at the interaction point (IP) $\sigma^*_x \cdot \sigma^*_y$.
The bunch population N cannot be increased beyond the 10^{11} level because of wakefields acting on the tail of each bunch and because of excessive beam disruption caused by the interaction with the large Coulomb-field of the opposing bunch. The vertical disruption parameter D_y scales as

$$D_y = \frac{N \cdot \sigma_s}{\sigma_y^* \left(\sigma_x^* + \sigma_y^*\right)} \qquad (2)$$

Thus, one could - at least in principle - compensate the effect of a large N on beam-beam interaction by a large beam size and a short bunch length. This would be favourable only if one operates at a small rf frequency, because only then are both the longitudinal and transverse wakefields tolerable even at large N. In fact, as is seen from Table 1, all high f_{rf} designs except VLEPP use bunch population numbers below 10^{10}. With VLEPP, one intentionally puts up with both wakefields and a large disruption factor $D_y = 215$, because the BNS damping with 'autophasing' [4] and the 'travelling focus' [5] techniques are considered powerful enough to manage the respective effects. Also, VLEPP considers the γ-γ collision option in the first place, where disruption and beamstrahlung is not an issue. In this scheme[6], two electron beams are collided with very intense laser beams just before interaction thus transferring most of the electron momentum to Compton gammas. These are collided then instead of the electron beams, which are separated by an external magnetic field before collision. Discussion of the challenge of generating the required intense laser beams is beyond the scope of this paper.
A further restriction on parameters is due to the intense synchrotron radiation called beamstrahlung which accompanies the beam disruption. It is characterized by the parameter Υ which scales as $\Upsilon \propto D_y \sigma^*_y / \sigma^2_s$. This limits the possible reduction of σ_s, besides technical

aspects, in the bunch compressor. Since, for a flat beam, Υ depends only on σ_x and not on σ_y, β^*_x is decreased so far that the rms collision energy is smeared by beamstrahlung by just a tolerable amount (say $\delta p/p$ a few %, see Table 1). Afterwards, β^*_y is decreased as far as possible. The limit is given by the bunch length, because a beta function smaller than the bunch length does not increase luminosity (hour-glass effect). In fact, as seen from Table 1, all LC schemes use β^*_y close to σ_s. Another limit on β^*_y that comes into play at very high beam energies is due to the synchrotron

General parameters	**Units**	**Symbol**	**TESLA**	**SBLC**	**JLC(X)**	**NLC**	**VLEPP**	**CLIC**
Initial c.m. energy	GeV	E	500	500	500	500	500	500
Luminosity	$10^{33}\,cm^{-2}\,s^{-1}$		3.6	2.2	5.1	5.3	12	0.7-3.4
total two-linac length	km	l_{tot}	31	36	15	20	10	12.4
rf frequency of main linac	GHz	f_{rf}	1.3	3	11.4	11.4	14	30
Linac repetition rate	Hz	f_{rep}	5	50	150	180	300	2530-1210
Number of particles/bunch	10^{10}	N	3.6	2.9	0.63	0.65	20	0.8
Number of bunches/pulse		n	1130	125	85	90	1	1-10
Damping ring energy	GeV	E_d	4	3.15	1.98	2	3	2.15
Main Linac			**TESLA**	**SBLC**	**JLC**	**NLC**	**VLEPP**	**CLIC**
Avg. beam power/beam	MW	P_b	8.2	7.26	3.2	4.2	2.4	0.8-3.9
Bunch spacing	ns	τ_b	708	16	1.4	1.4	--	0.66
Bunch train length	ns	τ_p	$8{\cdot}10^5$	1984	118	125	--	0 - 6
Unloaded Gradient	MV/m	g_0	25	21	73	50	100	80
Loaded Gradient	MV/m	g_l	25	17	53	38	91	78-73
Length of sections	m	l_s	1.04	6	1.3	1.8	1.0	0.27
a/λ range		a/λ	0.30	0.16-0.11	0.20-0.14	0.22-0.15	0.14	0.2
Section filling time	ns	τ_f	$5{\cdot}10^5$	790	110	100	110	11.6
rf pulse length at cavity	μs	τ_p	1315	2.8	0.23	.24	0.11	0.0116
Pulse compression ratio			--	--	2	3.6	4.5	--
Number of klystrons		n_k	604	2517	3400	3940	1300	'2'
Peak rf power from klystron	MW	P_k	7.1	150	135	50	150	700
Avg. total AC power for rf generation (both linacs)	MW	P_{tot}	88*	142	114	102	57	100*)**
Beam parameters at interaction			**TESLA**	**SBLC**	**JLC**	**NLC**	**VLEPP**	**CLIC**
Horizontal invariant emittance	$10^{-8}\pi$m	ε^n_x	1400	1000	330	500	2000	300
Vertical inv. emittance	$10^{-8}\pi$m	ε^n_y	25	50	4.8	5	7.5	15
Horizontal β at IP	mm	β^*_x	25	22	10	10	100	10
Vertical β at IP	mm	β^*_y	0.7	0.8	0.1	0.1	0.1	0.18
rms beam width at IP	nm	σ^*_x	845	670	260	320	2000	247
rms beam height at IP	nm	σ^*_y	19	28	3	3.2	4	7.4
Bunch length	mm	σ_s	0.5	0.5	0.09	0.1	0.75	0.2
eff.beamstrahlung parameter		Υ_{eff}	0.03	0.04	0.12	0.09	0.07	0.07
rms $\delta p/p$ from beamstrahlg.	%	$\sigma_{\delta p/p}$	2.9	2.8	3.2	2.4	13.3	3.5
vertical disruption		D_y	11	8.5	8.2	7.3	215	9.7
Crossing angle	mrad		0	3	6.1	20	0	1

Table 1: Main parameters of linear collider studies at a c.m. energy of 500 GeV [1-3]. For the JLC, there is also a C-band (5.7 Ghz) and an S-band (2.8 GHz) version under consideration. The choice will depend on the maximum beam energy desired in the final stage of upgrade, given a fixed total length of the tunnel. Also, a change of frequency during a later upgrade stage is possible. The luminosity is calculated in accordance to eq. (1). No enhancement due to the pinch effect has been taken into account, and no loss due to the crossing angle. For flat beams, the combination of both effects yields a luminosity enhancement factor of typically 1.5.

)For TESLA and for CLIC (drive beam) the cryogenic power is included.* *)For the single bunch version.*

radiation in the final focus quadrupole magnets [7]. The increasing difficulty with chromatic errors when reducing β^*_y is less a problem since the development of a broad-band final focus optics [8].

If one combines all these scalings and restrictions with eq. (1), it now reads

$$L = A\frac{P_b}{\gamma}\cdot\sqrt{\frac{\langle\delta p/p\rangle}{\varepsilon_y^n}} \quad (3)$$

with $A \approx 10^{36}\,cm^{-2}\,s^{-1}$, if P_b is measured in MW and ε^n_y in rad·m. As $\delta p/p$ is limited by the experiment's requirements, there are only two free parameters left in the luminosity formular: the average beam power P_b and the normalized vertical emittance ε^n_y.

In principle, ε^n_y is determined in the damping ring by misalignment tolerances or, ultimately, by intra-beam scattering. In practice, however, it could be in vain to achieve, with big technical effort, a very small ε^n_y at the exit of the damping ring because it will eventually grow in the linac due to wakefield effects if its value was chosen unreasonably small.

One concludes that, with reasonable numbers on ε^n_y and $\delta p/p$, Megawatts of average beam power are needed to keep L above the $10^{33}\,cm^{-2}\,s^{-1}$ level. Thus, the efficiency of beam power generation from wall plug power becomes an important issue. Facing the fact that there is surely an upper limit of tolerable power consumption, it is a non-trivial statement that the parameter optimization and even the choice of fundamental technical parameters like the rf frequency could have a very much different outcome if the required luminosity would be smaller by say a factor of ten.

2. THE CHALLENGE OF HIGH BEAM POWER

Realization of high beam power involves two problems:

1.
2. One has to generate a large amount of rf power with high power efficiency. Then, again with high efficiency, this rf power must be transmitted to the electron/positron beam.
3. When the beam extracts this large electric power from the accelerating cavities, there will be longitudinal and transverse field distortions induced, called wakefields. They will, in turn, act on the tail of each bunch and may still be present to some extent when the next bunch arrives, thereby causing both single bunch beam break-up and multi-bunch instabilities.

The design net efficiency η_{rf} for production of rf power for the various schemes is listed in Table 2. It is seen that all of these values lie close by in the 25 - 40 % range. It should be noted, however, that the respective values are much closer to the present-day state of the art for the lower rf frequency schemes TESLA and SBLC than for the high frequency ones. The machines differ over a wider range concerning the efficiency η_{AC} of converting ac power to beam power, see Table 2. The reason is, that the efficiency of rf power transmission to the beam is best if the rf pulse is much longer than the cavity filling time, i.e. acceleration of a long bunch train is favoured. In this case, power transmission is in a quasi steady-state. While now most collider schemes foresee the multi-bunch mode, it leads to severe difficulties with CLIC. One concludes from all that, that it is harder for high frequency machines to achieve high beam power.

	TESLA	SBLC	JLC	NLC	VLEPP	CLIC
η_{rf}/%	35	36	30	30	39	26
η_{AC}/%	19	10	5.6	8.2	8.4	1.6

Table 2: Net rf system efficiency for production of rf power [1]. For TESLA and for CLIC (drive beam) the cryogenic power is included. For CLIC, the single bunch version is meant.

With respect to wakefields, the difference is much bigger. The short-range longitudinal wake field causes an energy spread within the bunch, which is undesirable due to the chromatic effects of focusing along the linac. For scaled accelerating structures this spread is proportional to the square of the frequency f_{rf}. This is plausible if one considers the fact that for fixed gradient the stored energy per unit length in an accelerating cavity is inversely proportional to f_{rf}^2. The easiest cure foreseen for this higher order mode excitation is to increase the aperture-to-wavelength ratio a/λ when increasing the rf frequency. Unfortunately, this measure also injures the shunt impedance, i.e. one needs more power to generate the accelerating field (a superconducting linac like TESLA does not have this problem, so it can use a large a/λ value, anyway). Thus one cannot go too far in that direction. What also helps is just to increase the accelerating gradient g_0, because the stored energy scales with g_0^2 while the extracted power only scales linearly with g_0. This is of cause the most favourable way, but it is limited by efficiency considerations. Thus, one has to conclude that low frequencies are preferable also with respect to longitudinal wakefields [9].

The frequency scaling behaviour of transverse wakefields is even more pronounced as they increase with the third power of f_{rf} and linearly with the bunch population N. This is illustrated in Figure 1, where $N\cdot f_{rf}^3$ is plotted in arbitrary units versus N for those frequencies which are considered by the respective linear collider schemes. Note that a logarithmic scale is used. Although TESLA and

SBLC use N considerably larger than the X-band designs and CLIC do (again except for VLEPP), the transverse wakefields would be still smaller by up to two orders of magnitude if the other parameters were unchanged. However, $\vec{E}_\perp$ scales with $\sigma_z^{-1/2}$, and the beams suffer on a

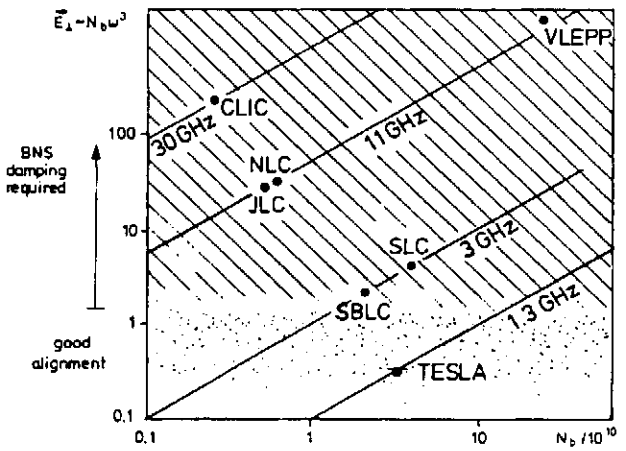

Figure 1: Transverse wakefield $\vec{E}_\perp$ as a function of bunch population N for scaled structures with frequencies as considered by the respective linear collider schemes. The hatched area indicates the region where BNS damping techniques will be indispensable, while for the dotted region good alignment of quadrupole lenses and cavities (in the 10 to 500 μm range) may be sufficient.

longer way if the accelerating gradient is smaller. Also, the cavity shape and the average β function enter. If all these effects are taken into account, the relative transverse emittance growth scales roughly as [10]

$$\Delta\varepsilon/\varepsilon \propto [N^2 \sigma_z ((f_{rf}\,\lambda/a)^3/g_l)^2/\varepsilon]\,\beta\,\Delta y^2_{cav}$$

if cavities are misaligned by Δy_{cav}. Figure 2 illustrates, that the relative vertical emittance growth in fact differs by orders of magnitude between various machines if no counter-measures like BNS damping are taken. The hatched area in Figure 1 indicates the region where BNS damping will be indispensable.

Besides short range wakefields there are also long range effects that can lead to multi-bunch instabilities. These long-lasting distortions are driven by Higher Order Modes (HOM) which are excited by bunches in the front of the bunch train and act on subsequent bunches. A significant reduction of HOMs has been achieved with the development of the 'Choke Mode Cavity'[11], which allows the HOMs to propagate out of the cavity while only the accelerating mode is trapped. Recently a method has been proposed to damp HOMs by stainless steel coating the iris [12].

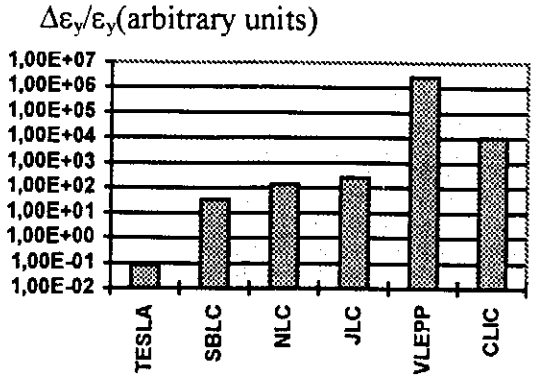

Figure 2: Relative vertical emittance growth (in arbitrary units) from transverse wakefields if cavities are misaligned by Δy_{cav} and if no BNS damping is applied.

To summarize this paragraph, it is seen that low frequency linacs can more easily achieve high beam power while still suffering much less from wakefields. In other words, in spite of higher beam power and significantly relaxed cavity alignment tolerances they can preserve smaller beam emittances. Additional advantages are

- only one stage of bunch length compressor is required
- in case of SBLC, the existing SLC in Stanford/USA, with all its experience, may be considered an existing 20 % prototype of an S-band collider.

There are, however, serious drawbacks if one concentrates on the technology for high beam power alone:

- For accelerating gradients above some 30 MV/m, the power efficiency of a normal conducting low frequency collider drops, because rf pulse compression is required (i.e. η_{rf} gets smaller and the bunch train will be shorter). Thus, an optimized high beam power collider will be very long. This might be, if not an economical, at least a political disadvantage.
- Concerning TESLA, considerable progress has been made with achieving the design accelerating field of 25 MV/m in 5-cell cavities [13], and recently in a TESLA Test Facility series production 9-cell cavity [14]. However, it remains still to be seen if even higher gradients (although not excluded from basic physics) can be supplied routinely in a long linac and if costs can be reduced sufficiently.
- It seems likely that dark currents are more serious at lower frequencies, since they have a higher probability to get trapped there.
- Multi-bunch operation is essential for high beam power operation, and it involves all the complications of multibunch-instabilities. Meanwhile no scheme except VLEPP (and maybe CLIC) is completely free of this complication, but one should be aware that it has ist roots in the requirements of high power efficiency.

3. SMALL VERTICAL EMITTANCE

The vertical beam size achieved with the Final Focus Test Beam installation at SLAC [15] was σ^*_y = 70 nm at ε^n_y = $200 \cdot 10^{-8}$ π rad·m and N = $0.65 \cdot 10^{10}$. Comparing with the respect values of the LC plans (see Table 1), one readily sees that all of them need 'small' vertical beam size at the IP. Some go, however, more than one order of magnitude below the present state of the art. Interestingly, this does not necessarily mean, that alignment tolerances in the respective damping rings are much different, because the TESLA and SBLC damping rings have to be much longer due to the longer bunch train, i.e. more focusing elements are involved.

Techniques beyond well-proven ways of alignment and orbit correction will be needed. As a means of improving the effective beam position monitor alignment, the 'beam based alignment' technique has been devised [16]. To improve cavity alignment, mechanical micro-movers, controlled by signals from HOM antennas, are under construction [17]. All beam-based correction techniques are applicable only for misalignments changing slowly compared to f_{rep}. In this respect, the low f_{rf} , low f_{rep} machines have clearly a disadvantage. On the other hand, especially TESLA can tolerate a much worse cavity misalignment (few tenths of a mm compared to less than 10 μm for X-band) and position monitor resolution because the wakefields are weak enough. Also, its large bunch spacing allows using the first bunch in a train to correct the subsequent ones.

Name	upgrade scenario	l_{tot} for 1 TeV c.m.
TESLA	double the length can still very much reduce ε^n_y	60 km
SBLC	rf pulse compression (reduces η_{AC})	30 km
JLC	start with S-band (?), upgrade with X-band	22 km
NLC	increase both length and gradient	20 km
VLEPP	double the length?	20 km?
CLIC	double the length	14 km

Table 3: Energy upgrade scenarios of LC schemes

4. UPGRADE POTENTIAL

The most essential upgrade of a 500 GeV c.m. linear collider will be a program to increase the collision energy. Table 3 illustrates the various energy upgrade scenarios proposed [1]. It is seen that most groups plan to increase the total length, not only the low f_{rf} schemes. Only the high f_{rf} machines, however, can stay within 20 km for a 1 TeV collider. Also, they have the potential to even further increase the gradient, at the expense though of further reducing η_{AC}. By learning from operational experience how to preserve extremely small ε^n_y, they might then still be able to provide the required luminosity. It is unclear yet if this is realistic and if saving total length pays off compared to the higher power efficiency of, say, a long TESLA collider.

5. CONCLUSION

It is the lesson from many theoretical as well as experimental studies performed over the last two decades, that a linear collider providing the required high luminosity can be built. It remains to be learned, however, from the various test facilities under construction now, what the most economical way and the most reliable technique will be.

REFERENCES

[1] G. Loew, T. Weiland (eds.): Linear Collider Technical Review Committee Report 1995, to be published (1995)

[2] R. Brinkmann: Low Frequency Linear Colliders, Proc. EPAC94, London (1994)

[3] W. Schnell: High Frequency Linear Colliders, Proc. EPAC94, London (1994)

[4] V. Balakin, A. Novokhatsky, V. Smirnov: Proc. 12th Int. Conf. on High Energy Accelerators, Batavia, Illinois (1983)

[5] V. Balakin: Proc. 1991 Linear Collider Workshop Protvino, Russia (1991)

[6] V. I. Telnov, Nucl. Instr. Meth. A 294, 72 (1990)

[7] K. Oide: Synchrotron-Radiation Limit on the Focusing of Electron Beams, Phys. Rev. Lett. 61, No. 15, (1988)

[8] R. Brinkmann: Optimisation of a Final Focus System for Large Momentum Bandwidth, DESY-M-90-14, (1990)

[9] G.-A. Voss: The case for the S-band Linear Collider, Proc. 1992 Lin. Acc. Conf., Ottawa, (1992)

[10] R. Brinkmann, private communication

[11] T. Shintake, et al.: High Power Test of HOM-Free Choke-Mode Damped Accelerating Structures, KEK Preprint 94-82, (1994) and Proc. 17th Int. Linac Conf. Tsukuba (1994)

[12] M. Dohlus, presented on the LC95 workshop, Tsukuba (1995); see also [17]

[13] C. Crawford, et. al.: High Gradients in Linear Collider Superconducting Accelerator Cavities by High Pulsed Power to Suppress Field Emission, Part. Accelerators, 49, 1-13 (1995)

[14] J. Graber: High Gradient Superconducting RF Systems, this conference

[15] V. Balakin, et.al.: Focusing of Submicron Beams for TeV-Scale e^+-e^- Linear Colliders, Phys. Rev. Lett. 74, No. 13 (1995)

[16]. T. O. Raubenheimer; SLAC-report 387 (1991)

[17] N. Holtkamp: The S-band Linear Collider Test Facility, this conference

ANALYSIS OF MULTIPACTING IN COAXIAL LINES

E. Somersalo, P. Ylä–Oijala, Rolf Nevanlinna Institute, University of Helsinki, PO Box 26, 00014 University of Helsinki, Finland
D. Proch, DESY, Notkestrasse 85, 2000 Hamburg 52, Germany

Abstract

Multipacting can cause breakdown in high power rf components like couplers, windows, etc. This phenomenon starts if certain resonant conditions for electron trajectories are fulfilled and if the impacted surface has a secondary yield larger than one. A general cure against multipacting is to avoid the resonant conditions. Therefore we investigated the dynamics of the electron trajectories in order to find rules for these resonances and thus suppress multipacting by appropriate design. We developed a new code which combines standard trajectory calculations with advanced searching and analyzing methods for multipacting resonances. As a first step, coaxial power lines are investigated. We characterize multipacting behavior in straight and tapered lines and give scaling laws with respect to dimension, frequency and impedance. The calculations are compared with experimental observations.

I. INTRODUCTION

This paper gives a brief description of a code developed for analyzing multipacting in rf cavities. The code consists of two main elements: The first step is to recognize those rf power levels in the given geometry that are able to multipact. The second step is to locate and identify the possible multipacting processes. The core of the code consists of standard trajectory calculations. The novel feature is a systematic application of ideas arising from the theory of dynamical systems.

II. THEORETICAL BACKGROUND

Physically, the multipacting process is described as follows. An electron is emitted from the surface of an rf cavity and driven by the field. When it impacts the cavity wall, it may release one or more electrons from the surface layer of the wall, the number of the secondary electrons depending on the impact energy and the wall material characteristics. These secondary electrons are again accelerated by the field, yielding new impacts and possibly new secondary electrons. In appropriate conditions, the number of electrons may increase exponentially, leading to remarkable power losses, gassing of the surface and heating of the walls.

The following is a brief summary of the mathematical description of the process, which constitutes the background of the programs used for analyzing the multipacting processes in rf cavities.

A. Dynamical system

Consider a void cavity Ω with a time harmonic rf field. Denoting by f the rf frequency, the electric and magnetic fields can be written as

$$\vec{E}(x,t) = \vec{E}(x)\sin 2\pi ft, \quad \vec{B}(x,t) = \vec{B}(x)\cos 2\pi ft,$$

where $\vec{E}(x)$ and $\vec{H}(x)$ are the spatial amplitudes of the fields. Let φ denote the phase angle of the field, $0° \le \varphi < 360°$. Consider an electron being emitted at a point x of the cavity wall $\partial\Omega$, the field phase at the time of emission being φ. Assuming that the rf field map in the cavity is known, it is a straightforward matter to compute the relativistic trajectory of the electron driven by the field. Denote by x' the point where the electron hits the cavity wall for the first time. If the phase of the field at the time of the impact is denoted by φ', we have a mapping

$$R : (x,\varphi) \mapsto (x',\varphi').$$

Using the notation $X = \partial\Omega \times [0°, 360°[$, the above mapping R defines a dynamical system in the phase space X: Each point $p = (x,\varphi) \in X$ generates a discrete trajectory $\{p, R(p), R^2(p), \ldots\}$. For each initial point $p \in X$, there are two possibilities: It may happen that after a finitely many impacts, the field phase is such that the electric field prevents the electron from escaping the wall. In this case, the discrete trajectory remains finite. The other possibility is that the discrete trajectory is infinite. The latter case is the geometric condition for the multipacting to occur.
Besides the geometry of the trajectories, the analysis needs to contain the secondary electron yield characteristic to the surface properties. Given an electron trajectory starting at a point p, the kinetic impact energy $E_{\mathrm{kin}}(p)$ can be computed. If the secondary electron yield of the cavity wall is denoted by δ, the number of secondary electrons due to one single electron starting at p is in the average given by $\alpha(p) = \delta(E_{\mathrm{kin}}(p))$. Considering the full discrete trajectory, the number of secondary electrons due to one single electron starting at p after n impacts is

$$\begin{aligned}\alpha_n(p) &= \alpha(p) + \alpha(p)\alpha(R(p)) + \ldots \\ &+ \alpha(p)\alpha(R(p))\ldots\alpha(R^n(p)).\end{aligned}$$

B. Distance function

A special case of the infinite trajectories that leads to resonant multipacting is when periodic trajectories appear. This corresponds to fixed points of the mapping, i.e.,

$$R(p) = p$$

for some $p \in X$, or more generally,

$$R^n(p) = p, \quad n = 1, 2, \ldots$$

Physically, this corresponds to a situation where an electron trajectory hits eventually the same wall point in the same field phase where it started. This condition is fulfilled in the earlier described multipacting phenomena, and it seems to be a potentially dangerous resonant condition in general. An effective way of searching for those points p in the phase space is to consider the distance function

$$d_n(p) = \sqrt{|x - x_n|^2 + \gamma |e^{i\varphi} - e^{i\varphi_n}|^2},$$

where $p = (x, \varphi)$ and $(x_n, \varphi_n) = R^n(p)$. Here, γ is a scaling constant. The distance function d_n tells how far away the trajectory is after n impacts from the initial point. If $d_n(p)$ is small for n large, the point p is likely to be prone to multipacting.

III. COMPUTATIONS

To obtain reliable results, the rf field maps have to be known rather accurately in the cavity. In straight coaxial lines discussed below, the field map is no problem since it is analytically known. In the other cases, one has to use a numerical scheme. We have developed a suitable numerical code for computing the fields in axisymmetric geometries. The code is based on boundary integral equations, with extra care being taken for the accuracy of the computations close to the walls.

The multipacting analysis was implemented along the following lines. Given a cavity Ω and the corresponding rf field map, we picked a large number of initial points p_j in the phase space X associated to the boundary and for each point p_j computed the discrete trajectory $\{p_j, R(p_j), R^2(p_j), \ldots\}$. After a fixed number n of iterations of the map R, we counted those electron trajectories that were still able to multipact. This number, denoted by c_n, was computed repeatedly for different incident rf field powers. If at a given incident power no multipacting can occur and the discrete trajectories $\{p_j, R(p_j), R^2(p_j), \ldots\}$ are short, the number c_n is very small. The multipacting powers outstand clearly as having an elevated c_n value.

Having the counter function c_n computed, we plotted the distance function $d_n(p_j)$ for those rf power values where c_n was large. The minima of d_n give the initial points of those trajectories that correspond to multipacting. A recomputation of the trajectories starting at the minima of d_n can be used to analyze the nature of the multipacting process. The important questions are the order of the multipacting (number of rf cycles per wall impact), whether it is a one–point or multi–point multipacting and whether it is due mostly to the magnetic or electric field.

Finally, the kinetic energy condition for each multipacting process has to be checked. If the impact energies are too low or too high, no multipacting will occur even if the geometric conditions are satisfied. The kinetic energy check was done by computing the number α_n defined earlier for the potentially multipacting trajectories.

A. Coaxial cable: Scaling laws in SW operation

The multipacting analyzer was first applied to straight coaxial lines in standing wave (SW) operation. The computations were done in a half wavelength long section of the line.

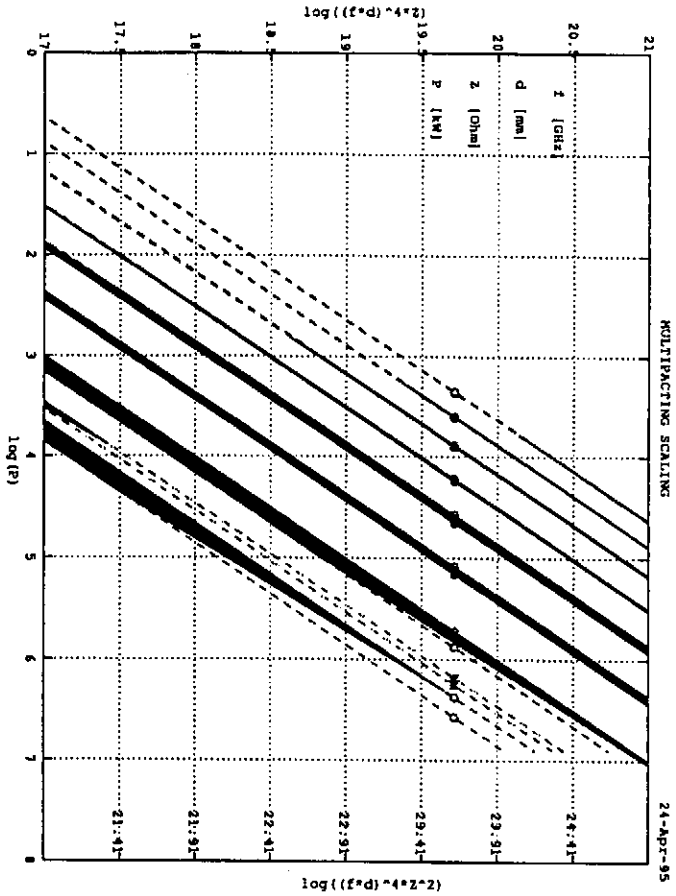

Figure. 1. Multipacting bands in coaxial lines

The following is a summary of the results. First, the analysis showed that multipacting in SW coaxial line fields is due to the electric field only. In fact, the powers that yield multipacting can be found by computing the trajectories at the electric field maximum only. Second, both one–point multipacting (from outer conductor to itself) and two–point multipacting (from outer to inner conductor and back) may occur. We analyzed the multipacting in lines with different sizes, different rf frequencies and different line impedances. It turned out that the multipacting powers obey quite accurately the following scaling laws:

$$P_{\text{one-point}} \sim (fd)^4 Z, \quad P_{\text{two-point}} \sim (fd)^4 Z^2,$$

where f is the rf frequency, d is a size parameter (in this paper d is the diameter of the outer conductor) and Z is the line impedance.

We computed the average impact energy of the electrons in multipacting trajectories. It was verified numerically that the average impact energy obeys roughly the scaling law

$$E_{\text{kin}} \sim (fd)^2,$$

in accordance to a simple dimension analysis. Typically the secondary electron yield for Niobium has a maximum around 400 eV, and is larger than one in the range $\sim$ 100 – 1500 eV.

Figure 1 is a graphical summary of the analysis. The upper horizontal axis is the natural logarithm of the number $(fd)^4Z$ (in (GHz×mm)^4×Ohm). The one–point multipacting powers for a given coaxial line can be found by computing this number, drawing a vertical line and reading the powers where this line intersects the bands marked by circles. The lowest band is the first order one–point multipacting band. The next band upwards is a two–point first order band, then follows a set of one–point bands, the order increasing up to 8 when one moves up in the figure to lower powers. The kinetic energy condition 100 eV $\leq E_{\mathrm{kin}} \leq$ 1500 eV when multipacting may occur is marked in the picture by shading. Similarly, the lower horizontal axis is the logarithm of the number $(df)^4Z^2$ (in (GHz×mm)^4×Ohm^2), characteristic for two–point multipacting. By computing this number and reading the intersection with the band marked with asterisks gives the multipacting powers. Note that there is only the first order two–point band in the picture; the higer order bands tend to get mixed with the more prominent two–point bands. Again, shading at the far left of the band indicates where the kinetic energy condition holds. With typical design parameters, the two–point process has a too large kinetic energy for multipacting. The circles and asterisks in the picture correspond to the 50 Ohm 1.3 GHz TESLA line.

B. Transition to TW operation

It is important to understand the behavior of the multipacting levels when the field switches from standing wave to the traveling wave, i.e., the reflected wave vanishes. We repeated the computation with the coaxial line with no reflected wave, and found that the multipacting levels shift according to the simple rule

$$P_{TW} = 4P_{SW},$$

i.e., in the traveling wave operation each multipacting level appears at four times higher one–way rf power. There is a simple physical heuristics behind this phenomenon: The peak voltage in standing wave operation is twice the peak voltage of the traveling wave. The analysis of the trajectories show, however that the situation is a bit more subtle, since the multipacting electrons have to be traveling as the wave form moves.

C. Other coaxial structures

The analysis algorithm has been applied so far to a set of coaxial structures. These include the tapered coaxial line and coaxial lines with an impedance step. Currently, we are running computations with grooved lines and certain ceramic window designs. The results will be reported in a forthcoming article.

D. Test cavity

To test the method, we made computations in a geometry where direct multipacting measurements can be made. A test cavity with a direct access to the multipacting current as well as the experiment are described elsewhere in this

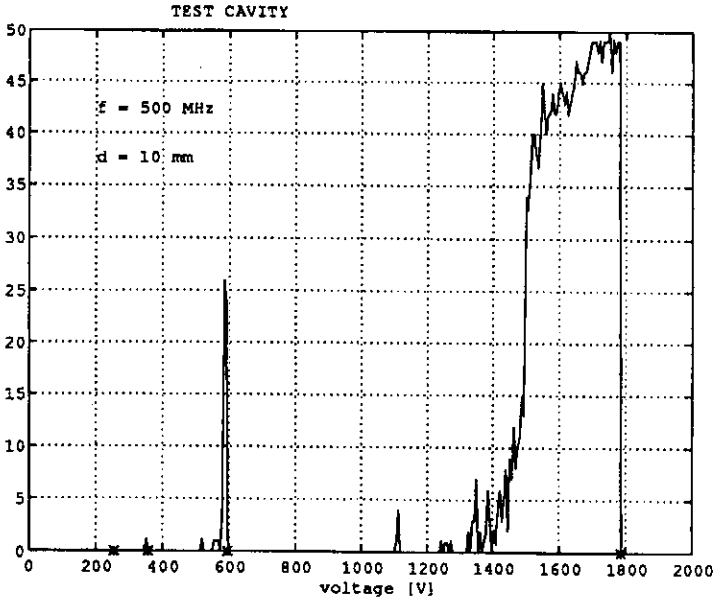

Figure. 2. Multipacting counter function for the test cavity

proceedings ([2]). The electric field in the gap between the electrodes is fairly homgenous, and two–point multipacting of order n between the electrodes is expected at voltage drop close to

$$V_{(n)} = \frac{m_e}{e}\frac{4\pi f^2 d^2}{2n-1}. \qquad (1)$$

This is the field giving resonant trajectories between two infinite parallel plates with time harmonic voltage drop. Figure 2 shows the counter function c_{30} versus the voltage between the electrodes on the symmetry axis. The two prominent bands correspond to the first and second order two–point multipacting between the electrodes. They agree well with the theoretical values (1), marked by an asterisk. The slight shift to the left is due to the positive initial velocity used in the trajectory calculations, not included in (1). This figure corresponds to the measured curve in Figure 3 in [2]. Let us mention that the computed kinetic energy for the second order process is typically too low to appear with secondary electron yields characteristic e.g. to Niobium surfaces.

References

[1] E. Somersalo, P. Ylä–Oijala and D. Proch: Electron multipacting in RF structures. TESLA Reports 14–94.

[2] D. Proch, D. Einfeld, R. Onken and N. Steinhauser: Measurement of multipacting currents of metal surfaces in RF fields. WPQ24 (This conference).

FIELD PROPAGATION EFFECTS AND RELATED MULTIBUNCH INSTABILITY IN MULTICELL CAPTURE CAVITIES

M. Ferrario#, A. Mosnier*, L. Serafini#, F. Tazzioli#, J.-M. Tessier*
#Infn, Frascati and Milano -- *Cea/Dapnia/Sea, Ce-Saclay

Field propagation effects during the filling and re-filling of the cavity are not harmful for a relativistic beam accelerated in a multicell standing wave cavity. On the opposite the beam dynamics of a non relativistic beam injected into a capture cavity can be significantly affected by the interaction with other modes of the fundamental passband, under beam-loading conditions. In fact, the dominant beating provided by the passband mode nearest to the accelerating π-mode introduces fluctuations on the accelerating voltage. The phase slippage occurring in the first cells, between the non relativistic beam and the lower modes, produces an effective enhancement of the shunt impedances, which are usually negligible for a relativistic beam in a well tuned cavity. In some cases simulations show a significant oscillation of the energy spread and transverse normalized emittance along the bunch train. As an example, we have applied our computational models to the beam-loading problem in the Tesla Test Facility (TTF) superconducting capture cavity.

I. INTRODUCTION

In addition to single bunch effects, induced in particular by space charge forces, multi-bunch effects due mainly to RF field propagation inside the cavity, will affect the quality of a non relativistic beam accelerated by standing wave structures. The study of these beam loading effects, which could limit the performances of injectors involving SW cavities, led to the development of numerical codes [1]: HOMDYN, which includes space charge effects and transverse motion and MULTICELL, which involves the longitudinal motion.

After a cavity filling time, the cavity is periodically refilled by RF power during the bunch to bunch interval. Although the generator frequency is set close to the accelerating π-mode, all the "modes" of the TM_{010} pass-band will be excited. Recently, in the aim to study the beam loading effect in the superconducting cavity TESLA for a relativistic beam, the multi-mode problem was solved by using systems of first order differential equations [2] or Laplace transforms [3].

In this paper, we use however a different approach, by directly solving the differential equations relative to each usual mode of the pass-band, provided that an intermode coupling term is taken into account. It can be shown in fact [4] with the help of the theory of coupled resonators, that the usual "modes" of the pass-band, found in the steady-state regime, are coupled through the external Q of the first cell, where the coupler is located, and not through the intrinsic wall losses of the cells.

The excitations Z_m of these "normal modes" of index m are then found by solving the following system (1) of coupled differential equations:

$$\ddot{Z}_m + \frac{\omega_o}{Q_o}\dot{Z}_m + T_{1m}\frac{\omega_o}{Q_{ex}}\sum_k T_{1k}\dot{Z}_k + \omega_m^2 Z_m = $$
$$= \frac{T_{1m}}{N\varepsilon}\frac{d}{dt}\int_{S'}(\vec{n}\times\vec{H}_n(\vec{r},t))E_{an}(\vec{r})\,dS + \qquad (1)$$
$$-\frac{1}{\varepsilon}\frac{d}{dt}\int_{V_{cav}}\vec{J}(\vec{r},t)\vec{E}_a^m(\vec{r})\,dV$$

The first driving term represents the generator current, while the second integral over the whole cavity represents the beam interaction with the mode m and will be computed during each bunch passage. The coefficient T_{nm} is the normalized excitation of mode m (m=1,M) at the center of cell n (n=1,N). The evolution of the M field amplitudes during the cavity filling and refilling driven by the generator current, together with the perturbation due to beam-loading, are found by numerical integration of system (1) coupled to the beam equations of motion. Since we are particularly interested in the evolution of amplitude and phase envelopes of the RF fields of the fundamental pass-band, which are slowly varying functions, this second order system can be easily transformed to a first order differential equations system [1].

II. RELATIVISTIC BEAM

In a well tuned cavity interacting with a relativistic beam, the average accelerating field vanishes for all modes, except of course for the π-mode. However, since the π-mode is coupled to the other excited modes through the Q_{ex}, some fluctuations remain.

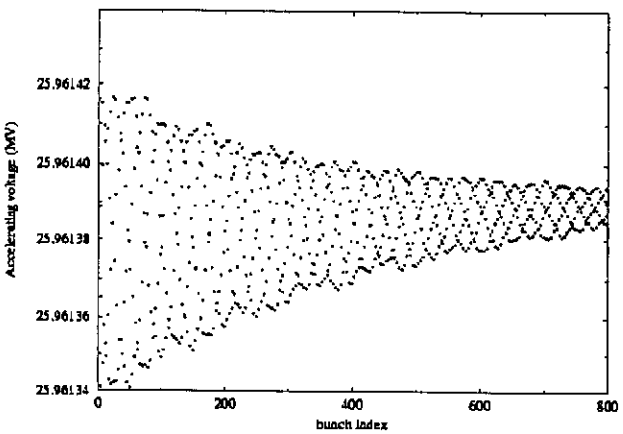

Figure 1 : Accelerating voltage evolution during 800 bunches

Figure 1 is a plot of the total accelerating voltage during the entire TESLA beam passage in a 9-cells SC cavity (bunch charge: 8 nC, bunch spacing: 1 μs, accelerating gradient: 25 MV/m), and points out the residual oscillations, mainly caused by the mode of the pass-band nearest to the π-mode, decaying according to the mode time constants $\tau = 2Q_{ex}/\omega$. The induced bunch-to-bunch energy spread is nevertheless very small, from 3 10^{-6} at the beginning to 0.5 10^{-6} at the end.

III. NON-RELATIVISTIC BEAM

With a non-relativistic beam the situation changes completely: the effects of the modes lower than the π-mode do not cancel any more. The phase slippage occurring in the first cells, between the non relativistic beam and the lower pass-band modes, produces an effective enhancement of the shunt impedances, which is usually negligible for a relativistic beam in a well tuned cavity. Furthermore, since the beam phase is slipping all along the structure, the field jumps and the detuning due to the off-crest beam vary from cell to cell. Some appreciable fluctuation of the output energy during the beam pulse is then expected. This multi-bunch energy spread is here estimated for the SC capture cavity of the low charge injector I of the Tesla Test Facility [5], (bunch charge: 37 pC, bunch spacing: 4.615 ns, accelerating gradient: 10 MV/m).

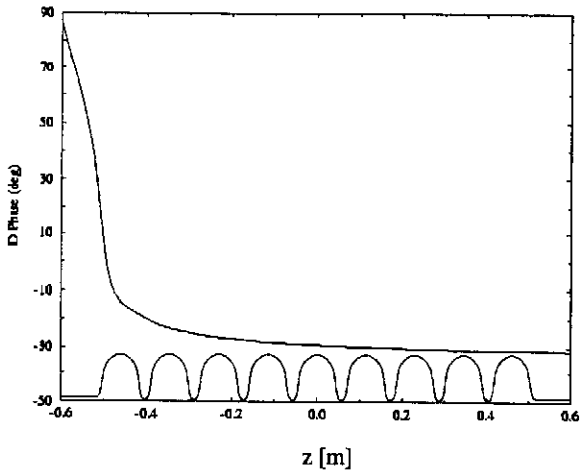

Figure 2 : Beam phase shift along the SC capture cavity (the cavity profile is also shown)

Figure 2 shows typical plots of the beam phase with respect to the RF wave for a single bunch crossing the 9-cell capture cavity. An injection energy of 240 KeV was assumed. Before reaching a stable value, the phase shift varies rapidly especially in the first cells. The total frequency detuning is about 110 Hz, i.e. almost one third of the cavity bandwidth.

Figure 3 shows the evolution of the energy gain on a short-time scale (1000 bunches), with the coupler linked to the cell n.1 or the cell n.9. The accelerating voltage exhibits fluctuations with a main beating due to the nearest 8π/9 mode spaced 0.76 MHz apart from the π-mode.

The beam loading effect is different according whether the power coupler is located upstream or downstream with respect to the beam. The shapes of the oscillations are similar and the multi-bunch energy spread amounts to 9 10^{-4} in both cases.

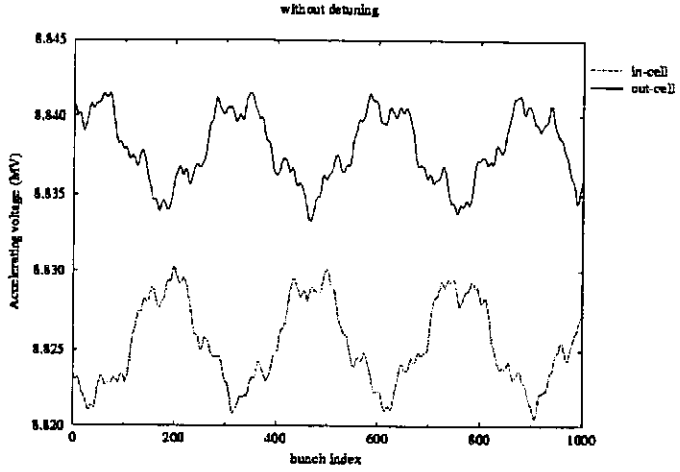

Figure 3 : Energy gain evolution during 1000 bunches

Figures 4 shows the accelerating voltage evolution on a longer time-scale, like the TTF beam pulse duration of 0.8 ms (about 173 333 bunches with injector I). The average compensation of the beam loading, by adjustment of the different parameters (generator, beam voltage or injection time), is not possible, resulting in a large slope on the cavity voltage at the beginning or at the end of the beam pulse.

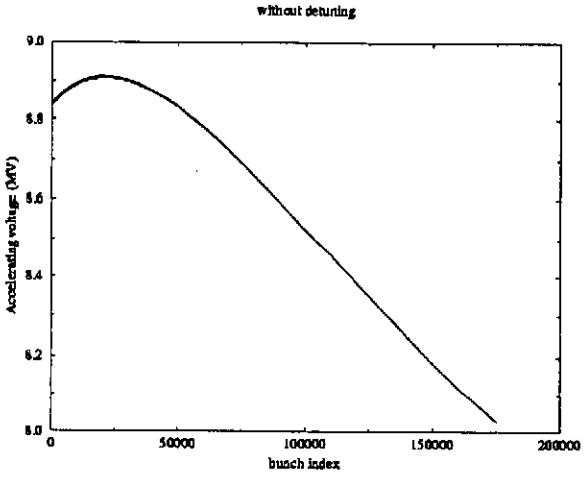

Figure 4 : Energy gain evolution on a long time-scale

IV. BEAM DETUNING COMPENSATION

When a beam is running off-crest, a cavity detuning, in addition to the critical coupling, is generally introduced [6] in order to cancel the reflected RF power and thus to minimize the RF power fed by the klystron. In the steady-state regime and for critical coupling, the tuning angle must be set to the RF phase with respect to the beam phase according to:

$$-\tau\,\Delta\omega_\pi = \tan\psi = \tan(\phi_{rf} - \phi_b)$$

The generator and the cavity voltages are then in-phase. Furthermore, it will be shown later that this beam-detuning compensation will decrease the cavity voltage fluctuations. The phasors diagrams are drawn on Figure 5, without (a) and with (b) cavity detuning.

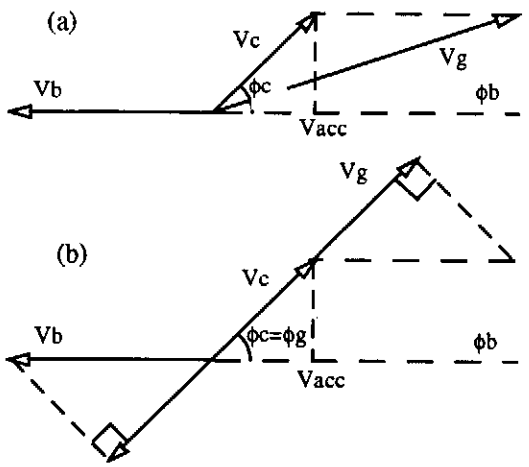

Figure 5 : Phasors diagram without (a) and with cavity detuning (b)

In order to have a constant accelerating voltage during the beam pulse, by balancing the rising generator voltage and the beam voltage, the beam should be injected after the beginning of the RF power pulse with a delay $t_0 = \tau \, Ln\, 2$ with cavity detuning or $t_0=\tau Ln(V_g \cos\phi_g/Vb)$ without cavity detuning. Both conditions, however, neglect the other modes than the π-mode

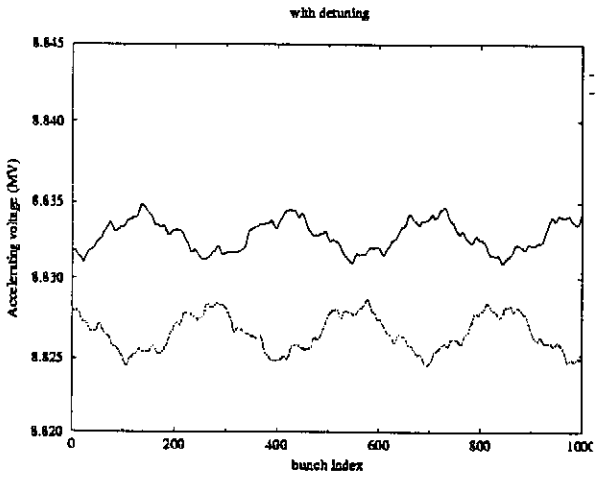

Figure 6 : Energy gain evolution with cavity detuning, solid line: out-cell, dotted line in-cell.

Figure 6 shows the energy gain with a cavity detuning of -110 Hz. The phase of the generator is assumed to track the cavity phase, at least during the field rise time. We note that the accelerating voltage fluctuations are about two times lower, giving a multi-bunch energy spread of 4 10^{-4}.

Figures 7 shows the accelerating voltage evolution on a longer time-scale: an average beam loading compensation can be obtained when the proper cavity detuning is introduced. We note again that the voltage oscillations decay with the time constants of the other modes of the pass-band.

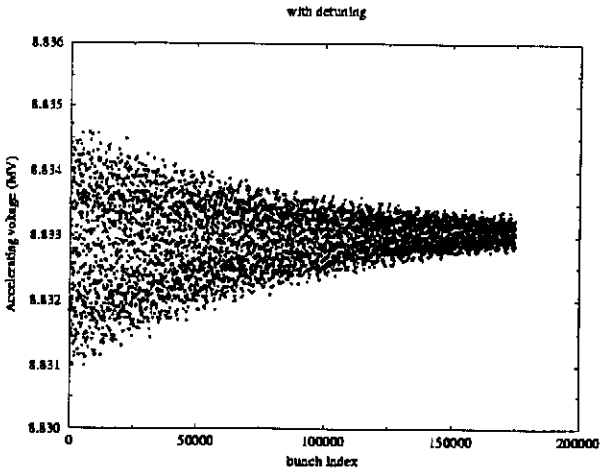

Figure 7 : Energy gain evolution on a long time-scale with cavity detuning

V.CONCLUSIONS

Although the propagation effects are not harmful for a relativistic beam accelerated in a multicell cavity, they have to be taken into account with non relativistic beams. In the latter case, the modes other than the π-mode introduce larger cavity voltage beatings. For the low charge TTF injector, the resulting bunch-to-bunch energy spread will be lower than 0.1% in any case. This value is nevertheless very small in comparison with the single-bunch energy spread of 3% , found with PARMELA simulations [5]. The impact on the transverse dynamics is also small: an rms normalized emittance fluctuation of 1% has been computed [1]. The TESLA cavity geometry is thus well suited to the capture section of the TTF injector.

With a larger number of cells or a smaller cell-to-cell coupling, stronger effects would have been obtained. On the other hand, we could imagine larger energy spreads induced by more critical beam parameters, like the bunch charge or the input energy.

VI.REFERENCES

[1] M. Ferrario, A. Mosnier, L. Serafini, F. Tazzioli, J.-M. Tessier "Multi-bunch Energy Spread induced by Beam Loading in a Standing Wave Structure", submitted to Particle Accelerators.

[2] H. Henke and M. Filtz, TESLA 93-26, 1993.

[3] J. Sekutowicz, Particle Accelerators, 1994, Vol. 45.

[4] A. Mosnier, "Coupled Mode equations for RF Transients Calculations in Standing Wave Structures", CEA/DAPNIA/SEA 94-30, see also [1]

[5] M. Bernard, B. Aune, S. Buhler et al., "The TESLA Test Facility Linac Injector", Proc. of EPAC, London, 1994.

[6] P.B. Wilson, AIP Conf. Proc. No 87 (AIP, New York, 1982), p. 474

MEASUREMENT OF MULTIPACTING CURRENTS OF METAL SURFACES IN RF FIELDS

D. Proch, Deutsches Elektronen-Synchrotron DESY, Hamburg, Germany and
D. Einfeld, R. Onken, N. Steinhauser, Fachhochschule Ostfriesland, Emden, Germany

Abstract

Multipacting currents can absorb RF energy and produce breakdown in high power components such as couplers, windows, higher order mode absorbers, etc.. This phenomenon starts if certain resonant conditions for electron trajectories are fulfilled and if the impacted surface has a secondary yield larger than 1. There are known recipes to reduce the secondary yield by coating techniques but the success rate is often unsatisfactory. Therefore we have started systematic measurements of the RF multipacting current. We measure the multipacting current between two electrodes of a specially designed coaxial resonator. Technical surfaces (Cu, plated Cu on stainless steel, Al, stainless steel) have been investigated before and after surface treatments such as chemical cleaning, baking and Ti coating. We present data for the strength of multipacting, start current, processing time and possible reconditioning.

I. INTRODUCTION

Multipacting is a phenomenon of resonant electron multiplication:

- one electron is accelerated by the electric RF field and hits the target surface after one even (odd) number of RF half cycles as resonant condition for one (two) surface multipacting,
- the impacting electron produces more than one secondary electron.

These two conditions have to be fulfilled in order to start an electron avalanche. This electron current might result in severe limitations of the stored energy in microwave components or finally ignite a breakdown. To suppress these limitations, the resonant condition can be avoided by proper choice of geometry. Resonant conditions for a parallel plate geometry in pure electric fields can be easily predicted and thus be avoided by the right gap distance. In the case of electromagnetic fields, however, multipacting is simulated by tracking programs. In the case of complicated three dimensional RF components a simulation of electron trajectories becomes very demanding. Furthermore the RF design might not allow to change the geometry by the needed amount.

Therefore attempts are undertaken to suppress multipacting by proper coating of critical surfaces. A material for coating is chosen which has a secondary yield of smaller than or at least near by one. Different coating materials are known, for example Ti, TiN, CrO_2, etc. [1] . Those materials have been investigated by measuring the secondary yield in DC experiments on sample surfaces. RF components might have complicated geometry to be coated. The improvement also depends on coating conditions of large technical surfaces. Therefore a test resonator was developed to measure the RF multipacting current directly under various coating conditions. For fast turn around this resonator should allow a fast exchange of the multipacting electrodes and should operate at low power. In this paper the design of such a test resonator is given and first measurements on different coatings are presented.

II. DESIGN OF THE TEST RESONATOR

The resonant condition for two side multipacting in an electric field is given by:

$$E_{(n)} = \frac{4m\pi}{e} \cdot \frac{f^2 l}{(2n-1)} \qquad (1)$$

n: order of multipacting (n:1,2,3,...)
f [Hz]: frequency
l [m]: gap distance
m [kg]: mass of electron
e [C]: charge of electron
$E_{(n)}$ [V/m]: resonant electric field gradient

The magnetic RF field in the center gap of a reentrant resonator is small as compared to the electric RF field. Therefore two side multipacting according to equation (1) is expected in such a resonator. The experiment prooved that multipacting actually occures at the predicted field levels. This

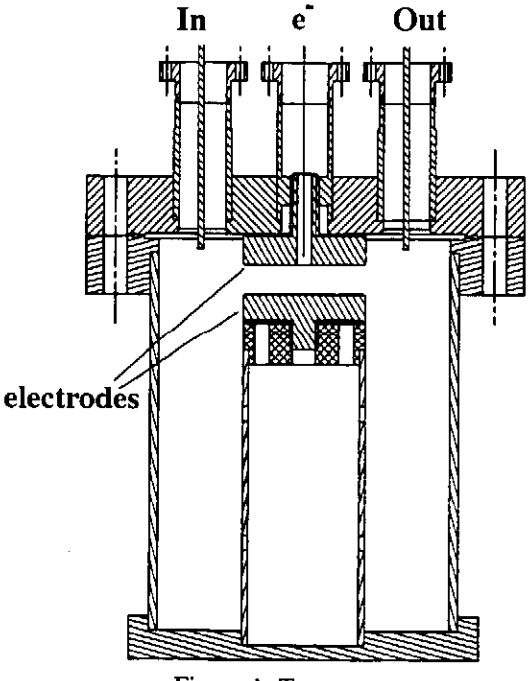

Figure 1: Test resonator

resonator has been also analysed by trajectory calculations and is discussed in [2].

A resonant frequency of 500 MHz has been chosen because of available laboratory equipment. The gap distance of 10 mm is rather large but hereby dimension tolerances by many assemblies can be neglected. Typically 10 watts of RF power is needed to reach first order multipacting. The diameter of the resonator is uncritical and was chosen according to available material.

The resonator is fabricated from copper (resonator) and stainless steel (flange) plated with copper. The two ports on the top cover are used for pumping and RF coupling. Both RF antennas have the same coupling in order to maintain the symmetry of the central electric field. A small coaxial line penetrates the upper center electrode to give a direct measure of the multipating current.

length	mm	113
outer diam.	mm	100
inner diam.	mm	42
gap distance	mm	10
resonance frequ.	MHz	500
RF power at 1 kV gap	Watt	3.2
typ. unloaded Q		5×10^3

Table 1: Data of the multipacting resonator

III. MEASUREMENT PROCEDURE

After assembly of a pair of electrodes the upper Conflat flange is closed and the resonator is pumped to better 10^{-6} mbar. The generator is locked to the cavity resonance and the antennas are calibrated at low RF field level. Then the RF power is modulated up to 20 watts with a saw-tooth generator of 0.1 Hz. The onset of multipacting current is measured and the order of multipacting is determined from the calibrated gap electric field gradient. The magnitude and the processing behavior of the mutipacting current are measured the following way:

- the RF cavity power is set to 5 watts above the onset of multipacting,
- the cavity is operated under these conditions with the generator frequency locked to the cavity,
- the multipacting current will decrease and the cavity field will increase until the electron current completely disappears. At this moment the cavity field will jump up to the undisturbed value,
- the cavity is operated for about 2 h after the first processing because sometimes multipacting will reappear.

From the above given procedure the following characteristic data are extracted:

- order of observed multipacting,
- typical decay time of multipacting current during processing,
- time needed to overcome multipacting,
- tendency of deconditioning.

IV. MEASURED RESULTS

For each measurement one pair of electrodes (= one sample) is prepared and installed. Most work has been done with Cu and stainless steel samples to calibrate the measurement equipment and to test the reproduceability of the multipacting behavior. 6 Cu samples (3 from OFHC copper, 3 from standard copper) and 4 stainless steel samples have been fabricated. After each measurement the samples were slightly chemically polished so that a new surface was prepared for the next measurement. Some Cu samples were coated with Ti (sputter technique), one sample was coated with TiN (thermal evaporation) [3]. Four stainless steel samples have been electroplated with 20 µm of Cu. Four samples (2 Cu, 2 Ti on Cu) have been stored in a plastic (PE) bag (filled with dry N_2) for one week. Table 2 summarizes the measured results. The numbers of the multipacting current and of the processing time are mean values of the individual measurements. They differ typically from measurement to measurement by 12 % (current) and 40 % (time). The value of the electric field at the onset of multipacting varies only by 7

MATERIAL	N	I [mA]	E1 [kV/m]	E2 [kV/m]	n	t [s]
Copper	18	2.92	132.1	188.4	1	2080
Copper (heated at 400°C)	2	3.52	145.8	231.4	1	1223
Cu, stored one week in PE bag	2	3.30	82.5; 139.0	108.9; 192.8	2 ; 1	>6500
Titanium on Copper	5	3.03	139.9	184.5	1	933,1
TiN on Copper	1	3.00	129.3	170.7	1	552
Titanium on Aluminum	2	2.88	141.8	183.4	1	885,5
Cu Ti, stored one week in PE bag	2	3.21	51.1; 123.6	68.1; 190.0	3 ; 1	>6500
Aluminium	7	4.30	54.7	69.4	3	>6500
Stainless Steel	18	3.37	69.3; 128.8	87.7; 147.6	2 ; 1	2781
Copper electrochemically plated on S.S.	7	3.33	132.7	183.8	1	2571

Table 2: Results of the multipacting measurements (N: number of measurements; I: multipacting current; E1, E2: electric field gradient at onset, stop of multipacting current; n: order of multipacting; t: processing time)

%. The order of multipacting is deduced from equation (1).

Figure 2 shows the typical processing behavior of Al, Cu and stainless steel samples. The multipacting current is plotted versus time under the condition of additional 5 watts RF power above the first onset of multipacting.

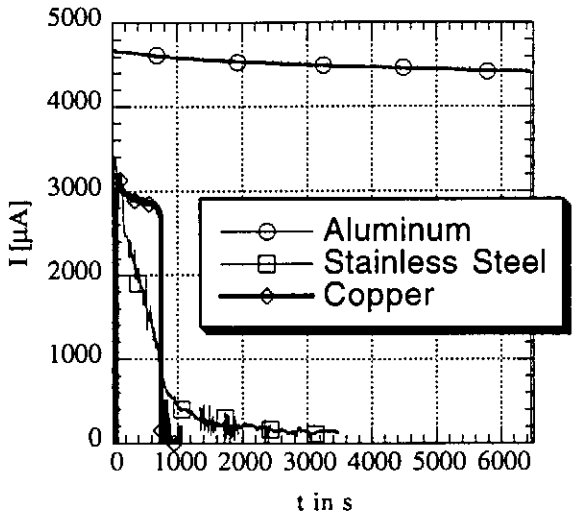

Figure 2: Multipacting current vs. time for 3 different metals

Figure 3 displays the multipacting current versus the gap voltage during processing. The multipacting current drops down so that the power being absorbed from the multipacting process decreases, too. Therefore the stored energy in the resonator and thus the electric field in the gap increase. The condition of equation (1) predicts a resonant voltage of 176 kV/m (n=1) for our geometry. The experiment shows multipacting between 150 and 210 kV/m. The width of the multipacting region is larger at lower multipacting orders. This is due to a spread of starting velocity and starting angle of the secondary electrons.

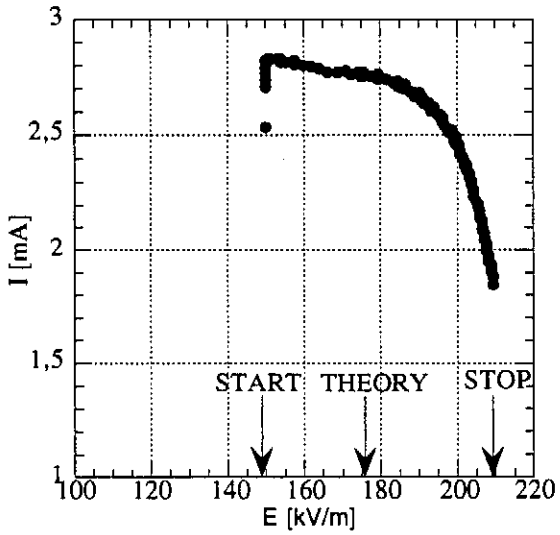

Figure 3: Multipacting current vs. electric field gradient for Titanium on Copper

V. DISCUSSION

All samples show multipacting of at least first order. They differ in magnitude of multipacting current and in processing time. Al samples show the worst behavior, as expected. They do not process within the measurement time of 6500 sec..The multipacting behavior of standard copper and OFHC copper does not differ at all. Heat treatment of 400°C, 6 hours, reduces the processing time to 60 %. Coating of Cu with Ti reduces the processing time to about 45%. A Ti coating of Al has a substantial improvement because of the strong multipacting behavior of the bare Al. After coating with Ti, samples from Cu and Al behave the same. Electroplated Cu on stainless steel is somewhat worse than pure copper before heat treatment.

One interesting result is the dramatic deterioration of Cu and Ti coated Cu samples after storage in a plastic (PE) bag. Both types of samples do not process within 6500 sec. after storage in the bag. This deterioration was also reported by another experiment [4]. The mechanism is not understood. One speculation is, that some lubricant in the PE foil penetrates to the metal surface of the sample. Nevertheless, the common practice to store or transport RF components in plastic bags should be avoided, if multipacting is of concern.

VI. ACKNOWLEDGEMENT

One pair of Cu samples was coated with TiN by M. Kuchnir, FNAL. We gratefully acknowledge this preparation.

VII. REFERENCES

[1] A. R. NYAIESH, E. L. GARWIN, F. K. KING and R. E. KIRBY; "Properties of Thin Anti-Multipactor Coatings for Klystron Windows"; SLAC-PUB-3760; August 1985

[2] E. SOMERSALO, P. YLA-OIJALA AND D. PROCH; "Analysis of Multipacting in Coaxial Lines"; FAE08; this conference

[3] M. KUCHNIR AND E. HAHN; "Coating Power RF Components with TiN"; Fermilab TM-1928; March 1995

[4] A. WOODE AND J. PETIT; "Investigations into Multipactor Breakdown in Satellite Microwave Payloads"; ESA Journal 1990; Vol. 14; p. 467-478

Status of the Design for the TESLA Linear Collider

R. Brinkmann, DESY, Notkestr. 85, D-22603 Hamburg
for the TESLA collaboration

Abstract

Among the different approaches towards a next generation 500 GeV (c.m.) Linear Collider the TESLA design uses superconducting accelerating structures operating at 1.3 GHz and a gradient of 25 MV/m. The particular features of TESLA are a high AC-to-beam power transfer efficiency and relaxed tolerances compared to the other approaches. This paper gives an update on the machine parameters and the overall design, including a discussion of the potential for an upgrade to higher center-of-mass energies.

I. INTRODUCTION

The different design studies for a next generation e^+/e^- linear collider fall, roughly speaking, in two categories: the high frequency approaches (NLC, JLC, VLEPP, CLIC), which aim at a high accelerating gradient and the low frequency approaches (SBLC, TESLA) operating at a lower gradient, but having the advantage of reduced rf peak power requirements and smaller wakefield effects in their larger aperture accelerating structures [1,2]. The TESLA design, with an rf frequency of 1.3 GHz at the lower end of this frequency scale, has the special feature of using superconducting cavities for the linac, which allows to accelerate many bunches in a long rf-pulse yielding a high rf-to-beam power transfer efficiency. An accelerating gradient of 25 MV/m with a quality factor (unloaded) of $Q_0=5\times10^9$ at T=2K is foreseen. The choice of 1.3 Ghz is a compromise between surface resistance ($\propto\omega_{rf}^2$) and R/Q (favoring a high frequency). Another argument is the availability of klystrons at this operating frequency. Whereas the advantages of very low wakefields and high acceleration efficiency are obvious, the challenge of TESLA is clearly to demonstrate that stable operation with a gradient of 25 MV/m can be achieved not only within a laboratory experiment but on a large scale. In addition, the costs of the s.c. structures have to be drastically reduced compared to systems built up to now. In order to demonstrate that these goals can be achieved, a test facility is under construction at DESY [3,4] in international collaboration with institutes in China, Finnland, France, Germany, Italy, Poland, Russia and USA contributing to the technical R&D and/or the design of the 500 GeV collider. In the following, the present status of design is described. After a discussion of general parameters, the layouts of the final focus and interaction region, the main linac and the injection system are presented. In section 5, the upgrade potential of TESLA is discussed.

II. PARAMETERS

Using basic relations for the luminosity and the beamstrahlung and assuming an optimum beta-function β_y^* at the interaction point (IP) close to the bunchlength σ_z, the luminosity is in good approximation given by:

$$L = const. \times \frac{P_b}{\gamma} \times \frac{< \Delta E / E >_{rad}^{1/2}}{\varepsilon_y^{1/2}}$$

where P_b is the average beam power, $<\Delta E/E>_{rad}$ the energy loss due to beamstrahlung and ε_y the normalised vertical emittance. With the extremely small wakefields in the s.c. cavities, the TESLA linac is ideal for preserving a small ε_y without excessively tight tolerances (see section 4). Making use of this fact, the TESLA parameters have recently been slightly modified towards a smaller vertical emittance (see table 1 for a comparison of the new with the original [2] TESLA parameters). The main benefit of the new parameter set is a reduced AC-power consumption which is now below 100 MW for the 500 GeV (center of mass) machine at unchanged luminosity. The tolerances in the linac still remain conservative and the vertical spot size at the interaction point (IP) is a moderate extrapolation of the recent achievement of the FFTB experiment [5] by about a factor of 3.5.

III. INTERACTION REGION, FINAL FOCUS, COLLIMATION

Keeping beamstrahlung at a low level is essential for acceptable background conditions and good energy resolution for the high energy physics experiment. The center-of-mass energy spread in TESLA amounts to $<\delta E/E>_{c.m.} = 1.5\%$. It could be further reduced for a top quark threshold scan to $<\delta E/E>_{c.m.} \approx 0.1\%$ by increasing the horizontal beamsize at the IP, still keeping the luminosity above 10^{33} cm^{-2} s^{-1}. With the relatively large spacing between bunches ($\Delta t_b=0.7\mu s$), the experiment can resolve individual bunch crossings. Thus the small numbers of e^+e^- pairs N_{pair} outside a mask with 5cm radius and 100mrad opening angle as well as the hadronic background [6] are easily handable.

For TESLA a head-on collision design with electrostatic separation of the beams after the final doublet is possible [7], see fig.1. This allows to use s.c. quadrupoles which provide a large aperture (a_Q=24 mm) for the disrupted beam and the beamstrahlung γ's emitted at the IP with large angles. A

layout for the separation of the outgoing from the incoming beam and for beamstrahlung collimation is under study [8].

Table 1: New parameters of the TESLA 500 GeV (c.m.) linear collider in comparison with the original design.

	NEW	OLD	
total length	32	32	km
t_{pulse}	800	800	μs
n_b/pulse	1130	800	
Δt_b	707	1000	ns
f_{rep}	5	10	Hz
N_e/bunch	3.63	5.1	10^{10}
$\varepsilon_x/\varepsilon_y$	14/0.25	20/1	10^{-6} m
β_x^*/β_y^*	25/0.7	25/2	mm
σ_x^*/σ_y^*	845/19	1000/64	nm
σ_z	0.5	1	mm
$<\Delta E/E>_{rad}$	2.9	2.9	%
Disr. D_x/D_y	0.2/11	0.4/8.5	
P_b (2 beams)	16.3	33	MW
P_{AC} (2 linacs)	88	154	MW
$\eta_{AC\text{-}to\text{-}beam}$	19	21	%
luminosity L	6	6	10^{33} cm^{-2}s^{-1}

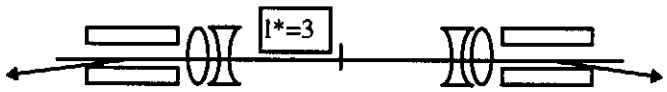

Fig. 1: Basic layout of the interaction region

The magnet lattice between the IR and the main linac consists of the final focus system (FFS) for beamsize demagnification and chromatic corrections, a collimation section to protect the IR quads from large amplitude particles and bending sections for creating a sufficient separation between two beamlines if the collider is to serve two experiments. The bend between collimation and the FFS also helps to reduce background due to muons originating at the collimators [9]. In total this "beam delivery" system is 1.5 km long (per beam). The momentum acceptance of the FFS (±0.6%) is well in excess of the beam energy spread (σ_E/E=0.1%).

The requirements for beam collimation are determined by the condition that synchrotron radiation generated in the doublet before the IP has to pass freely through the aperture of the final quad on the opposite side. This means that particle amplitudes have to be restricted to $12\sigma_x \times 35\sigma_y$ for TESLA. Continuous scraping of beam tails may not be necessary, since in the s.c. linac gas scattering is negligable and wakefields are small so that particles should normally not reach the above defined limits. Following concepts developed at SLAC [10], a design for simultaneous collimation in x,y and dE/E has been worked out [10].

IV. MAIN LINAC

The TESLA linac consists of basic units with one 9 MW klystron delivering rf-power to 32 9-cell 1.3 Ghz s.c. Nb cavities.

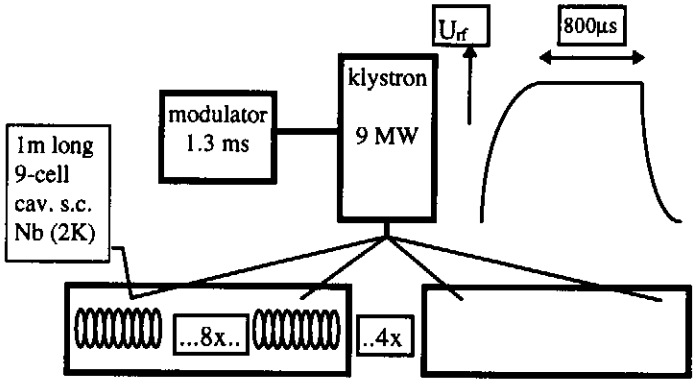

Fig. 2: Basic unit of the TESLA main linac

There are 8 of these 1m long cavities in one kryostat. The modulator produces a 1.3 ms long pulse, yielding a 0.8 ms long flat top accelerating field. The two TESLA linacs require in total 604 klystrons and 19,328 cavities. A focussing scheme using s.c. quadrupoles with scaling $\beta \propto \gamma^{0.2}$ (initial β = 22m) is foreseen [11].

One of the most important accelerator physics issues in a linear collider concerns preservation of a small (especially vertical) emittance in the linac. Emittance dilution caused by chromatic effects (dispersion, filamentation) due to energy spread in the bunch, short range wakefields and long range deflecting modes have been investigated [11]. With HOM-damping provided by two couplers per 9-cell cavity ($Q<10^5$), multibunch BBU leads to an effective emittance growth of only about 1%, assuming rather relaxed transverse rms position tolerances of 0.5 mm for the cavities and 0.1mm for the quadrupoles and beam position monitors (BPM's). A simple "one-to-one" orbit correction algorithm was applied in this computer simulation. With the same assumptions, the calculated emittance growth due to short-range wakefields and chromatic effects amounts to $\Delta\varepsilon_y/\varepsilon_y$ = 20%. A further reduction of emittance dilution is possible applying additional beam-based correction procedures [12]. With its relaxed tolerances, the TESLA linac will be rather insensitive to ground motion. In addition, the large bunch spacing allows to very effectively eliminate pulse-to-pulse orbit jitter. This is done by measuring the position of the first bunch and correct for the following ones with a kicker. Such devices would be installed at the beginning and the end of the main linac. The fast orbit correction method can also be applied to stabilise the beam position at the IP.

V. INJECTION SYSTEM

For TESLA it is necessary to compress the 0.8ms long bunchtrain in order to fit into a damping ring of reasonable size. Two options are presently discussed: A conventional ring with ≈6km circumference (like HERA-e) or a "dog-bone" shaped ring of ≈20 km length [13] which fits almost entirely (except for the arcs at the end) into the linac tunnel. One advantage of the latter design is an increased bunch spacing (80 ns instead of 25 ns for the HERA-e like ring), which relaxes bandwidth requirements for the injection/extraction system and the multibunch feedback. Recent beam optics studies for the dogbone ring show that the required emittances can be achieved with reasonable magnet position tolerances [14]. The possibility to use a rf-photo-gun to achieve the design emittance of the electron beam is being studied [15], which would allow to save one of the two damping rings.

Positrons are produced by converting γ's in a thin (0.4 radiation lengths) target. The required intense photon source is realised by passing the e^- beam after collision through a 30m long wiggler [16]. The method drastically reduces the heat load on the target and opens up the possibility to produce polarized positrons by using a helical undulator.

VI. UPGRADE POTENTIAL

With the relaxed tolerances of the low-frequency approach, TESLA is a very well suited design if one aims to push the vertical emittance towards a smaller value. A small ε_y becomes very important (if not inevitable) when an energy upgrade to 1TeV or higher is considered. How in detail the energy upgrade of TESLA would be realised depends on the progress on cavity development in the longer term future. Under conservative assumptions, the gradient has to be kept at 25 MV/m implying that a 1 TeV version of TESLA would have to double the length of the linac. However, neither this gradient nor the assumed quality factor of 5×10^9 are fundamental limits. Assuming a gradient of 40 MV/m as a future possibility, the machine with twice the length of the 500 GeV design could reach a center-of-mass energy of 1.6 TeV..The parameters for this machine are shown in table 2. A reduced bunch charge is used to facilitate preservation of the vertical emittance (first results of simulation studies show that this emittance can indeed been achieved with still relatively relaxed tolerances). A luminosity above 2×10^{34} cm^{-2} s^{-1} can be reached with an AC-power consumption increased by about a factor of 2.5 compared to the 500 GeV design.

Table 2: Parameters at 1600 GeV (c.m.) with an accelerating gradient of 40 MV/m at $Q_0 = 5\times 10^9$.

	TESLA 1.6 TeV	
total length	62	km
t_{pulse}	800	μs
n_b/pulse	2825	
Δt_b	283	ns
f_{rep}	3	Hz
N_e/bunch	1.8	10^{10}
$\varepsilon_x/\varepsilon_y$	10 / 0.03	10^{-6} m
β_x^*/β_y^*	35 / 0.7	mm
σ_x^*/σ_y^*	474 / 3.7	nm
σ_z	0.5	mm
$<\Delta E/E>_{rad}$	5.2	%
Disr. D_x/D_y	0.15 / 18.8	
P_b (2 beams)	39.2	MW
P_{AC} (2 linacs)	228	MW
$\eta_{AC\text{-}to\text{-}beam}$	17.2	%
luminosity L	23	10^{33} $cm^{-2}s^{-1}$

VII. REFERENCES

[1] J. Roßbach, "Options and Trade-offs in Linear Collider Design", contribution to this conference.
[2] R. Brinkmann, Proc. EPAC 94, London, Vol. I, p. 363.
[3] H. Weise, "The TESLA Test Facility (TTF) Linac- a Status Report", contribution to this conference.
[4] M. Leenen, "The Infrastructure for the TESLA Test Facility (TTF)- a Status Report", contribution to this conference.
[5] D.L. Burke, Proc. EPAC 94, London, Vol. I, p. 23.
[6] D. Schulte, thesis Universität Hamburg, 1995, to be published.
[7] O. Napoly et al., DESY-TESLA 94-31.
[8] A. Drozhdin, DESY-TESLA 94-29
[9] M. Sachwitz and H.J. Schreiber, DESY-TESLA 94-27.
[10] R. Brinkmann et al., to be published.
[11] A. Mosnier and A. Zakharian, Proc. EPAC 94, London, Vol. II, p. 1111 and A. Mosnier, private communication (1995).
[12] T. Raubenheimer, SLAC-PUB-6117 (1993).
[13] K. Flöttmann and J. Roßbach, Proc. EPAC 94, London, Vol. I, p. 503.
[14] R. Brinkmann et al., to be published.
[15] E. Colby et al., "Design and Construction of High Brightness RF Photo injectors for TESLA", contribution to this conference.
[16] K. Flöttmann and J. Roßbach, DESY-M-91-11.

THE TESLA TEST FACILITY (TTF) LINAC – A STATUS REPORT

H. Weise, for the TESLA Collaboration, Deutsches Elektronen-Synchrotron DESY,
22603 Hamburg, Germany

Abstract

The TESLA Test Facility (TTF) Linac, under construction at DESY by an international collaboration is an R&D test bed for the superconducting cavity variant of the TeV scale future linear colliders. The main body of the TTF Linac will consist of four cryomodules, each containing eight 1 meter long nine-cell cavities made from bulk niobium and operated at L-band (1.3 GHz) frequency. The base accelerating goal is 15 MV/m. While a first injector is going to be installed in 1995 and will provide 8 mA beam current within 800 μs long macro pulses at 216 MHz bunch repetition rate, a second injector based on a BNL like RF-gun combined with a standard TESLA cavity as preaccelerator and with a bunch compressor is under development. This injector will need to operate with a bunch charge of 5×10^{10} electrons at 1 MHz bunch repetition rate; the macro pulse length is again 800 μs and the injector output energy approximately 20 MeV. Overview and status of the linac construction will be given. Plans for the future use of the TTF Linac are presented.

I. INTRODUCTION

An electron-positron collider with a center of mass energy of 500 GeV and luminosity above 10^{33} cm $^{-2}$sec^{-1} should be considered as a possibility for the next accelerator facility after the LHC. This is a widespread consensus within the high energy physics community. Such a collider would provide for top analyses via $t\bar{t}$ production and discovery reach up to a Higgs mass of $\approx$350 GeV.

Worldwide, there are groups pursuing different linear collider design efforts. Several of these R&D groups plan to have working prototype test facilities in the 1997 time scale, this in order to establish well-developed collider designs. The TESLA activity [1] is one of these R&D efforts, differing from the others in its choice both of superconducting (s.c.) accelerating structures and of low operation frequency (1.3 GHz).

The TESLA Test Facility (TTF) is to be located at DESY, with major components flowing in from the members of the collaboration. The facility includes infrastructure to prove the feasibility of reliably achieving acceleration gradients above 15 MV/m in a series production. And the TTF has also to show that the in a LINAC test string (32 s.c. cavities) assembled accelerating structures can be successfully operated; this with the help of auxiliary systems (couplers, frequency tuners, cryogenics) to accelerate an electron beam to 500 MeV.

II. THE 500 MeV TTF-LINAC

In Fig. 1 (see next page) a plan view of the TTFL layout is shown. Being located in one of the DESY experimental halls the linac is within an approximately 100 m long shielded enclosure. From right to left an injector including its gun, a capture cavity, and a diagnostic section, is followed by a first cryomodule housing 8 s.c. cavities. A warm section allows for a later installation of a magnetic bunch compressor (see below, outlook) preceding another three cryomodules. The linac facility is finally completed by a diagnostic area which will be used extensively for beam experiments [2].

The operating parameters of the TTFL are given in Tab. I where the two columns Inj I/Inj II already list two scenarios for different injectors.

Table I
TTFL operating parameter.

Parameter	TTFL	
Linac Energy	500 MeV	
RF frequency	1.3 GHz	
Accel Gradient	15 MV/m	
Q_0	3×10^9	
# Cryo modules	4	
ΔE/E single bunch rms	$\approx 10^{-3}$	
ΔE/E bunch to bunch rms	$\approx 2\times10^{-3}$	
Bunch length rms	1 mm	
Beam current	8 mA	
Beam macro pulse length	0.8 ms	
Lattice β typical	12 m max	
	Inj I	Inj II
Injection Energy	10 MeV	20 MeV
Emittances (x/y), $\gamma\sigma^2/\beta$	$\approx 5\mu$m	$\approx 20\mu$m
Beam size σ, end of linac	250μm	500μm
Beam size σ, injection	1.7 mm	3.5 mm
Bunch frequency	217 MHz	1MHz
Bunch separation	4.6 ns	1μsec
Particles per bunch	2.3×10^8	5×10^{10}

In the first stage of installation the injector area includes a thermionic electron gun [3], a subharmonic prebuncher, the s.c. capture cavity, focusing lenses, and beam diagnostic equipment. The capture cavity is identical to one of the nine-cell structures (see Tab. II below) in the main linac. With its gradient of 15 MV/m the injected 250 keV electron beam will be accelerated to energies above 10 MeV. In the future, Injector I will be replaced by the high bunch charge Injector II [4] based on a laser driven rf gun. This injector comes close to the requirements of the TESLA Linear Collider electron source (5×10^{10} electrons per bunch, $\epsilon_n = 1\ \pi\ mm\ mrad$). The new installation will be located in the same injector area but needs some addi-

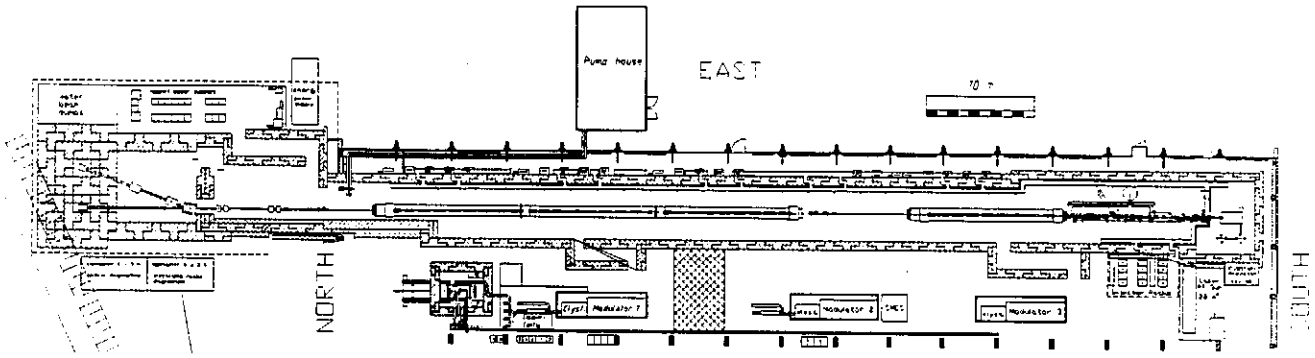

Figure 1. Plan View of the TESLA Test Facility Linac Layout.

tional space for the laser and for the klystron/modulator driving the rf electron gun.

Four cryomodules, each 12.2 m in length, comprise the main body of the linac. Each module contains eight nine-cell π-mode cavities and a quadrupole package. Thus, the beam optics is basically a periodic lattice with a cell length being identical with the module's length; the phase advance in the modified FODO lattice (the quadrupoles come in pairs) is $\pi/2$; matching to the lattice is performed by means of two triplet magnets. Depending on the finally achieved accelerating gradient (15 - 25 MV/m) the energy gain per cryomodule will be between 120 and 200 MeV. Each cavity has a RF power input coupler, two higher-order-mode (HOM) output couplers, a RF fundamental pick up, and a frequency tuning mechanism. Selected parameters of the cavities are given in Tab. II.

Table II
RF cavity parameters for the TTFL

Frequency	1.3	GHz
Cells per cavity	9	
Cavity length	1.036	m
Iris radius	35	mm
R/Q	1011	ohms/cavity
E_{peak}/E_{acc}	≈ 2.0	
RF power @ 25 MeV/m	206	kW/m
HOM k_{long}/cavity	8.5	V/pC (σ_z = 1 mm)
HOM k_{trans}/cavity	18	V/pC/m

The quadrupole package includes a superferric quadrupole doublet, transverse steering coils (two pairs, one each for permanent corrections and for vibration control), a transverse beam position monitor (cylindrical rf cavity), and a HOM absorber. Operation temperature of the quadrupole package is 4 K.

Every s.c. cavity has its own helium vessel and the whole string is supported by a long helium gas return pipe. Shielding against the earth magnetic field will be provided. Therefore, an unloaded quality factor of the cavities well above $Q_0 = 3 \times 10^9$ can be reached at operating temperature (1.8 K). The estimated heat load for all four TTFL modules is approximately 115/115/700 W at 1.8/4.5/70 K, this being calculated for a gradient of 15 MV/m and $Q_0 = 3 \times 10^9$. In this calculation the cold/warm transitions for the bunch compressor section are included. The first module will be equipped with a large number of temperature sensors as well as with vibration sensors. Alignment during cooldown will be monitored using optical methods and in addition to this using a stretched wire system. The latter can be used also during linac operation.

RF power for the main body of the linac will be provided by two klystrons and two modulators. Each klystron/modulator will deliver 4.5 MW with a pulse length of up to 2 ms. The first of these two rf power sources has been commissioned successfully [5]. The injector's capture cavity has its own klystron, the needed RF power within the macro pulse is below 100 kW. The rf gun needed for Injector II requires a few MW of RF power. Here it is foreseen to take advantage of a 10 MW klystron (1.3 GHz) which will be developed as a prototype for the TESLA Linear Collider.

The high energy beam analysis area behind the end of the fourth cryomodule serves as a room to measure the relevant beam parameters, i.e. beam position, beam size and emittance, beam energy and spread, beam current and transmission through the linac, bunch length and shape. Some parameters will be measured as a function of the bunch number in the 800 μs long bunch train, others as an average over some part or for a series of trains. In a first step standard beam diagnostics (scanners, screens and striplines) will be used while commissioning the TTFL. The extensive use of optical transition radiation is foreseen. Space for testing new diagnostic tools developed for TESLA will also be provided. Two beam dumps complete the whole TTF Linac set up.

III. FIRST RESULTS AND STATUS

At present, the commissioning of the TTF infrastructure [6] i.e. a chemical etching facility, a high pressure rinsing station, an UHV oven, and a preparation area/clean room is finished. Two prototype test cavities have been used to commission the cavity processing. Now, a complete preparation procedure includes cavity inspection, a first chemical etching, an UHV oven treatment (with Titanium at 1400°C inside and outside of the cavity), Tita-

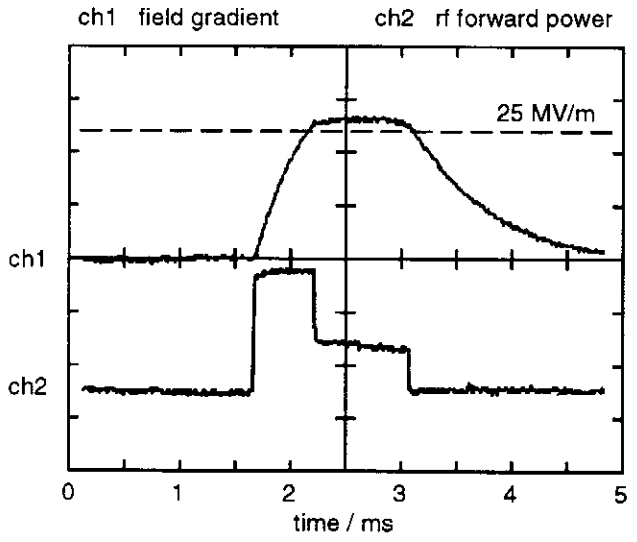

Figure 2. Field Amplitude and RF Forward Power in the First Series TESLA Cavity.

nium removal by a second etching, frequency tuning, final etching, and high pressure (100 bar) water rinsing. The first series cavity has been finished in mid March.

In Fig. 2 the shown oscilloscope traces represent the remarkable results of a first operation in the vertical test cryostat. The upper trace gives the field gradient as a function of time while the lower one is the measured forward power, both after some High Peak Power Processing [7]. The total rf pulse length is 1.3 ms, the first 500 μs are the filling time (exponential groth of the field gradient). At a reduced forward power the gradient was kept above 25 MV/m (the aimed TTF gradient is 15 MV/m) until after 800 μs the exponential decaying gradient relates to the switched off forward power. The decay time corresponds to the loaded quality factor; Q_o has been above 10^{10}.

The assembly of the first cryomodule needs 8 s.c. cavities and will start in summer '95. Injector I is going to be installed in fall '95; at present first tests are carried out at Saclay. The cryomodule installation is also planned for fall this year. It includes the warm/cold transitions and the cryogenic supply lines. A temporary beam line with quadrupoles, steerers, and diagnostics stations will take care of the beam transport between the end of the first module and the high energy experimental area. This area will have its main components installed until the end of the year. Thus, commissioning of the first module of the TTFL can take place by the end of 1995.

IV. OUTLOOK

Further milestones in the TTF Linac schedule are the assembly of the cryomodules #2 - #4 in 1996, the installation of these modules and the above mentioned injector II in early 1997, and the final commissioning with beam in summer 1997. Experiments with the beam will be carried out to study the different components of the linac and their influence on the electron beam quality.

Quite aside from its possible linear collider prospects, the TTF Linac is offering unique beam physics features. As a first application in experimental physics the construction of a Free-Electron Laser (FEL) is under discussion. Due to its exceptional capability to maintain high electron beam quality during acceleration for high charge densities, a superconducting linac might be an optimum choice to drive an FEL based on the Self-Amplified-Spontaneous-Emission (SASE) principle which would allow for the production of coherent radiation tunable in the photon energy range up to 200 eV (6 nm). This kind of FEL has no optical cavity, the electron bunch is just travelling through a long undulator and the spontaneous emitted field together with the periodic undulator field causes an electromagnetic potential (the so-called ponderomotive potential). Further downstream in the undulator the electrons are bunched in this periodic potential and then emit coherently. The achievable peak intensities can be extremely high, and they depend directly on the charge density of the electron beam. A detailed description of studies on such a FEL can be found in [8].

References

[1] The TESLA R&D effort (TESLA = TeV Energy Superconducting Linear Accelerator) is being carried out by an international collaboration. A number of institutions have joined the collaboration and include IHEP Beijing, TU Berlin, Max Born Institut Berlin, CEN Saclay, CERN, Cornell, Univ.Cracow, TH Darmstadt, DESY, TU Dresden, JINR Dubna, Fermilab, Univ.Frankfurt, INFN Frascati, INFN Legnaro, INFN Milano, INFN Roma II, FZ Karlsruhe, LAL Orsay, IPN Orsay, Polish Acad.of Science, IHEP Protvino, SEFT Finland, UCLA Dept.of Physics, Univ.Warsaw, Univ.Wuppertal.

[2] B. Aune, A. Mosnier, Experimental Program with Beam in the TESLA Test Facility, Proc. of the 1994 LINAC Conf., Tsukuba, Japan.

[3] T. Garvey et al., Simulations and Measurements of the TTF Phase-1 Injector Gun, this conference.

[4] E. Colby et al., Design and Construction of High Brightness RF Photo-injectors for TESLA, this conference.

[5] H. Pfeffer et al., A Long Pulse Modulator for Reduced Size and Cost, Proc. 21st Intern. Power Modulator Symposium, 1994, Costa Mesa, CA, USA.

[6] S. Wolff, The Infrastructure for the TESLA Test Facility (TTF) - A Status Report, this conference.

[7] J. Graber, High Gradient Superconducting RF Systems, this conference.

[8] J. Roßbach, Studies on a Free Electron Laser for the TESLA Test Facility, this conference.

THE INFRASTRUCTURE FOR THE TESLA TEST FACILITY (TTF) - A STATUS REPORT

S. Wolff, for the TESLA Collaboration,
Deutsches Elektronen-Synchrotron DESY, Notkestr. 85, 22603 Hamburg, Germany

Abstract

The TESLA collaboration is preparing the installation of a 500 MeV superconducting linear test accelerator to establish the technical basis for a future 500 GeV e^+e^- collider. The setup consists of 4 cryomodules, each containing 8 solid niobium cavities with a frequency of 1.3 GHz. The infrastructure to process and test these cavities has been installed at DESY. The facility includes a complex of clean rooms, an ultraclean water plant and a chemical etching installation for cavity surface preparation and cavity assembly as clean as possible. To improve the cavity performance a firing procedure at 1400°C in an ultra-high vacuum furnace is foreseen. An existing cryogenic plant has been modified to cool down the cavities below 2K and measure them in vertical and horizontal test cryostats. The RF power will be provided by a 4.5 MW klystron (pulse length 2 ms) in connection with a modulator. This system will also be used for a high peak power RF treatment to further improve the cavity performance by eliminating potential sources of field emission. The components of the complete infrastructure for the TESLA Test Facility are described and their status is reported.

I. INTRODUCTION

The theoretical accelerating gradient in a niobium superconducting cavity is limited to around 50 MV/m by the maximum value of the magnetic surface field occuring at the cavity equator. In practice the gradient is limited to substantially lower values by field emission from localized regions of the cavity surface. In the past few years however there has been dramatic progress both in the understanding of field emission mechanism and in its cures. By means of high pressure ultra clean water rinsing (HPR), ultrahigh vacuum baking at 1400°C with titanisation or by high peak power RF processing (HPP) developed at Cornell multicell structures at S- and L-band frequencies have exhibited more than 20 MV/m accelerating gradients.

To develop the surface treatment methods and the fabrication procedures required to produce high gradient multicell cavities on an industrial scale the TESLA collaboration first has started to construct and test forty 9-cell 1.3 GHz solid niobium cavities [1].

The necessary semiconductor standard clean rooms and the surface treatment facilities to process these cavities have been installed at DESY together with the equipment to test the cavity performance.

The most important components of this infrastructure are:
- a complex of clean rooms (300 m^2) for dustfree cavity assembly and treatment, to avoid cavity contamination
- a chemical etching facility complying with the purity standards of semiconductor industry
- an ultraclean water supply for rinsing the inner cavity surface to remove potential sources of field emission
- a high pressure rinsing facility for improved cleaning with ultra pure water of the inside of the cavity
- an UHV furnace to bake out the cavity up to 1500°C to improve the niobium material properties and to eliminate field emitters
- a high peak power RF facility to process cavities for further reduction of field emission
- vertical and horizontal helium cryostats to cool down and test the cavity performance at 1.8 K
- a cryogenic plant to provide liquid helium at 1.8 K and 4.5 K as well as helium gas at 70 K for the cryostats and the planned test linear accelerator

II. COMPONENT STATUS

The TESLA Test Facility (TTF) is located in an experimental hall of about 3000 m^2 surface area, which also houses the planned 500 MeV superconducting linear accelerator [2].

An overview of the TTF is shown in Fig.1.

A. Clean Room and Assembly Area

In order to avoid contamination of the cavity surface during processing and assembly a clean room has been built with an area of approx. 300m^2. The complex is divided into different classes, ranging from class 10000 down to class 10 (Federal standard 209), the last one being used for the most critical operations like mounting the input couplers to the cavity or connecting the cavities to a string for a cryomodule. Integrated in the clean room is the area for chemical etching of the cavity surface, the high pressure rinsing station and the UHV furnace. The clean room is operational since September 93.

B. Chemistry

Inside the chemistry area a cabinet for etching of the niobium cavities is installed. The acid in use is a mixture of $HF(40\%)/HNO_3(65\%)/H_3PO_4(85\%)$ of VLSI quality in a 1/1/2

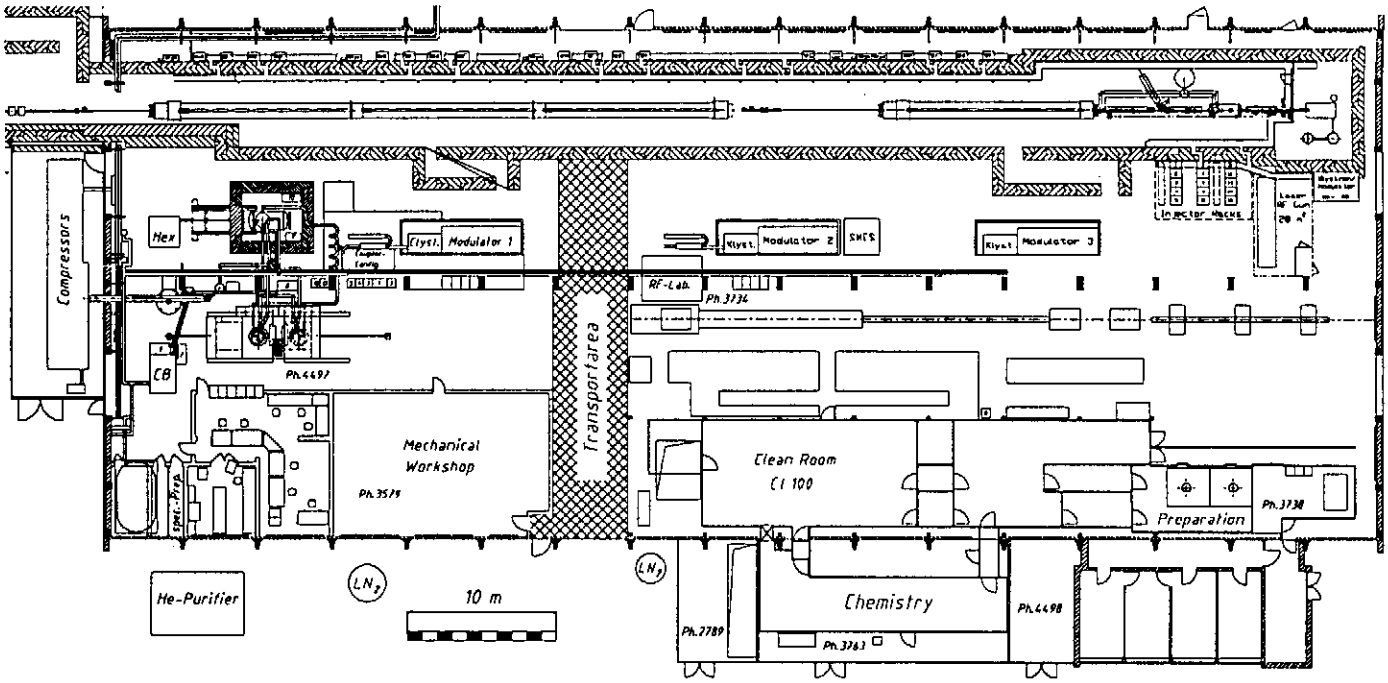

Figure 1: Overview of the TESLA Test Facility (TTF) at DESY.

volume ratio. For etching the cavity can be connected to one of two closed loops. One is operated with acid spoiled from earlier operations performed with a cavity right after reception or after titanisation, the so-called titanium loop. The other is operated with "clean" acid, the so-called niobium loop. In these loops the acid is circulating between the cavity and the storage tanks, which are located in a separate room outside the cleanroom. The pumps, tubes (made from PVDF) and filter elements (0.2µm size) of the chemical distribution system fulfill the standards of semiconductor industry.

The cavity can be etched from inside or from outside separately. For outside etching the cavity is sealed completely and inserted into a vessel which is then connected to the loop.

The standard cavity treatment consists of 5 etching operations. In the first two operations in a precleaning step for later furnace treatment and titanisation about 10 µm are etched off on the inside and on the outside of the cavity just after reception from industry. After titanisation the titanium-niobium surface is removed by etching off about 80 µm on the inside and 30 µm on the outside. Finally after tuning of the cavity outside the clean room a "clean" etching of about 20 µm in the "niobium loop" is performed in order to achieve the highest quality on the inner RF surface. The temperature of the acid can be set between 0° and 20°C with a mass flow of 10 *l*/min (improvement to 20 *l*/min is foreseen). The process itself and the safety interlocks are controlled by a computer to reach high safety and reproducibility standards. After the etching process the cleaning procedure is finished by an ultrapure water rinse. After the last "clean" etching a high pressure rinsing with ultra pure water is performed.

C. Ultrapure Water Supply

An ultrapure water plant supplies the cavity cleaning facilities with water of 18.2 MΩcm specific resistivity under (nearly) particle free conditions. Its first stage consists of a reverse osmosis unit (300 *l*/h), the second stage is equipped with nuclear grade mixed bed ion exchangers, augmented by filters and an ultraviolet light source. The point of use filters have a mesh size of 0.04 µm. A storage tank of 4000 *l* capability allows the use of large quantities of ultrapure water for cavity surface rinsing and cleaning. This plant is in continuous operation since August 93.

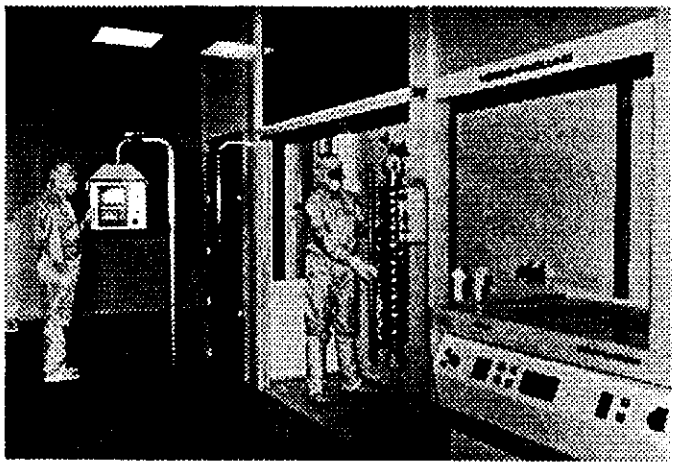

Figure 2: Cavity assembly in the clean room

Added to this facility is a high pressure rinsing station (up to 200 bar), which has been developed and built by CERN.

This unit allows the ultimate cleaning of the inner cavity surface and is in operation since July 94.

Fig. 2 shows the mounting of a cavity in the chemistry. The chemical facility is in operation since April 94.

D. UHV Furnace

Heat treatment of the complete cavity reduces potential sources for field emission and improves the niobium material properties like residual resistivity ratio ($RRR=R_{300K}/R_{10K}$) which is connected to thermal conductivity and homogeneity. During this process (at 1400°C and a vacuum of 10^{-7}mb) titanium is evaporated and builds up as a film on the inner and outer cavity surface. This effect leads to a solid-state gettering process for residual gases, especially oxygen, during high temperature annealing. The furnace for the TESLA cavities is in operation since December 94.

E. High Peak Power Processing (HPP)

Besides heat treatment in an UHV furnace the application of high power RF pulses (≈ 1 MW) for a short time (≈ 1 ms) to the cold cavity has proven as very effective to remove potential field emitters from the inner cavity surface. To apply this method for the TESLA cavities an HPP test stand has been built. It consists of a modulator supplied by FNAL and a klystron with a peak power of 4.5 MW at a pulse length of 2 ms. This setup (shown in Fig.3) is connected through RF wave guides with the vertical and horizontal cryogenic cavity test stands. The HPP facility is in operation since July 94.

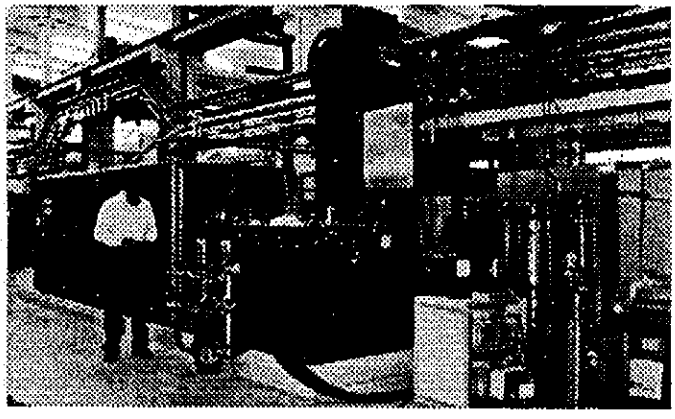

Figure 3: RF setup for HPP treatment

F. Cryogenics

For cooldown and test of the TESLA cavities an existing liquid helium plant has been extensively modified. By adding vacuum pumps and screw compressors a temperature of 1.8 K can be reached, with a refrigeration power of 100 W, which will be increased to 200 W for the test linac operation. The unit, which in addition provides helium at 4.2 K (400 W) and 70 K (2000 W), is connected to two vertical cold test stands built by FNAL and a horizontal test cryostat provided by CE Saclay. The liquid Helium plant is operational since December 93.

G. Cavity Performance

The first 9-cell cavities for TTF have been treated and tested using the above described infrastructure. The cavity treatment consisted of an inner and outer etching of 10 µm, a furnace treatment and titanisation of 4 hours at 1400°C followed by a chemical treatment removing 80 µm on the inside and 30 µm on the outside. After a mechanical tuning a chemical etching of 20 µm on the inside and a high pressure rinsing with 100 bar water pressure was performed. The mounting to the RF coupler was done in the class 10 clean room.

The Q_0 vs $E_{acc.}$ curves during CW operation before and after high peak power processing are shown in Fig.4. As can be seen from the graph the initial Q_0 is about $2*10^{10}$. With high peak power processing it was possible to raise the acceleration field to above 22 MV/m. The decrease in Q_0 value after HPP treatment is due to higher helium temperature.

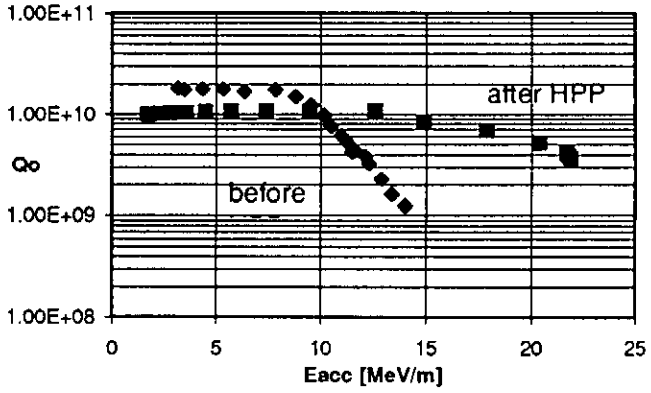

Figure 4: Performance of cavity D2 before and after HPP

III. SUMMARY

For the TESLA Test Facility (TTF) at DESY the complete infrastructure for superconducting cavity processing and testing is in operation. First series cavities have been processed with good results. It is expected that the so far achieved field strength of 22 MV/m during CW operation can still be improved by optimization of the process parameters.

IV. REFERENCES

[1] Proposal of the TESLA collaboration. TESLA Report 93-01.

[2] H. Weise, DESY, for the TESLA collaboration. Contribution to this conference.

Presented as Invited Talk FAE03 at the 1995 IEEE Particle Accelerator Conference, Dallas, TX, May 1-5, 1995.

HIGH GRADIENT SUPERCONDUCTING RF SYSTEMS

J. Graber, F.R. Newman Laboratory of Nuclear Studies, Cornell University, Ithaca, NY 14853 USA

Abstract

Superconducting Radio-Frequency (SRF) cavities are a promising technology for the next generation of electron positron colliders. In order to apply SRF technology in such machines, accelerating gradients must be improved, from the 5 to 10 MV/m level achieved in accelerators today, to the range of 20 to 30 MV/m. The state of the art in high gradient SRF technology will be discussed. Topics include achieved cavity performance, fabrication, preparation, handling, and processing techniques. Significant progress, e.g. multi-cell cavities with gradients > 25 MV/m and single-cell cavities with gradients > 40 MV/m, has been achieved over the past several years towards the goal of increased gradients. The major improvements have been in the areas of understanding and reducing cavity loading due to field emission and thermal quenches.

I. INTRODUCTION

Superconducting Radio-Frequency (SRF) technology has been an active field of research for accelerator cavities for the last 25 years. The SRF field has grown from the use of simple single-cell test cavities in a laboratory environment to reliable installation of hundreds of multi-cell structures in an operational accelerator. Hundreds of meters of SRF cavities are now used in accelerators around the world.

The SRF cavities used at such laboratories as KEK,[1] CERN,[2] Darmstadt,[3] Argonne,[4] and DESY[5] have retained their performance over time, showing SRF technology to be a reliable basis for continued construction of accelerators.

SRF cavities are presently being investigated as the basis for future electron positron colliders in the 0.5-2 TeV center of mass energy regime. Under the aegis of the TESLA[6] project, an international collaboration is operating towards this goal. SRF based accelerators present several advantages when compared with their normal conducting (NC) counterparts.[7]

Cryogenic considerations[8] have determined the choice of RF frequency for a high gradient cavity to be in the range of 1-3 GHz. Further consideration of thermal stability, wakefields, and availability of RF power sources has led the TESLA collaboration to the choice of a 9-cell 1.3 GHz cavity.

If SRF technology is to be used for construction of a TESLA machine, the accelerating gradients must be improved from the 5 to 10 MV/m level achieved in presently operated accelerators to 20 to 30 MV/m. In this presentation, I will review the efforts being made towards achieving this goal, showing the "state of the art" in obtaining high gradients, specifically as measured in multi-cell SRF cavities built for electron-positron machines.

It is useful to begin with a brief summary of the salient operational experience with SRF cavities in full accelerators. The observed limitations of these cavities will then be used as a launching point to discuss the current experimental efforts being pursued in order to overcome these limitations.

Finally, I will conclude with a discussion of future directions of SRF high gradient research.

II. OPERATIONAL EXPERIENCE

SRF cavities have proven themselves to be a viable and reliable basis for construction of accelerators. Cavities at DESY[9] and KEK[1] have to date logged many ten thousands of hours of operation with no significant degradation of cavity performance.

From the point of view of TESLA and other high gradient machines, it is most informative to investigate the experience to date of the SRF cavities of CEBAF. [10]

Figure 1 shows the achieved gradients in the CEBAF cavities, both in vertical testing and in horizontal commissioning in the accelerator. The cavities at CEBAF were constructed from niobium with RRR = 250. RRR (Residual Resistivity Ratio) is the ratio of bulk resistivity at room temperature to the NC resistivity at 4.2 K, and is used as a measure of the purity and thermal conductivity of the niobium.

The design parameters of the CEBAF cavities were an accelerating gradient of 5 MV/m, with an unloaded quality factor (Q_0) greater than 2.4 x 10^9 (operation at 2 K). In all, 338 cavities (in 169 pairs) have been installed in CEBAF, and have exceeded specifications. It is equally impressive that 70% of the cavities passed acceptance tests the first time that they were assembled and tested.

The excellent performance of the CEBAF cavities is

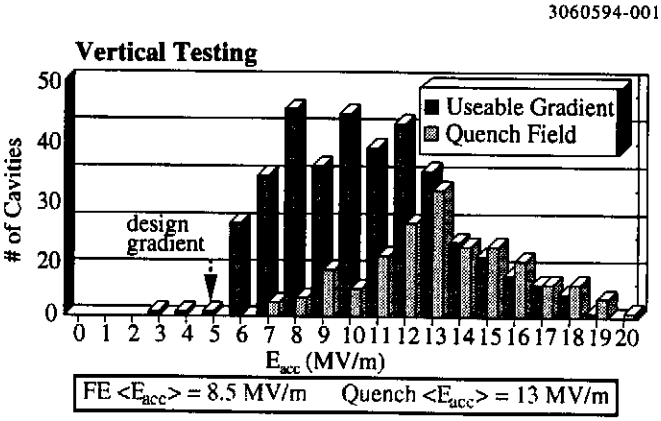

(a) Vertical tests of the cavities.

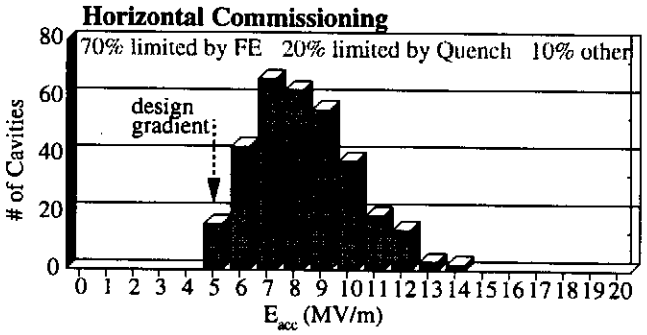

(b) Horizontal commissioning in the accelerator.

Figure 1. Results from CEBAF on 5-cell 1.5 GHz cavities.

nonetheless not adequate for the proposed TESLA machine. The two primary limiting phenomena for the CEBAF cavities are listed in Figure 1(a), quench (thermal breakdown) and field emission (FE). These are the same phenomena encountered in all other facilities with SRF cavities, and are thus the primary focus of nearly all SRF research groups. As is shown in Figure 1(b), 90% of the cavities installed in CEBAF had their final limitation due to one of these two phenomena.

It is worth noting that the achieved gradient and performance to date in CEBAF are significantly higher than that in previous facilities, largely due to the increased knowledge gained by the SRF research programs over the last 15 years.

III. STATE OF THE ART

For reasons of brevity, this discussion of the present state of the art of high gradients will be largely restricted to results obtained with multi-cell cavities, primarily because it is with multi-cell cavities that a TeV collider must be built. This approach will regrettably neglect excellent results obtained at many laboratories, including 1-cell test cavities,[11-13] and basic FE studies.[14,15] Interested readers are encouraged to consult the references for further information.

A. Quench

Quench, or thermal breakdown, is the phenomenon where as cavity fields are increased, a local heat source (defect) increases its dissipation until the heat dissipation overwhelms the local thermal conductivity, raising the local temperature of the RF surface above the critical temperature. The local hot spot will quickly grow to macroscopic size, eventually driving the entire cavity RF surface normal conducting, which then collapses the cavity fields.

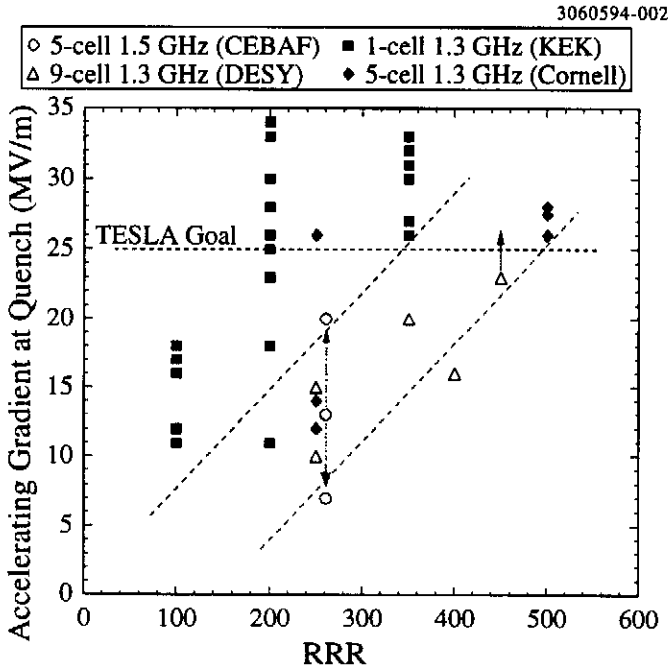

Figure 2. Achieved accelerating gradient plotted as a function of RRR (residual resistivity ratio) of the niobium in the cavities. A more complete description of this plot is provided in the text.

The most natural solution to the problem of quench is increased thermal conductivity, in order that the dissipated heat can be conducted away before the critical temperature is surpassed. The most common method for obtaining higher thermal conductivity has been to improve the purity of the bulk niobium used in cavity fabrication. Figure 2 displays measured quench fields at several different laboratories plotted as a function of cavity RRR. The data from CEBAF in Figure 1(a) is shown in the form of its average and range. The two diagonal lines are meant to show an approximate value of RRR necessary to insure a quench field above a given value. The upper line is for 1-cell cavities, while the lower line bounds the 5-cell and 9-cell cavities.

The purity of bulk niobium as delivered by industry has increased from RRR = 40 in the early 1980s to in excess of 500 today. Through solid state gettering,[16] the RRR can be further increased by up to a factor of 2, making RRR $\geq$ 1000 now a possibility. Extrapolation of the plots in Figure 2 show that RRR $\geq$ 500 is necessary for multi-cell cavities with quench fields consistently above E_{acc} = 25 MV/m.

One more possibility for increased thermal conductivity is the possibility of niobium-copper sputtered cavities,[17] where the increased thermal conductivity of the copper substrate would be used to conduct the heat. This technology is not yet feasible, however, due to an exponential decrease in Q_0 with increasing fields from granular superconductivity effects.

B. Field Emission

Field emission has been the dominant limitation on SRF cavities for the last ten years (since niobium with RRR greater than 100 became widely available). FE is tunneling of electrons out of the niobium surface in the presence of high surface electric fields. Many comprehensive reviews of the subject and its relationship to SRF cavity behavior are available.[18-21] FE related dissipation grows exponentially with increasing fields, quickly consuming all power available in a low power SRF setup. Furthermore, the impact of emitted electrons on the cavity surface causes heating, further degrading the RF performance of the cavity.

The most important information that has come from field emission studies, in both DC[14,22] and RF[15,23] conditions, is that FE is directly related to micron sized surface contaminations, in particular metallic particles. Table 1 shows a listing of the various contaminants found in emission studies at several different laboratories. Most of the elements detected can be traced to either actions or materials related to the processing or assembly of the cavities and their test apparati.

Recent results indicate the further possibility that RF surface contamination could lead to a thermal quenches.[26]

TABLE 1. Contaminants found in FE sites.

Geneva DC	Saclay DC	Wuppertal DC	Cornell RF
Ag,Al,C,Ca, Cr,Cu,Mn,O, S,Si,W	Ag,Al,C,Ca, Ci,Cr,F,Fe, K,Mg,N,Na Ni, O, Si, Ti, Zn	Al,Cs,Ca,Cu, Mn,O,S,Si Ti,W	C,Ca,Cr,Cu F,Fe,In,Mn Ni,O,Si,Ti

Given the effect of surface preparation on FE performance, the thrust of many of the investigations into SRF cavities has been in the area of producing a cleaner RF surface. It is likely that the most important gains in performance have come through use of clean rooms and protocols for assembly of cavity testing systems. Past studies on ultra high vacuum baking of the cavity[24,25] produced the first major breakthroughs to the 20 to 30 MV/m range that we seek. However furnace treatment is an expensive procedure, in time and resources, thus the effort to find alternative methods of obtaining clean, and therefore emission free, surfaces has been continued.

Recent, promising results have been obtained at several laboratories using a high pressure water rinse (HPR) as the final step prior to assembly to the vacuum apparatus. In HPR, a jet of ultra pure water (pressure ≥ 80 bar), is used to dislodge surface contaminants which are believed to be resistant to more conventional rinsing procedures.

An example of an HPR results on a 5-cell cavity at CEBAF is shown in Figure 3. On first measurement, the cavity was limited as shown to E_{acc} = 9 MV/m, with severe FE loading. The cavity was disassembled, rinsed with HPR, and then reassembled. Upon re-testing, the open circled curve was measured, limited only by a quench at 14 MV/m.

1-cell cavities have had even more impressive results, with many different labs[11,12,27] reporting multiple measurements of accelerating gradients in excess of 30-35 MV/m following HPR treatment. Indeed, the highest gradient reported to date is E_{acc} = 43 MV/m in a 1-cell cavity tested at CEBAF following HPR.[28]

Despite this promising work, however, consistently emission free surfaces continue to elude us, especially in the case of multi-cell cavities, where the larger surface area brings a proportionally larger probability of a contamination. One emitter is sufficient to limit the performance of an SRF cavity to unacceptable levels. This concern is especially daunting when one considers that with the proposed gradient, a 0.5 TeV collider would require 20,000 cavities.

The best results in reducing or eliminating FE after the cavity has been assembled have been obtained through High Power Processing (HPP).[29] HPP is an extension of the successful practice of conditioning an RF cavity, where the

3060594-004

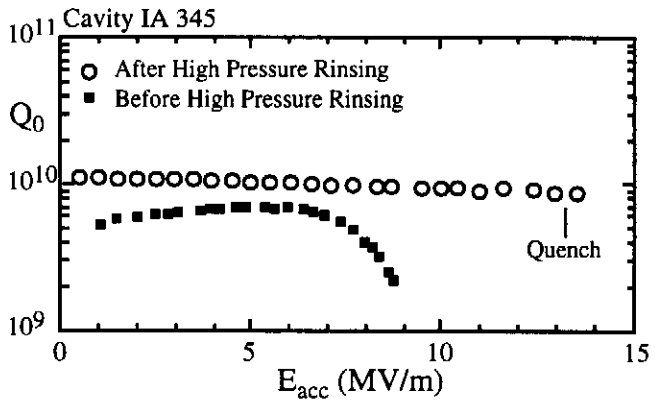

Figure 3. Q_0 vs. E_{acc} plots showing high pressure rinsing results on a 5-cell 1.5 GHz cavity at CEBAF.

3060594-005

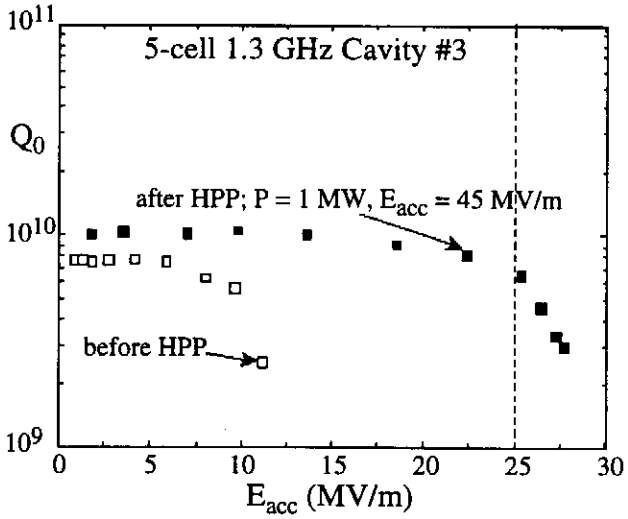

Figure 4. Q_0 vs. E_{acc} plots showing high power processing (HPP) results on a 5-cell 1.3 GHz cavity at Cornell.

emission in a cavity is reduced to acceptable levels through gradual raising of the incident power. Thermometry has shown that processing occurs through a local reduction in FE,[29] as evidenced by reduced electron impact heating. Microscopic investigation of RF surfaces following processing[23,29] has determined that processing occurs when the FE current is raised high enough to cause melting and/or vaporization of micron sized regions of the RF surface, presumably the emitter.

Continuous wave (CW) low power (≤ 100 W) RF processing of SRF cavities is severely limited by the exponential growth of the power dissipation under FE conditions. All available power is consumed before the fields, and therefore the FE current, can be raised high enough to initiate processing. With HPP, the incident power is raised to the order of hundreds of kilowatts to a megawatt, allowing fields to be increased high enough for processing to occur. Figure 4 shows the Q_0 vs. E_{acc} plot of a 5-cell 1.3 GHz cavity tested at Cornell. The pattern of measurement shown is typical: a cavity is severely limited by FE, which is impervious to conventional, low power, RF processing. HPP is applied with high power (in this case up to 1 megawatt), following which the attainable CW fields are greatly improved, sometimes by more than 100%. Three different 5-cell 1.3 GHz cavities reached gradients higher than 25 MV/m with this procedure.[30]

Studies of HPP on multi-cell cavities at both 1.3 GHz and 3 GHz have shown that success in processing is directly related to the magnitude of the fields reached during the HPP procedure. Put more succinctly, as long as the fields continue to increase in HPP, the CW performance will similarly improve. Empirically, it has been found in 5-cell 1.3 GHz that FE loading will be essentially eliminated in fields up to 50 % of the level reached during HPP.[30]

Finally, HPP also provides the possibility for *in situ* treatment of cavities which have been degraded by vacuum accidents. Normally a vacuum accident would require complete disassembly and re-cleaning of an affected cavity. With HPP,

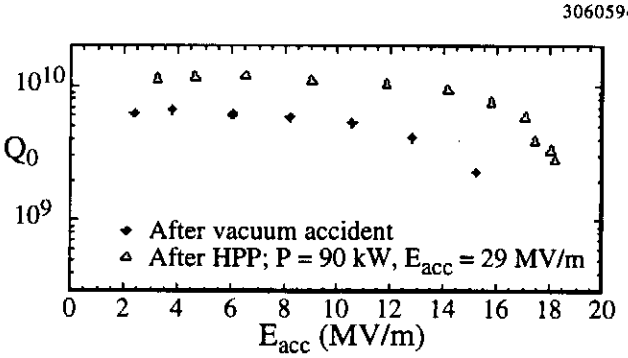

Figure 5. Q_0 vs. E_{acc} plots showing recovery of cavity performance with HPP following a vacuum accident.

the principle has been established that the cavity could regain all or most of its pre-accident performance without disassembly. Three separate 9-cell 3 GHz cavities were tested following vacuum accidents,[29,31] and, in each case, at least 80% of the cavity's previous performance was regained through HPP. The Q_0 vs. E_{acc} plots for one of these accidents are shown in Figure 5.

C. Putting It All to Work: The TESLA Test Facility

In order to further demonstrate the feasibility of the TESLA approach to a TeV collider, the TESLA Collaboration has begun work on the TESLA Test Facility (TTF), a 50 meter, SRF based linac, to be constructed with SRF technology at DESY. Current status of the TTF was discussed in another presentation at this conference.[32,33]

In setting up the TTF, the TESLA Collaboration has taken advantage of the latest information from the SRF community regarding the best methods of preparing cavities for RF performance. The TTF has a state of the art chemical and clean room facility, which includes a high pressure rinse system capable of delivering rinse water at up to 100 Bar, and a UHV furnace for surface preparation and/or RRR improvement. Figure 6 shows the Q_0 vs. E_{acc} plots from measurement of the capture cavity, which was procured by Saclay, then prepared and tested at DESY. As can be seen, the cavity

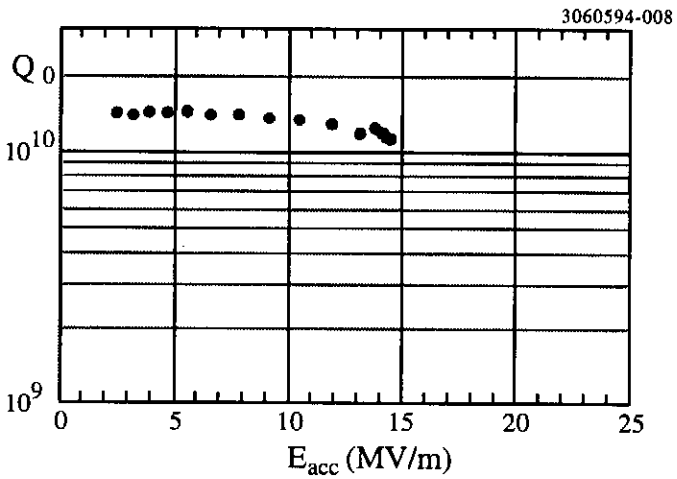

Figure 6. Q_0 vs. E_{acc} plot showing the performance of the TTF capture cavity (9-cell, 1.3 GHz, RRR = 250), tested at DESY.

was essentially emission free up to 14.5 MV/m, where a quench was encountered. This cavity has RRR of only 250, as it is designed for operation at only 12 MV/m.

The TTF also has an HPP setup capable of delivering up to 1 Megawatt pulses of up to 2 msec. The HPP procedure has been successfully used on several cavities to date, the most successful being the vertical test of cavity # 2, a production cavity with HOM couplers.

Figure 7 shows the CW measurements; through HPP processing, the cavity reached a CW accelerating gradient of 22 MV/m. More significantly, during HPP, the cavity was operated in the conditions prescribed for TESLA- input coupling Q_{ext} = 3 x 10^6, RF pulse length = 1.3 msec, incident power of 250 kW. Figure 8 shows oscilloscope traces of the power transmitted to a monitor probe (upper trace), and the incident power delivered to the cavity (lower trace). As can be seen in Figure 8, the cavity reached an accelerating gradient of

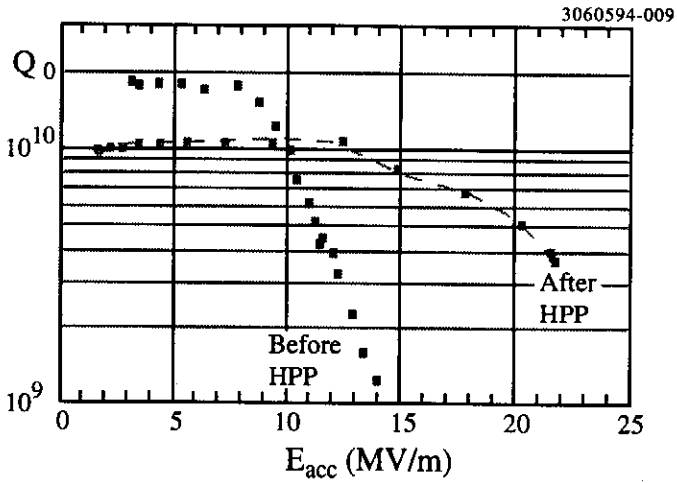

Figure 7. CW Q_0 vs. E_{acc} plots of TTF cavity #2, (9-cell, 1.3 GHz, RRR = 350), before and after HPP (P ≤ 400 kW, E ≤ 32 MV/m).

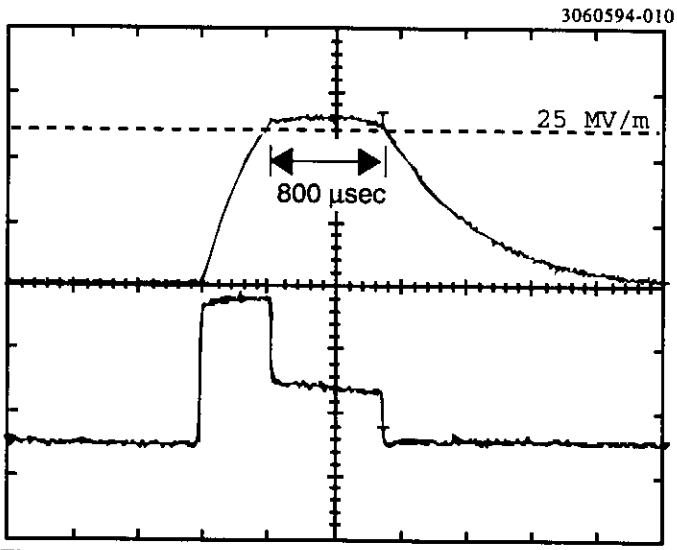

Figure 8. Oscilloscope traces captured during operation of TTF Cavity #2 operated under pulsed conditions at an accelerating gradient of approximately 26 MV/m. A description of this figure be found in the text.

26 MV/m after filling for 500 μsec. At this point, the forward power was stepped down to 100 kW, in order to simulate the effect of beam load on cavity fields. The cavity maintained E_{acc} = 26 MV/m for the entire 800 μsec designed for TESLA operation, and then decayed away naturally when the incident power was turned off.

Horizontal testing, followed by installation in the TTF, of this and subsequent cavities will proceed beginning this summer.

IV. FUTURE DIRECTIONS AND REMARKS

The prospect for further gains in high gradient superconducting RF accelerators is very bright. The concerted research effort undertaken in the last fifteen years to extend the attainable gradients has paid off with significant gains. The progress in achieved gradients (CW testing) is shown clearly in Figure 9. The maximum achieved gradients at the time of compilations in 1980 and 1989 are included as line plots for reference to show the gains made over time. Nearly all research in extending gradients today is being performed with 1-3 GHz cavities, with surface area between 0.05 and 0.8 square meters, hence the lack of gains in other regions.

The two primary limiting phenomena, field emission and quench are well understood. Improved purity of niobium has increased quench limits significantly. A clean RF surface is the most important determining factor in reducing FE. HPR and clean assembly procedures are helping provide such a surface. HPP is effective in reducing field emission in cavities which exhibit FE in spite of clean assembly procedures.

The design gradient for TESLA has been met in vertical testing of the TTF cavity at DESY. Repetition of this measurement in a horizontal cryostat, followed by installation in the TTF are scheduled for later this summer. By the 1997 PAC, we expect to show how the TTF project has further demonstrated the feasibility of TESLA.

3060594-011

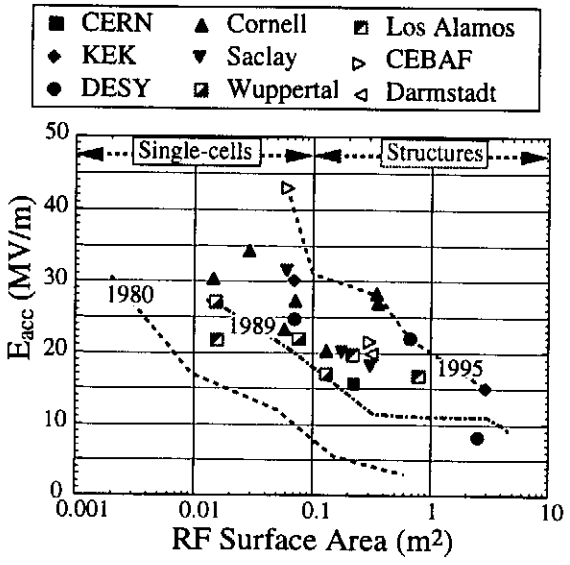

Figure 9. Historical progress in the attainable accelerating gradients, plotted as a function of RF surface area per cavity. High gradient studies are now performed primarily for cavities with area between 0.05 and 0.8 square meters.

VI. ACKNOWLEDGMENTS

The author would like to thank the following for their assistance and input in preparing this paper: H. Padamsee (Cornell); D. Proch, W.-D. Moeller, and M. Pekeler (DESY); S. Noguchi and E. Kako (KEK); B. Rusnak (LANL); W. Weingarten (CERN); B.Bonin (Saclay); P. Kneisel and C. Reece (CEBAF).

VII. REFERENCES

[1] K. Akai, *Proc. of the 5th Workshop on RF Superconductivity*, D. Proch ed., DESY, Hamburg, Germany, **DESY M-92-01**, 126 (1992).
[2] G. Cavallari, et al, *Proc. of the 6th Workshop on RF Superconductivity*, R. Sundelin ed., CEBAF, Newport News, VA USA, 49 (1994).
[3] H.D. Graef, et al, ibid ref. 2, 1203 (1994).
[4] K. W. Shepard, et al, ibid ref. 2, 1 (1994).
[5] B. Dwersteg, et al, *Proc. of 4th European Particle Accelerator Conference*, London, England, 2039 (1994).
[6] R. Brinkmann, this conference paper RPC07.
[7] H. Padamsee,et al, *Ann. Rev. Nucl. Sci.* **43**,635 (1993).
[8] D. Proch, ibid ref. 2, 382 (1994).
[9] C. Hovater, ibid ref. 2, 198 (1994).
[10] C. Reece, et al, this conference paper FAE12.
[11] D. Reschke, et al, ibid. ref. 2, 1095 (1994).
[12] B. Bonin and M. Juillard, ibid ref. 5, 2045 (1994).
[13] B. Rusnak, et al, *Proc. of the 1993 IEEE Particle Accelerator Conference*, Washington DC, USA, 1021 (1993).
[14] J. Tan, et al, *J. Phys D: Appl. Phys.*, **27**, 2654 (1994).
[15] E. Mahner, ibid ref. 2, 252 (1994).
[16] H. Padamsee, *IEEE Trans. Mag.*, **21**, 1007 (1985).
[17] D. Bloess, et al, ibid ref. 5, 2057 (1994).
[18] P. Kneisel, *J. Vac. Sci. Technology*, **A11**, 1575 (1993).
[19] W. Weingarten, *Particle World 1*, 93 (1990).
[20] Y. Kojima, *Proc. of the 1991 Particle Accelerator Conference*, San Francisco, CA, USA, 16 (1991).
[21] D. Proch, ibid ref. 13, 758 (1993).
[22] Ph. Niedermann, Ph.D. Thesis No. 2197, Univ. of Geneva (1986).
[23] D. Moffat, et al, ibid ref. 1, 245 (1992).
[24] D. Reschke, et al, ibid ref. 5, 2063 (1994).
[25] H. Padamsee, et al, *Proc. of the 4th Workshop on RF Superconductivity*, Y. Kojima ed., KEK, Tsukuba, Japan 207 (1989).
[26] J. Knobloch, priv. comm.
[27] K. Saito, et al, ibid ref. 2, 372 (1994).
[28] P. Kneisel, priv. comm.
[29] J. Graber, Ph.D. Dissertation, Cornell Univ. (1993).
[30] C. Crawford, et al, *Particle Accelerators*, **49**, 1 (1995).
[31] P. Schmueser, et al, Cornell Report **SRF-920925-10** (1992).
[32] S. Wolff, this conference, paper RPB09.
[33] H. Weise, this conference, paper RPB08.

Progress in the Study and Construction of the TESLA Test Facility Injector

R. Chehab, M. Bernard, J.C. Bourdon, T. Garvey, B. Jacquemard, M. Mencick, B. Mouton, M. Omeich, J. Rodier, P. Roudier, J.L. Saury, M. Taurigna-Quere and Y. Thiery.
Laboratoire de l'Accélérateur Linéaire, IN2P3 - CNRS, Orsay, France.

B. Aune, M. Desmons, J. Fusellier, F. Gougnaud, J.F. Gournay, M. Jablonka, J.M. Joly, M. Juillard, Y. Lussignol, A. Mosnier and B. Phung.
CEA, DSM/DAPNIA, Saclay, France.

S. Buhler and T. Junquera
Institut de Physique Nucléaire, IN2P3-CNRS, Orsay, France.

Abstract

A 500 MeV, 1.3 GHz superconducting linear accelerator is being studied and built to serve as a test facility for the TESLA linear collider project. The phase 1 injector, having an energy of 8 - 14 MeV and an intensity of 8 mA with a high duty cycle (800 microseconds, 10 Hz repetition rate), consists of a 250 keV electron gun, a 216.7 MHz sub-harmonic buncher and a superconducting capture cavity at the main linac frequency. The main characteristics (intensity, position, emittance, bunch length, energy spread) are to be measured using different techniques. A particular effort will be made on the use of optical transition radiation (OTR) for the determination of the transverse beam emittance as well as the bunch length. The injector, involving, the participation of three French laboratories (LAL, CEA/DAPNIA, IPN), will be tested partly in France (Orsay-Saclay) and then completely at DESY (Hamburg).

1. INJECTOR DESCRIPTION

The TTF linac injector can be conveniently divided into 5 sections; (i) a 250 kV electron source and its associated power supply, (ii) a 250 keV electron transport line, (iii) a superconducting RF "capture cavity" to bunch and accelerate the incoming beam to energies of 8 to 14 MeV, (iv) a beam analysis station to measure the properties of the accelerated beam, and (v) a high energy transport line to match the beam to the TTF linac.

As the TTF injector has already been described elsewhere [1,2,3] we will give only a brief description of each of these sections before describing in more detail the diagnostics which will be used on the injector. Table 1 shows the main specifications for the injector. A brief description of the TTF linac can be found in reference 4.

Table 1
Specification of the TTF Injector

Beam energy	> 8 MeV
Average current	8 mA
Pulse length	800 μs
Bunch length (rms)	1 mm
Energy spread (rms)	< 1%
RMS emittance	10 mm-mrad
Repetition rate	10 Hz

1.1 *The Electron Source and Power Supply*

The injector employs a 250 keV electron source in which the electrons are first accelerated to a nominal 30 keV in a conventional thermionic triode gun before receiving the additional energy by acceleration in a 90 cm long electrostatic column. Further details of the 30 kV gun can be found in a companion paper [5]. The electrostatic column is a commercial tube employing a series of metallic field-grading electrodes interspersed by glass insulators glued to the electrodes. The gun and the column are fed by individual power supplies, 40 kV for the former and 300 kV for the latter. To obtain a stable voltage during the 800 μs macropulse the column is powered via a 33 nF capacitor. Measurements of the long term voltage stability show the variations in the power supply are inferior to 1×10^{-4}. The entire power supply equipment, which was constructed by Sefelec, has been tested to full voltage. The column-gun arrangement is pumped via a 200 l/s pump at the outut of the column. The vacuum conductance of the column limits the pumping speed at the gun to 35 l/s. Following baking of the gun (80°C) and the column (60°C - limit recommended by manufacturer) the base pressure in the column is 4×10^{-9} mbar. Modulation of the gun is obtained by applying a train of -100 V, 1 ns pulses to the cathode from a wide-band amplifier. The input pulse to the amplifier can be varied in repetition rate from 217 MHz down to 1 MHz. The amplifier (Nucletudes, France) and its associated electronics has been tested into a dummy load and performs according to specification.

1.2 *The 250 keV Transport Line*

Along with the diagnostics (described below) the main elements of the 250 keV line consist of 4 shielded solenoidal focus lenses, and a 216.7 MHz sub-harmonic pre-bunching cavity. The lenses, required to transversely confine the beam during transport to the capture cavity, each provide an integrated strength of 8×10^{-5} T^2m over an active length of 9.4 cm and with a peak field of 350 Gauss. One of the four lenses is constructed as a 'double lens', i.e. two lenses with their magnetic fields in opposing directions. This means that there is no net rotation for the beam on passing through the lens and thus it can be conveniently used for beam emittance measurements. Each lens (purchased from Sigmaphi) incorporates a pair of horizontal and vertical steering elements in which the conductors are drawn onto printed circuit boards mounted inside the solenoids. The sub-harmonic bunching (SHB) cavity is a single re-entrant cell fabricated in stainless steel. To reduce the cavity RF losses the internal surface has

TESLA-Report 1995-11
Contributed Paper to the 1995 Particle Accelerator Conference and the International Conference on High Energy Accelerators.

received a thin (40 μm) deposition of copper. The cavity is powered by a 2 kW RF amplifier capable of delivering 5 ms pulses at 10 Hz. The amplifier (RFTS, Bordeaux), which was specified to have phase stability of 0.5° and an amplitude stability of 0.5% during a 1 ms pulse has been fully tested and shown to meet its specifications. The cavity has been conditioned with full RF power and bench measurements have confirmed the computed shunt impedance and unloaded Q of the cavity (R_s = 3 MΩ, Q_0 = 22000). With the exception of the SHB all elements on the 250 keV beam line have been mounted on a common girder and the girder has been installed at the output of the high voltage column. At the time of writing tests of the 250 keV beam are planned to commence at the beginning of May 1995.

1.3 *The Capture Cavity*

After the SHB further bunch compression is performed by a superconducting (SC) cavity. The SC cavity is a standard niobium, 9 cell, TESLA cavity, fabricated by CERCA S.A. (France). After hydroforming the half cells, heat treatment in a vacuum furnace was performed at Saclay (1300°C for 1000 minutes) which improves the residual resistivity ratio (RRR) of the niobium to an estimated value of 360. Following this treatment, complete electron welding of the cells, coupler ports and helium tank connecting flanges was accomplished. The chemical polishing treatment of the cavity internal surface (105 μm) was followed by High Pressure Water Rinsing (100 bar) at DESY.

The cavity was tested at DESY in a vertical cryostat equipped with a special coupler and waveguide transition for RF conditioning using High Peak Power (HPP) processing. Initial HPP in LHe at 4K was applied to the cavity with 1 MW peak power RF pulses at a repetition rate of 2 Hz and progressively increasing pulse lengths (50 μs, 100 μs, 200 μs). During this first experiment the accelerating field reached 21 MV/m with a $Q_{ext} = 10^6$. After cooling the helium bath to 1.8 K further HPP conditioning was applied culminating in a maximum accelerating field of 23 MV/m with a 300 μs RF pulse. Measurement of the Q vs E_{acc} at 1.8 K in cw mode shows a very good low field Q_0 (1.4×10^{10}) and absence of electron emission, however the accelerating field was limited to 14.5 MV/m by a quench. In conclusion the fabrication methods and the treatments were validated giving very good results for this cavity so allowing its mounting into the capture cryostat. Simulation studies of the injector show a large tolerance for the acceptable accelerating field (8 - 15 MV/m) in order to achieve the required electron beam specifications at the entrance to the first cryomodule.

The cold tuning system is now ready to be mounted in the cavity. It was assembled on a TESLA cavity and tested at room temperature giving a frequency tuning range of ± 470 kHz. A complete mechanical test, including the stepping motor, was performed in a LN_2 bath.

The main parts of the capture cryostat are now fabricated and the assembly has started. A special interface cold box is under construction in order to perform a complete test of the cavity with its coupler at the nominal operating conditions, both with cryogenic and RF power.

The capture cavity klystron has been succesfully tested to 300 kW peak power with RF pulses of 2 ms (10 Hz repetition rate). The modulator exhibits a plateau stability of 0.1% during the pulse. The phase and amplitude control loops are now constructed and the design concepts were succesfully tested in the MACSE facility at Saclay with the nominal pulsed condition of the TTF linac.

1.4 *The Beam Analysis Line*

In order to verify the beam parameters after acceleration in the capture cavity, and to allow regulation of the RF phases, a beam analysis line is installed down stream of the capture cavity. The high energy beam is deviated by a dipole magnet having a bend radius of 700 mm and a bend angle of 60°. Vertical edge focusing is provided by introducing a wedge angle of 18.24° at the exit and entrance faces. The resulting horizontal focal plane is 1242 mm downstream of the exit face, and consequently energy spread measurements will be made in this plane as described below. The maximum allowable field in the magnet is 0.1T, permitting electrons of energies upto 20 MeV to be measured.

1.5 *The High Energy Transport Line*

The principal elements of the high energy transport line, again with the exception of the diagnostics described below, consist of a pair of quadrupole triplets which will be used to transport the beam emerging from the capture cavity to the first cryomodule of the TTF linac. Again, the triplets incorporate steering elements to properly centre the beam at the input to the first cryomodule. At a later stage we plan to install a magnetic chicane on this line to permit experiments with off-axis beams in the linac. X-ray diodes, situated close to beam collimators, will indicate the presence of beam losses when tuning the injector. While tuning, the beam will be stopped in a cooled Faraday cup capable of handling the 1 kW average beam power.

2. BEAM DIAGNOSTICS

In order to measure and check the beam characteristics appropriate instrumentation is installed along the linac. On the 250 keV beam line, up to the first cryomodule, numerous monitors are provided due to the necessity to verify and, if possible, improve the initial beam characteristics. Non destructive monitors are used for beam intensity, position and RF phase but all profile monitors are destructive.

2.1 *Intensity and Position Measurements*

The beam pulse at the gun exit will be checked with a capacitive pick-up made from an alumina ring with a copper deposition on its inner and outer surfaces. The capacitance is 120 pF. Current monitors using toroids, placed before and after the capture cavity permit beam intensity monitoring and allow beam losses to be detected to provide a "trip" signal to turn off the gun.

Beam position monitors (BPM's) of the "button electrode" type have been constructed to monitor the beam position throughout the injector. An additional electrode on one BPM allows a measurement of the RF phase of the beam with respect to the master oscillator phase. The beam centroid is evaluated using the signals delivered by four electrodes. These signals are first filtered and then RF multiplexed before being treated in a single analogue electronic channel so as to avoid discrepancies due to different gains, bandwidths or zero offsets

between four different channels. Results concerning the beam position are represented on a graphic page using written indications (position in mm) or bargraphs. Acquisition and timing procedures are monitored through a VME card. Time shuttering inside the macropulse is forseen. This will allow a sharper analysis of the beam position.

2.2 *Beam Profile Measurements*

The 6-D emittance is obtainable through transverse and longitudinal profile measurements. Developments in optical methods and of the associated software tools make them preferable for this task [6]. Nevertheless, more classical methods using, for example, secondary electron emission are also considered.

Transverse Beam Profiles

Secondary electron emission with SEM-grids and optical transition radiation with aluminium foils and luminescent screens are used. Retractable aluminium oxide screens with a thin, transparent, deposition of indium oxide are used before and after the capture cavity to get approximate information on the beam dimensions. Quantitative information on the beam profile is obtained by an SEM-grid placed between the SHB and the capture cavity. The low beam energy (250 keV) implies short stopping ranges and high energy deposition in the grid material. Therefore titanium strips of only 12 μm thickness were chosen. To permit high enough resolution and measurement range, an SEM-grid with 32 strips of 300 μm width and 400 μm separation has been constructed. Integrators with LF356 op-amps are connected to the strips. An adjustable gain amplifier is added in each channel. Digitisation is ensured via a MAX255 circuit. Each of these modules has 8 sample-and-holds with a multiplexer, an 8 bit ADC and an 8 bit x 8 channel memory. Data treatment is done with standard VME. Beam profiles are displayed on a monitor and the corresponding widths (FWHM, RMS...) sent to a data base. Due to space-charge effects at this energy an appropriate procedure is necessary for the emittance calculation. It uses the integration of the Kapchinsky-Vladimirsky envelope equation,

$$R'' + K(z)R - 2I/I_A(\beta\gamma)^3R - \varepsilon^2/R^3 = 0$$

This equation is integrated succesively for n different settings of a magnetic focusing lens placed before the SEM-grid. The calculated radii are then compared to the measured ones and a least squares fit method gives the value of the emittance, radius and divergence of the beam upstream of the magnet. The Twiss coefficients are then derived and the ellipse constructed and displayed [7]. A 100 ns gating system allows emittance analysis inside the macropulse.

An SEM-grid made of 40 tungsten wires (20 micron diameter, 2 mm separation) placed in the horizontal focal plane of the bending magnet of the injector analysis line will provide energy spread measurements with a dispersion of 16 mm/%. Profiles and associated widths are processed as described above. After acceleration in the capture cavity, the transverse beam profile will be measured using OTR. N profiles, corresponding to N different settings of the quadrupole triplet upstream will permit the emittance to be calculated using the "method of three gradients" and a least square fitting routine. An intensified CCD camera permits time resolved emittance measurements in the macropulse with a minimum time window of 100 ns. The beam divergence at the OTR location will be obtained by collecting part of the optical image after a beam splitter. This will be done by placing the CCD camera in the focal plane of the lens. A digitising card (IPP/ELTEC) working on a VME standard will allow digital conversion, on 8 bits, of 4 cameras at video standard CCIR or EIA. An interlaced mode, however, is not allowed here. Image storage will be done in a 1 Megabyte memory zone. External synchronisation for the acquisition is used. Gain and offset at the entrance of the ADC is programmable. A video output is used to obtain the beam spot. A C-library is connected to this card. The use of numerical filters, mathematical transforms and histogram construction is available by this means. Moreover, this library supports the hardware functions. It works under OS9 and some modifications have made it usable under LynxOS and VXWorks.

Longitudinal Beam Profile

A second beam splitter will take part of the optical light to a streak camera (ARP-RGM-SC1) having a resolution of 3 ps. Bunch lengths will thus be determined.

3. SUMMARY

A brief description of the status of the TTF injector has been given. The electron source and the 250 keV beam line are essentially complete and beam tests will begin soon. A capture cavity with the desired RF performance has been produced and its cryostat is under fabrication. The klystron has been tested to full power. The magnets for the high energy beam line have been specified and are on order from industry.

4. REFERENCES

[1] J.C. Bourdon et al., "An Injector for the TESLA Test facility Linac", Proceedings of the 6th RF Superconductivity Conference (CEBAF, Virginia), pp 1188-1191, 1993.

[2] M. Bernard et. al., "The TESLA Test Facility Linac Injector", Proceedings of the 4th European Particle Accelerator Conference (London), pp 692-694, 1994.

[3] T. Garvey, "Electron Source Activities at LAL", Proceedings of the International Workshop on e^+e^- Sources and Pre-Accelerators for Linear Colliders, (Schwerin), 1994, pp 302-308.

[4] H. Weise, "The TESLA Test Facility - A Description of the Superconducting 500 MeV Linac", Proceedings of the 4th European Particle Accelerator Conference (London), pp 689-691, 1994.

[5] T. Garvey et. al., "Simulations and Measurements of the TTF Phase 1 Injector Gun", these Proceedings.

[6] R. Chehab et. al., "Beam Emittance Determination Using Optical Transition Radiation" Proceedings of the 3rd European Particle Accelerator Conference (Berlin), pp 1139-1141, 1992.

[7] B. Aune et. al., "A Device for Gun Emittance Measurement", IEEE Trans. Nucl. Sci., Vol NS-32, pp1896-1898, 1985.

STUDY OF LUMINOUS SPOTS OBSERVED ON METALLIC SURFACES SUBJECTED TO HIGH RF FIELDS

T. Junquera, S. Maïssa, M. Fouaidy, A. Le Goff, IPN (CNRS - IN2P3) 91406 ORSAY cedex, France
B. Bonin, M. Luong, H. Safa, J. Tan, CEA - DAPNIA - SEA, 91191 GIF-SUR-YVETTE cedex, France

ABSTRACT

The performance of high gradient superconducting RF cavities for electron accelerators is mainly limited by field emission. Major improvements have been recently obtained using different surface conditioning techniques confirming the involvement of metallic particles in field emission enhancement. In this paper we present the results obtained with an optical apparatus attached to an RF copper cavity equipped with a removable sample which is subjected to high RF fields (E_{pk} > 40 MV/m). Stable light spots are observed on the sample surface and their intensities and optical spectra are measured as a function of the surface electric field. The total emitted current is simultaneously measured by an isolated hollow electrode facing the sample. Particles of different types were deliberately sprinkled over the sample surface and the luminous features are studied. Light intensity, spectral power density and evolution of the luminous sites provide useful information for understanding the field emission phenomena and the conditioning effects.

INTRODUCTION

In this paper we report on the development and experimental work performed with an optical apparatus attached to an RF cavity. A detailed description of this device and some preliminary results were presented in previous papers [1] [2]. The initial goal was to develop a diagnostic tool able to localize and characterize the light spots which are observed on the surface of cavities submitted to high electric fields. This effect has been observed in DC experiments [3] and sometimes an intense luminous activity has been reported in RF cavities with heavy field emission.

EXPERIMENTAL SET UP

a) Cavity

A simple copper cavity has been proposed by the Saclay Group [4] [5] for studying the RF field emission on removable samples. Field emission from metallic surfaces at room temperature is practically the same as from those at liquid helium temperatures. A simple cavity with a removable sample, operating at room temperature offers fast turn around and low operating costs. The work concerning deliberately contamination with metallic particles was presented in references [4] [5] [6]. An identical cavity was slightly modified to simultanously observe the top of the sample through an optical window and collect the electron current with a hollow electrode was developed [1] [2]. Two types of samples were used in the present study [Fig.1]: #1 giving E_{max} = 60 MV/m and #2 giving E_{max} = 100 MV/m (for 5 kW peak input power). These are the electric fields on the top of the samples which can be maintained for pulse lengths in the range of 10 µs to 5 ms with a duty cycle of 1 %.The field obtained with #1 samples was calibrated using a X-ray detector and the field with #2 samples was calculated with means of a computational code.

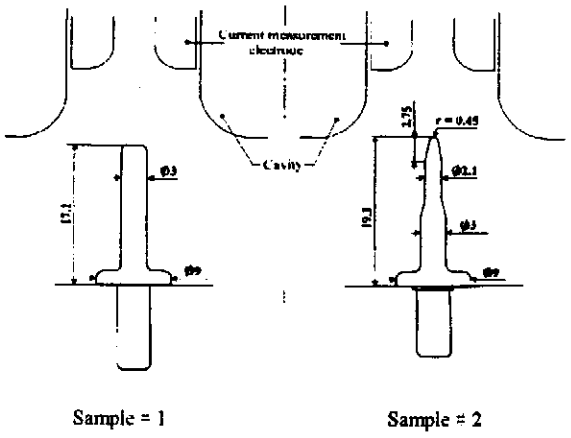

Fig. 1 : Sample geometry (all dimensions in mm)

b) Optical detectors

A simplified scheme is given in Figure 2. The intensified camera has a sensitivity of 5 x 10^{-4} lux in the wavelength range of 400 - 650 nm (at 40 % of maximum relative response). A detailed description is given in Ref. [2]. During the first tests a series of high-pass filters was used for a rough evaluation of the spectral power density with a resolution of 50 nm. The spectral analysis system was recently improved. A pair of crossed slits (50 µm) was inserted in the optical path. While the slits are moved to select the light emanating from just one spot. A prism is then positioned on the optical path and the dispersed light analysed by a cooled CCD multichannel sensor (Hamamatsu C5809 model).

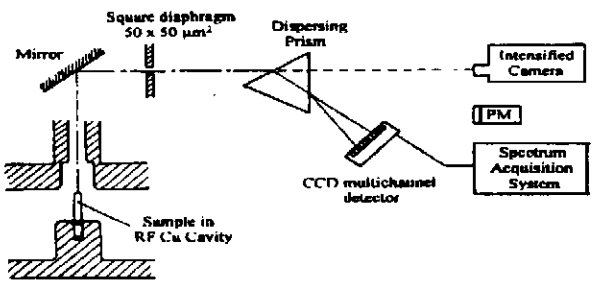

Fig 2 : Optical detectors

This two dimensional CCD array (64 vertical x 512 horizontal) integrates the incoming light during the exposure phase. At the end of this time, the photocharges of individual pixels are accumulated, first along the vertical axis (binning

TESLA-Report 1995-11
Presented at the 1995 Particle Accelerator Conference
Dallas (USA), May 1 - 5, 1995

phase) and then sequentially transferred to a readout stage. A sample and hold circuit delivers a low impedance video signal which is digitized by an oscilloscope. This signal is processed by a PC computer program which displays the power density spectrum for each exposure phase.

Due to the wavelength dependence of the refractive index of the prism, the wavelength range covered by each CCD channel varies from channel to channel : 1nm/channel at 400 nm, 10 nm/channel at 1100 nm (1 channel corresponds to 64 vertical pixels). The CCD sensitivity and channel calibration were performed with different near-monochromatic light sources (laser diode, LED, narrow band filters) [Fig. 3].

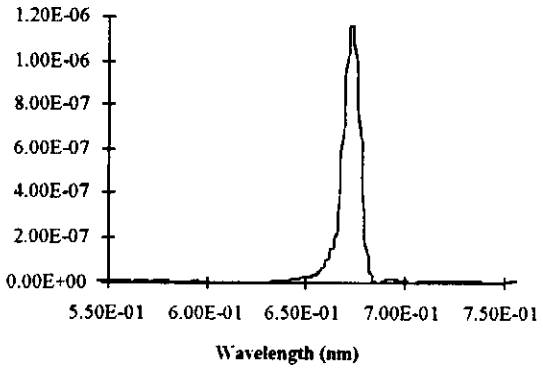

Fig. 3 : Calibration spectrum obtained with a 670 nm laser diode

Our calibration of power sensitivity was within ~ 7 % of the manufacturer's values : a spot with luminous intensity of 10^{-14} W is detectable by this means. The correspondance between wavelength and channel numbers was accomplished with ± 1 channel error by using an interpolation method between the monochromatic wavelength values.

RESULTS

Samples were prepared using a technique which is now established [4]. Particles are sprinkled on the top of a clean sample placed over the cold vapors of an LN_2 bath. The particles stick to the moistened surface and after drying remain well adhered (for samples prepared in this manner, the particles remain attached during sample mounting in the cavity and the majority remain attached even with the application of electrostatic fields). The samples are mounted in the cavity on a laminar flow bench. The prepared cavity is then evacuated and the experiment starts when the pressure reaches the range of 10^{-7} mbar. The past efforts of the GECS group were concentrated on field emission from metallic particles and surface scratches [4, 5, 6]. In this paper we focus on observations made on samples contaminated with dielectric (Al_2O_3) particles. Two sizes of alumina particles have been studied : large particles (50 - μm) and small particles (~ 1μm). On examination of the samples in the SEM, it was found that the smaller particles tended to agglomerate into larger clusters, but there were many individual particles as well.

Large particles

A copper sample (type # 1) contaminated with alumina particles was submitted to RF pulses of 4 ms (1 Hz repetition rate). Luminescent spots were clearly observed starting at a field of 5 MV/m. Increasing the field up to 30 MV/m leads to a higher density of spots on the top of the sample and a higher luminous power [Fig. 4]. The electron current was very unstable (500 μA at 10 MV/m).

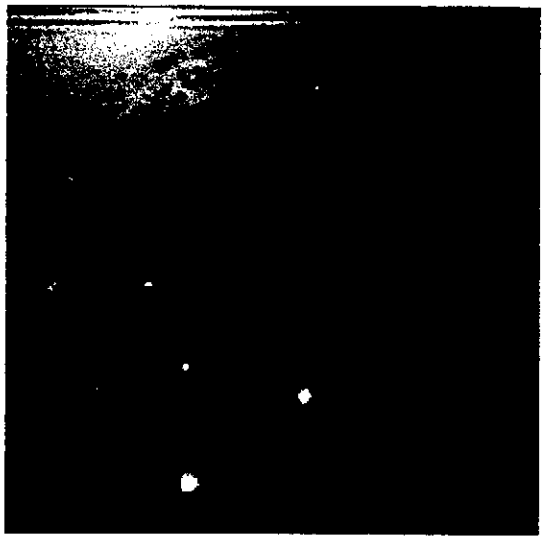

Fig. 4 : large alumina particles at E = 8 MV/m

Above this field level luminous tracks were observed, sometimes following straight trajectories, other times curved[Fig. 5].

Fig. 5 : large alumina particles at E = 20 MV/m

These tracks appear to be originated from the light spots and are accompanied with an increase of the vacuum pressure, higher electron current and important disturbances in the frequency tuning of the cavity. After several RF pulses the electron current and luminous effects stabilize, but each time the RF power level is increased it triggers a new spectacular pattern of light tracks and sometimes "explosion-like" luminous effects. Eventually a field level of 40 MV/m was reached and a more stable emission phase was obtained. At this point the RF power was turned off and the cavity

vacuum allowed to recover. The cavity behaved very differently during the next experiment. The current was quite stable and found to be roughly Fowler-Nordheim in nature. Luminous activity did not start until 20 MV/m. Several individual spots were measured with the spectral analysis system. Each spot showed a spectrum [Fig. 6] with same shape but with a different spectral density peak value and wavelength (ranging from 600 nm to 800 nm). One spot was studied between 30 - 40 MV/m; it was found that the peak wavelength did not change as the field level was increased. This study took several hours and during this time some of the light spots remained quite stable

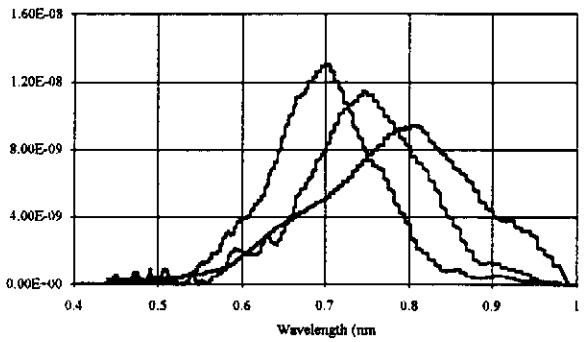

Fig. 6 : Three different light spots

Afterwards, the sample was examinated in a SEM. Melted features were found on alumina particles with diameters on the order of 10 µm. Small clusters of smaller particles (~ 5µm in diameter) coated the sample surface and some craters were also identified in their vicinity.

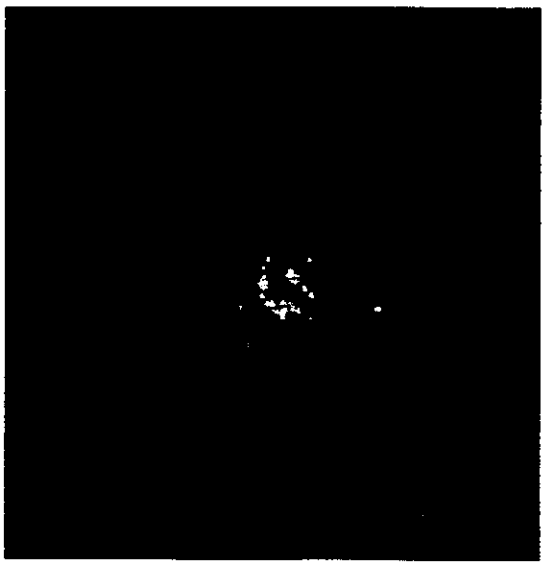

Fig. 7 : Small alumina particles at E = 80 MV/m

Small particles

In this experiment a niobium sample of type #2 was used which gave more stable operating conditions. The electron current was quite low (15 µA at 80 MV/m) and unstable during the first few minutes. Small luminous spots [Fig. 7] were observed which remain visible just for 1 or 2 RF pulses (100 µs long, 5 Hz repetition rate, estimated field 80 MV/m). After this conditioning period the pulse length was increased to 2 ms (1.2 Hz repetition rate). This time, no light spots were visible on the top of the sample and the electron current stayed stable ($I_e \cong 2$ µA at 80 MV/m). Examination in the SEM showed a large number of small craters (1 or 2 µm) in the area where the light spots had been visible. No trace of initial particles was founded over the surface. The short life and instability of the light spots made the spectral measurement very difficult in this experiment.

DISCUSSION

These experiments show that dielectric particles interact strongly with the RF fields in the cavity. They emit light and may be responsible for the observed electron current. There is also a clear dependence on the particle size.

The unstable behavior during the conditioning phase is accentuated for the larger particles which produce higher currents and more intense light spots. The light spectra show some similarity to those observed in alumina waveguide windows [7]. Some luminous features observed in the experiment with large particles have been also observed in DC experiments [3] : same order of magnitude of the luminous power in a light spot (10^{-12}W), spectral power density in the range 600 nm - 800 nm and peak wavelength not dependent on the electric field.

Let us consider the RF heating of these particles. The power density absorbed by a dielectric is given by $P(W/m^3) = 1/2\ \varepsilon_0\ \varepsilon_r\ \omega E^2\ \tan\delta/2$ .For alumina ($\varepsilon_r = 10$, $\tan\delta = 10^{-3}$) in a field of 50 MV/M at 1.5 GHz, we find $P \sim 10^{12}W/m^3$. The temperature increase of a particle of any size can be calculated using the specific heat (Cp ≅ 756 J/kg.K) and density 3970 kG/m3) of alumina. The time constant τ, to reach this temperature is proportional to the contact thermal resistance, R_{th} and to the total heat capacity C of the particle. From SEM measurements, a value of $R_{th} \geq 10^7$ K/W has been determined giving time constants in the range 10 µsec - 100 msec.

REFERENCES

[1] T. Junquera, A. Le Goff, B. Bonin, H. Safa, J. Tan : "6th Workshop on RF Superconductivity" (Newport News, Oct. 1993) CEBAF report, p. 1014,

[2] T. Junquera, S. Maïssa, M. Fouaidy, A. Le Goff, B. Bonin, H. Safa, J. Tan : Proc. EPAC 94 (London 1994), p. 2203.

[3] R. Hurley, P. Dooley, J. Phys. D : Appl. Phys. 10 (1977) L 195,

[4] J. Tan, H. Safa, B. Bonin, J.M. Tessier : J. Phys. D : Appl. Phys. 27 (1994) 2644,

[5] J. Tan, H. Safa, B. Bonin, M. Jimenez : J. Phys. D : Appl. Phys. 27 (1994) 2654,

[6] J. Tan, H. Safa, B. Bonin, J. Jodet : Proc. EPAC 94 (London 1994).[7] S. Michizono, Y. Saito, S. Yamagucni, S. Anami, N. Matuda, A. Kinbara, Proc. XVth ISDEIV, Darmstadt (1992), p. 614.

[7] S. Michizono, Y. Saito, S. Yamaguchi, S. Anami, N. Matuda, A. Kinbara, Proc. XVth ISDEIV, Darmstadt (1992), p. 614.